Semiconductor Colloidal Quantum Dots For Photovoltaic Applications

Cheng Cheng

Mansfield College

A thesis submitted in fulfilment of requirement for the degree of

DPhil in Materials at **The University of Oxford**

Abstract

This thesis studies lead suphide (PbS) colloidal quantum dots and their photovoltaic applications.

Different sizes of PbS QDs were synthesised and characterised using absorption spectroscopy and transmission electron microscopes. PbS QD Schottky junction devices were fabricated with AM1.5 power conversion efficiency up to 1.8 %. The Schottky junction geometry limits the device performance. A semiconductor heterojunction using ZnO as an electron acceptor was built and the device efficiency increased to 3%. By studying the light absorption and charge extraction profile of the bilayer device, the absorber layer has a charge extraction dead zone which is beyond the reach of the built-in electric field. Therefore, strategies to create a QD bulk heterojunction were considered to address this issue by distributing the junction interface throughout the absorber layer. However, the charge separation mechanism of the QD heterojunction is not clearly understood: whether it operates as an excitonic or a depleted p-n junction, as the junction operating mechanism determines the scale of phase separation in the bulk morphology. This study shows a transitional behaviour of the PbS/ZnO heterojunction from excitonic to depletion by increasing the doping density of ZnO.

To utilise the excitonic mechanism, a PbS/ZnO nanocrystal bulk heterojunction was created by blending the two nanocrystals in solution such that a large interface between the two materials could facilitate fast exciton dissociation. However, the devices show poor performance due to a coarse morphology and formation of germinate pairs. To create a bulk heterojunction where a built-in electric field could assist the charge separation, a TiO_2 porous structure with the pore size matching with the depletion width was fabricated and successfully in-filled by PbS QDs. The porous device produces 5.7% power conversion efficiency, among one of the highest in literature. The enhancement comes from increased light absorption and suppression of charge recombination.

Acknowledgements

I would like to thank Dr Andrew Watt for his supervision and constant encouragement in my journey to the title of Doctor of Philosophy. He guided me in the right direction when I was lost and provided me timely support when I had difficulty. He taught me how to think out of the box and we have generated some great research ideas. He also helped me with my English, which I do think it has improved significantly over the years.

I would like to thank Dr Hazel Assender for her supervision and guidance. I am grateful for her support and feedback on my progress. I learned a lot of her systematic approach and accuracy on research. I thank her for helping with my presentation skills and writing skills, in which I believe I am more confident now.

I thank my colleague Peter Kovacik for the constant discussion and exchange of ideas in labs, pubs or restaurants as well as during our excursions to mountains and beaches. I thank Jenna Holder for her help in advanced optoelectronic characterisation and our collaboration in the bulk heterojunction project. I thank Shawn Willis for teaching me solar cell characterisation and our collaborative project on PbS/ZnO heterojunction. I thank Mike Lee and Nakita Noel from the Physics Department for their help of making the TiO_2 substrates and many after-

hour experiments in the Clarendon Laboratory. I thank Dr Henry Snaith for his help on the collaboration of the PbS/TiO_2 project. I thank Alexandros Stavrinadis for his introducing me to the lab as well as letting me stay in his place in Shanghai and Barcelona. I thank Elva Zou for brushing up my Chinese and our work on AZO/PbS. I thank Simon Fairclough for teaching me quantum dot synthesis and his help on TEM characterisation. I thank Chris Cattley for constant lab improvement and tidying up and Laura Droessler for various lab socials.

I thank Richard Turner and John Topping for their technical support. I thank Dr Gareth Hughes for helping me with FIB-SEM and Dr Jamie Warner for PL. I thank Ziqian Ding, Long Jiang, Sam Johnson and Matthew Wincott for numerous discussions. I thank the Darren Neo, Assia Kasdi, Natasha Hjerrild and Inji Yeom for being fast and enthusiastic learners to expand my research.

I would also like the following part II and visiting students: Lou Yeoh, Simon Bowcock, Miriam Höner, Brienne Kugler, Tom Walton, Anna Rodriguez-Chavez, Kayla Nguyen, Jamie Lee, Maria Nelson, Dan Camp, Jessica Lin, Chuchu Zhang for making this lab a fun place.

In the end, I would like to thank my parents for their love and support and my girlfriend Sook Teng Vun for being by my side.

Statement of Originality

This thesis is an account of work carried out by the author in the Department of Materials, the University of Oxford under the supervision of Dr Andrew Watt and Dr Hazel Assender. Where the work of others has been drawn upon this is duly acknowledged in the text, and a list of references is presented at the end of each chapter. No part of this thesis has been submitted towards the completion of another degree at the University of Oxford or elsewhere. Parts of the thesis have been submitted to or published in the following scientific journals or conference presentations:

Journal articles:

Cheng C., Lee M.M., Noel N.K., Hughes, G.M., Ball, J.M., Assender H.E., Snaith H.J., Watt A.A.R., Templated TiO_2/PbS bulk heterojunction solar cells, in preparation.

Cheng C., Holder J.K.L, Warner J., Assender H.E., Watt A.A.R., Nanocrystal bulk heterojunction solar cells based on PbS-ZnO, in preparation.

Willis S.M., Cheng C., Assender H.E., Watt A.A.R., *The transitional heterojunction behaviour of PbS/ZnO solar cells*, *Nano Letters*, 2012, **12**, 1522-1526.

Conference proceedings:

Cheng C., Willis S.M., Cattley C.A., Walton T., Assender H.E., Watt A.A.R., PbS nanocrystals for photovoltaic applications, *Proceedings of Photovoltaic Science Application and Technology*, Edinburgh, UK, 2011

Conference presentations:

Cheng C., Willis S.M., Assender H.E., Watt A.A.R., Heterojunction PbS/ZnO colloidal quantum dot solar cells. In *Photovoltaic Science Application And Technology*, Edinburgh, UK, 2011.

Cheng C., Willis S.M., Assender H.E., Watt A.A.R., PbS quantum dot heterojunction solar cells. In Japan-UK Dye-sensitised Organic Photovoltaic, Oxford, UK, 2011.

Cheng C., Willis S.M., Assender H.E., Watt A.A.R., Heterojunction PbS/ZnO colloidal nanocrystal solar cells. In *IOP Advanced In Photovoltaics*, London, UK, 2011.

Cheng C., Willis S.M., Assender H.E., Watt A.A.R., All inorganic bulk heterojunction PbS/ZnO nanocrystal solar cells. In *RSC Functional Bulk Nanostructure for Energy Storage and Generation*, Chicheley, UK, 2011.

Cheng C., Willis S.M., Assender H.E., Watt A.A.R., Charge generation of dissociation mechanisms in PbS-ZnO heterojunction colloidal quantum dot photovoltaics. In *2011 MRS Fall Meeting*, Boston, USA, 2011.

Cheng C., Lee M.M., Noel N.K., Assender H.E., Snaith H.J., Watt A.A.R., Templated TiO_2/PbS bulk heterojunction colloidal quantum dot solar cells. In *2013 MRS Spring Meeting*, San Francisco, USA, 2013.

Table of Contents

List of Abbreviations

AFM	Atomic force microscope
Ag	Silver
Al	Aluminium
AM	Air Mass
Au	Gold
BDT	1,4-Benzenedithiol
BHJ	Bulk heterojunction
Bi_2S_3	Bismuth sulphide
C60	Buckminsterfullerene
C - V	Capacitance - voltage
CB	Conduction band
CELIV	Carrier extraction via linear increasing voltage
CT	Charge transfer
CTAB	Cetyltrimethylammonium bromide
CuPc	Copper phthalocyanine
EDT	1,2-Ethaneidthiol
E_g	Band gap
EQE	External quantum efficiency
FET	Field effect transistor
FF	Fill factor
FIB	Focussed-ion beam
FTO	Fluorine-doped tin oxide
HOMO	Highest occupied molecular orbital
I - V	Current - voltage
ITO	Indium-doped tin oxide
J_{sc}	Short circuit current density
LED	Light-emitting diode
LUMO	Lowest unoccupied molecular orbital
MCC	Metal chalcogenide complex
MEG	Multiple exciton generation
MEH-PPV	Poly[2-methoxy-5-(2-ethylhexyloxy)-1,4-phenylenevinylene]

MoO_x	Molybdenum oxide
MPA	3-Mercaptopropinoic acid
NREL	National Renewable Energy Laboratory
OA	Oleic acid
ODE	1-Octadecene
P3HT	Poly(3-hexylthiophene-2,5-diyl)
PbS	Lead sulphide
PbSe	Lead selenide
PCBM	Phenyl-C61-butyric acid methyl ester
PCE	Power conversion efficiency
PEDOT:PSS	poly(3,4-ethylenedioxythiophene) poly(styrenesulfonate)
PL	Photoluminescence
PS	Polystyrene
PTFE	Polytetrafluoroethylene
QD	Quantum dot
QE	Quantum efficiency
RMS	Root mean square
Sc	Scandium
SEM	Scanning electron microscope
SILAR	Successive ionic layer absorption and reaction
TCO	Transparent conductive oxide
TDPA	Tetradecylphosphonic acid
TEM	Transmission electron microscope
TiO_2	Titanium dioxide
$(TMS)_2S$	Bis(trimethylsilyl) sulphide
TOPO	Trioctylphosphine oxide
VB	Valence band
V_{bi}	Built-in potential
V_{oc}	Open circuit voltage
ZnO	Zinc oxide

Chapter 1 - Introduction

1.1 Solar energy and low cost photovoltaics

The single largest cause for global warming is carbon dioxide primarily emitted in the production of energy from burning of fossil fuel[1]. Oil, coal and natural gas, the three major fossil fuels, generate 86.5% of primary energy on earth[1]. Therefore, to develop alternative carbon-free renewable energy will be one of the best choices for the world to solve climate change to benefit the entire society.

Solar energy is abundant. The energy of all known existing fossil fuel is as much as the energy the earth receives in only 50 days from the sun[1]. One direct way to convert this sustainable energy to electricity is through photovoltaic cells[2]. The main hurdle to the large deployment of photovoltaic panels to generate electricity is the cost of materials and manufacturing based on the current technology. A study published by the United Kingdom government[3] shows the cost of electricity generated by photovoltaic modules in the UK is £314/MWh, by on-shore wind is £90/MWh and by natural gas is £50/MWh. The photovoltaic materials currently available in the market are dominated by crystalline silicon, along with thin film materials: cadmium telluride (CdTe), copper indium gallium selenide (CIGS) and amorphous silicon. Processing of these bulk materials is

expensive and required high-energy input, making the energy payback time 3-4 years for crystalline solar cells[4].

Reducing the costs of harnessing solar energy is being solicited in low temperature solution-processed semiconductors such as conjugated polymers[5–7], conjugated small molecules[8–10] and colloidal quantum dots[11–13]. This allows the PV modules to be manufactured through liquid phase deposition such as spin coating or inkjet printing, which can be combined with roll-to-roll production on flexible substrates, lowering both manufacturing and installation costs. Colloidal quantum dots have gained much attention recently for their band gap tunability. PbS[14–16], PbSe[17–19], CdSe[20–22], CdS, Cu_2S, SnS[23], SnSe[24], InAs[25] and InP[26] materials have been studied for their photovoltaic properties. Lead chalcogenide quantum dots have received most attention with their efficiency increasing fast from 0.1% to near 8% within 5 years.

1.2 Goal of the thesis

The focus of this thesis is to increase the power conversion efficiency of PbS QDs photovoltaic device by improving the device structure through our understanding of the fundamental process of the colloidal QDs. To rationalise the design of the device architecture, two main points are addressed in this thesis:

1) Whether the operating mechanism of a QD heterojunction is excitonic or depleted p-n. In an excitonic junction, charge collection length is determined by the exciton diffusion length and a chemical potential between donor and acceptor

must form to facilitate the dissociation of exciton. In a depleted p-n junction, a built-in electric field is present and can efficiently drift the electrons and holes to the corresponding electrodes. Thus for optimal design of the cell architecture, the mechanism of charge separation should be determined.

2) Since the absorber thickness, which determines the light absorbed by a device, is limited by the drift-diffusion length of charge carriers, new device structures were studied to show whether they can optimise both light absorption and charge extraction.

1.3 Structure of the thesis

Chapter 2 reviews the literature of the fundamentals of QD photovoltaics and their recent progress. The initial experimental research on PbS QD photovoltaic devices was carried out in 2010. Chapter 3 describes the experimental techniques of materials synthesis, QD device fabrication and characterisation as well as some results on QD Schottky junction devices. Chapter 4 reports an ITO/PEDOT:PSS/PbS/ZnO/Al device structure with the focus on understanding the junction operating mechanism. Chapter 5 and Chapter 6 explore interpenetrated QD donor-acceptor structures: a PbS/ZnO colloidal bulk heterojunction and a porous TiO_2/PbS bulk heterojunction. Chapter 7 concludes the scientific findings of the thesis and propose further work to be carried out.

1.4 References

1. Gore, A. *Our Choice: A Plan to Solve the Climate Crisis*; Push Pop Press: Menlo Park, CA, 2009.

2. Barnham, K. W. J.; Mazzer, M.; Clive, B. Resolving the Energy Crisis©: Nuclear or Photovoltaics? *Nature Materials* **2006**, *5*, 161–164.

3. Department of Energy and Climate Change *Review of the Generation Costs and Deployment Potential of Renewable Electricity Technologies in the UK*; 2011.

4. Knapp, K.; Jester, T. Empirical Investigation of the Energy Payback Time for Photovoltaic Modules. *Solar Energy* **2001**, *71*, 165–172.

5. Brabec, C. J.; Serdar Sariciftci, N.; Hummelen, J. C. Plastic Solar Cells. *Advanced Functional Materials* **2001**, *11*, 15–26.

6. Mayer, A. C.; Scully, S. R.; Hardin, B. E.; Rowell, M. W.; Mcgehee, M. D. Polymer-Based Solar Cells. *Materials Today* **2007**, *10*, 28–33.

7. Hoppe, H.; Serdar Sariciftci, N. Organic Solar Cells: An Overview. *Journal of Materials Research* **2004**, *19*, 1924–1945.

8. Wöhrle, D.; Meissner, D. Organic Solar Cells. *Advanced Materials* **1991**, *3*, 129–138.

9. Sun, Y.; Welch, G. C.; Leong, W. L.; Takacs, C. J.; Bazan, G. C.; Heeger, A. J. Solution-Processed Small-Molecule Solar Cells with 6.7% Efficiency. *Nature Materials* **2012**, *11*, 44–48.

10. Mishra, A.; Bäuerle, P. Small Molecule Organic Semiconductors on the Move: Promises for Future Solar Energy Technology. *Angewandte Chemie International Edition* **2012**, *51*, 2020–2067.

11. Kamat, P. V. Quantum Dot Solar Cells. Semiconductor Nanocrystals as Light Harvesters. *Journal of Physical Chemistry C* **2008**, *112*, 18737–18753.

12. Sargent, E. H. Colloidal Quantum Dot Solar Cells. *Nature Photonics* **2012**, *6*, 133–135.

13. Nozik, A. J. Quantum Dot Solar Cells. *Physica E* **2002**, *14*, 115–120.

14. McDonald, S. A.; Konstantatos, G.; Zhang, S.; Cyr, P. W.; Klem, E. J. D.; Levina, L.; Sargent, E. H. Solution-Processed PbS Quantum Dot Infrared Photodetectors and Photovoltaics. *Nature Materials* **2005**, *4*, 138–142.

15. Kramer, I. J.; Sargent, E. H. Colloidal Quantum Dot Photovoltaics: a Path Forward. *ACS Nano* **2011**, *5*, 8506–8514.

16. Sargent, E. H. Infrared Photovoltaics Made by Solution Processing. *Nature Photonics* **2009**, *3*, 325–331.

17. Choi, J. J.; Lim, Y.-F.; Santiago-Berrios, M. B.; Oh, M.; Hyun, B.-R.; Sun, L.; Bartnik, A. C.; Goedhart, A.; Malliaras, G. G.; Abruña, H. D.; *et al.* PbSe Nanocrystal Excitonic Solar Cells. *Nano Letters* **2009**, *9*, 3749–3755.

18. Ma, W.; Swisher, S. L.; Ewers, T.; Engel, J.; Ferry, V. E.; Atwater, H. a; Alivisatos, a P. Photovoltaic Performance of Ultrasmall PbSe Quantum Dots. *ACS Nano* **2011**, *5*, 8140–8147.

19. Luther, J. M.; Law, M.; Song, Q.; Perkins, C. L.; Beard, M. C.; Nozik, A. J. Structural, Optical, and Electrical Properties of Self-Assembled Films of PbSe Nanocrystals Treated with 1,2-Ethanedithiol. *ACS Nano* **2008**, *2*, 271–280.

20. Robel, I.; Subramanian, V.; Kuno, M.; Kamat, P. V Quantum Dot Solar Cells. Harvesting Light Energy with CdSe Nanocrystals Molecularly Linked to Mesoscopic TiO2 Films. *Journal of the American Chemical Society* **2006**, *128*, 2385–2393.

21. Fan, S.-Q.; Kim, D.; Kim, J.-J.; Jung, D. W.; Kang, S. O.; Ko, J. Highly Efficient CdSe Quantum-Dot-Sensitized TiO2 Photoelectrodes for Solar Cell Applications. *Electrochemistry Communications* **2009**, *11*, 1337–1339.

22. Huynh, W. U.; Dittmer, J. J.; Alivisatos, a P. Hybrid Nanorod-Polymer Solar Cells. *Science* **2002**, *295*, 2425–2427.

23. Stavrinadis, A.; Smith, J. M.; Cattley, C. A.; Cook, A. G.; Grant, P. S.; Watt, A. A. R. SnS/PbS Nanocrystal Heterojunction Photovoltaics. *Nanotechnology* **2010**, *21*, 185202–185207.

24. Franzman, M. a; Schlenker, C. W.; Thompson, M. E.; Brutchey, R. L. Solution-Phase Synthesis of SnSe Nanocrystals for Use in Solar Cells. *Journal of the American Chemical Society* **2010**, *132*, 4060–4061.

25. Yu, P.; Zhu, K.; Norman, A. G.; Ferrere, S.; Frank, A. J.; Nozik, A. J. Nanocrystalline TiO2 Solar Cells Sensitized with InAs Quantum Dots. *Journal of Physical Chemistry B* **2006**, *110*, 25451–25454.

26. Liao, H.; Tsao, C.; Lin, T.; Jao, M.; Chuang, C. Nanoparticle-Tuned Self-Organization of a Bulk Heterojunction Hybrid Solar Cell with Enhanced Performance. *ACS Nano* **2012**, *6*, 1657–1666.

Chapter 2 - Literature Review

2.1 Fundamental physics of solar cells

2.1.1 The solar spectrum

The extra-terrestrial solar spectrum is very similar to the spectrum of the black body at 5760 K (*Figure 2.1*). Before reaching the earth, the solar radiation is either absorbed or scattered by the atmosphere, changing its intensity at different wavelengths[1]. The term "Air Mass (AM)" which is the ratio of optical path length after attenuation by the atmosphere to the optical path length if the sun is directly overhead is used to quantify the attenuation by the atmosphere[2]. The standard spectrum for solar cell characterisation is Air Mass 1.5.

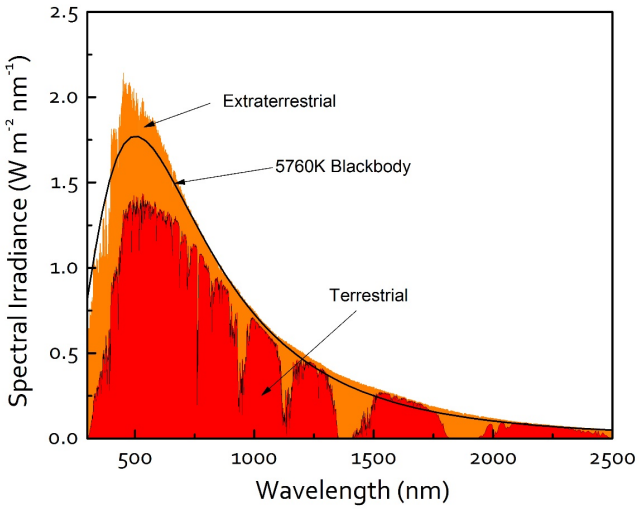

Figure 2.1: Extraterrestrial solar spectrum, the spectrum of a 5760K blackbody and terrestrial spectrum. (Spectra data are referenced from ASTM G-173-03)

2.1.2 Operational principle of solar cells

When a semiconductor is exposed to light of sufficient energy, photons can excite electrons from low-energy states (valence band) to high-energy states (conduction band). The energy difference between the valence band (VB) and the conduction band (CB) determines the semiconductor's band gap. Only photons with energy greater than the band gap can excite electrons to the CB. On losing an electron in the VB, a positively charged hole is generated. The excited electron could recombine with the hole quickly due to their Coulombic interaction. In a photovoltaic device, a junction is necessary to extract the electrons to the external circuit before they recombine. *Figure 2.2* describes the processes within a solar cell formed from a Schottky junction.

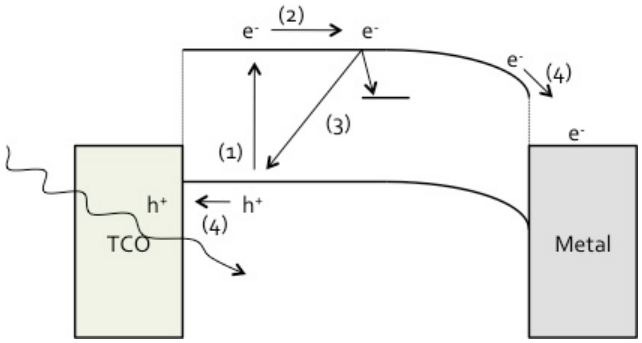

*Figure 2.2: Basic mechanism of a Schottky junction solar cell. (1) Charge generation; (2) diffusion; (3) recombination; (4) charge separation. * TCO - Transparent conductive oxide.*

2.1.2.1 Charge generation by photon absorption

The photon interaction with a solid material is described as absorption[3]. The absorption of light can be described by the well-known Beer-Lambert Law,

$$I(\lambda, x) = I_0(\lambda)e^{-\alpha(\lambda)x} \tag{2.1}$$

where $I(\lambda, x)$ is the intensity of monochromatic light λ at a point x in a layer, $I_0(\lambda)$ is the incident light intensity, and $\alpha(\lambda)$ is absorption coefficient. In a conventional solar cell, the major contribution to $\alpha(\lambda)$ are band-to-band transitions, where photons with energy greater than the band gap (E_g) can excite an electron to a high energy state, creating a free electron-hole pair.

In organic or quantum dot materials the dielectric constants are low[4] so the electron and hole wavefunctions are localised[5]. Excitons are bound states of electron-hole arising from the Coulombic force between them. The Coulombic interaction gives a high binding energy between the electron and hole in an exciton. Excitons are not charged, so their movement is by diffusion. As the binding energy is high, the diffusion length of excitons is very limited.

Besides electron transitions from band-to-band, intraband transitions, phonon absorption, band-to-trapped state and trapped state-to-trapped state transitions[3] are the optical processes that can occur in an absorption layer. If reflection and interference can be neglected, the absorption depth or optical penetration length of an absorption layer will be $1/\alpha(\lambda)$. *Figure 2.3* shows the optical penetration depth of PbSe nanocrystals at different wavelengths. High energy photons (short wavelength) have shorter absorption lengths, while low energy photons are absorbed less strongly and can penetrate a longer distance[6,7].

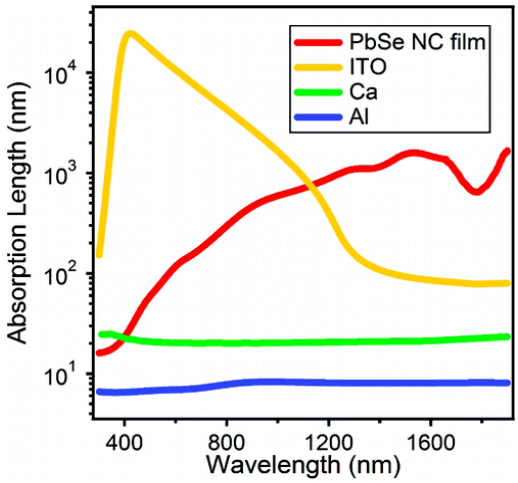

Figure 2.3: Absorption penetration depth of PbSe nanocrystals, indium-doped tin oxide, calcium and aluminium at different wavelengths. (Adopted from Law et al.[6])

2.2.2.2 Charge dissociation

A key component in photovoltaic devices is a junction that provides a driving force to separate electron-hole pairs or bound excitons[2].

In the case of an excitonic solar cell, excitons must migrate to an interface (i.e. type-II donor/acceptor interface) in order to dissociate into free electrons and holes (*Figure 2.4*). The chemical potential difference between the donor and acceptor materials provides the driving force for exciton separation.

In conventional solar cells, a built-in electric field is established near the junction interface between two materials with asymmetrical electronic properties. The junction can be formed between metal and semiconductor or between p-type and n-type semiconductors.

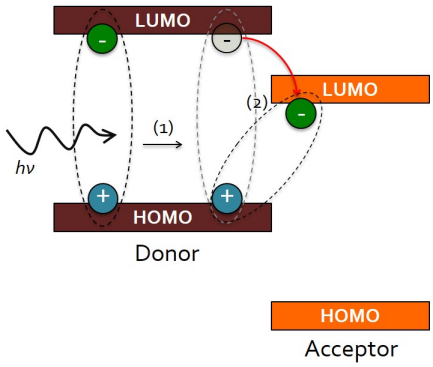

Figure 2.4: A schematic showing the type-II heterojunction donor-acceptor interface (readapted from reference[8]). (1) a photogenerated exciton migrate to the interface; (2) the exciton split into a free electron-hole pair with electron transferring to acceptor LUMO leaving a hole in the donor phase.

2.1.2.3 Semiconductor-metal Schottky junction

When a semiconductor and a metal are brought into contact, their Fermi levels align to achieve equilibrium by exchange of carriers between the two materials. A potential difference is built up by a change in carrier concentration, and at equilibrium, this potential difference is large enough to prevent further carrier flow. At the interface, the semiconductor carries a net charge forming a space charge region, which is negligible in the metal as the dielectric constants of semiconductors are much higher than those of metals. Accordingly, the change in potential, or band banding, occurs in the space charge region (or depletion region), creating a barrier to carrier flow. *Figure 2.5* shows the schematic of a Schottky junction between a metal and a p-type semiconductor.

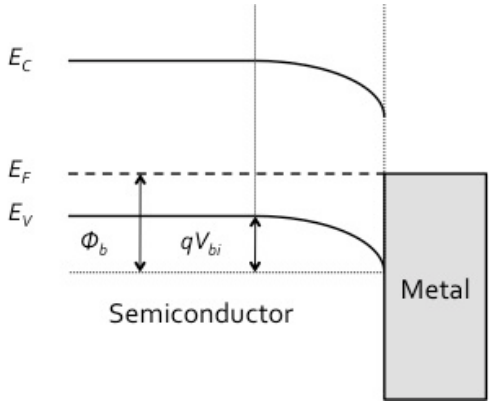

Figure 2.5: Schottky junction between a p-type semiconductor and a metal. A space charge region is formed at the interface, where band bending occurs.

The Schottky barrier height (φ_b) is the energy required for majority carriers flowing to the semiconductor (*Figure 2.5*)[9]. φ_b is given by

$$\varphi_b = E_g - \varphi_m + \chi \tag{2.2}$$

where E_g is the band gap, φ_m is the metal work function and χ is the electron affinity of the semiconductor. The built-in bias (V_{bi}) gives the total amount of the band bending and is determined by the Fermi level difference between the semiconductor and metal before they are brought into contact. The width of the space charge region or depletion region can be calculated by[2],

$$W = \sqrt{\frac{2\varepsilon_s V_{bi}}{qN_a}} \tag{2.3}$$

where ε_s is the permittivity of the semiconductor and N_a is the doping density of the semiconductor.

Schottky junction in the dark

Considering a p-type semiconductor, holes are the majority carriers and the hole flow provides the conduction in the semiconductor. At zero bias, a small current is observed due to thermally activated holes diffusing across the junction, balanced by the drift of electrons. At reverse bias (*Figure 2.6*(a)), as the barrier height is increased, the thermally activated holes become more difficult to pass over the barrier. The leakage current is mainly determined by the drift of electrons from the semiconductor to the metal. When a forward bias is applied (*Figure 2.6*(b)), the barrier height is reduced. Carriers pass more freely over the barrier, and the forward current increases exponentially with the applied bias (*Figure 2.6*(c)).

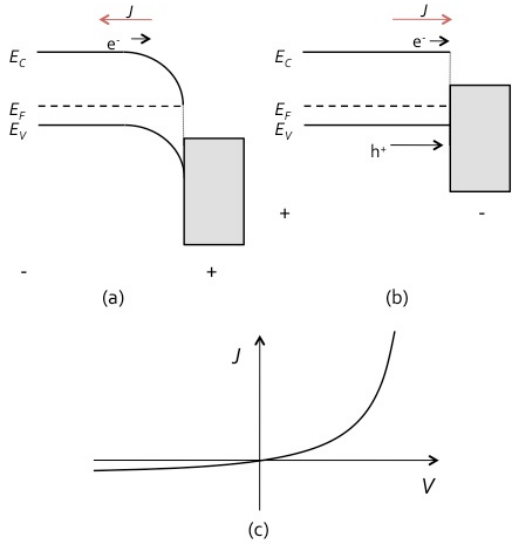

Figure 2.6: (a) p-type semiconductor-metal Schottky junction under reverse bias; (b) p-type semiconductor-metal Schottky junction under forward bias; (c) J-V characteristic curve of a Schottky junction from reverse to forward bias in the dark.

Schottky junction in the light

Considering a p-type semiconductor under illumination, electrons are promoted to the conduction band and drift to the metal by the built-in electric field. Thus under zero bias, for example, a significant current is produced arising from the photogenerated charges. The metal becomes more electron-rich with an increase in Fermi energy. The split of Fermi levels between the semiconductor and the metal by light creates a photovoltage. With increasing illumination intensity, the Fermi level will continue rising until the bands become flat. The flat band voltage is the maximum photovoltage that a Schottky junction can achieve.

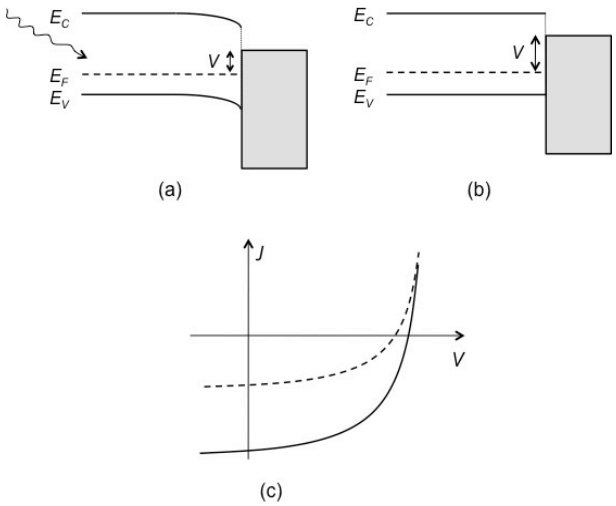

Figure 2.7: Schottky junction band diagram under illumination: (a) under weak illumination; (b) under strong illumination when flat band condition is achieved; (c) J-V characteristic curve of a Schottky junction device under weak (dashed) and strong (solid) illumination.

2.1.3 Characterisations of solar cells

The ability of a solar cell to absorb photons, generate charges and extract them to the external circuit is described by the term quantum efficiency (QE). QE is the

probability of an electron being extracted to the external circuit by an incident photon of energy E. The current density generated by the solar cell in short circuit is given by[2],

$$J_{sc} = q \int b_s(E) QE(E) dE \tag{2.4}$$

where $b_s(E)$ is the number of photons of energy in the range of E to $E + dE$ which are incident on unit area in unit time and q is the electronic charge.

When a load is present in a circuit with an illuminated device, the overall current is decreased and a potential is developed between the terminals. The overall current can be regarded as the superposition of the short circuit current generated by photon absorption and a reverse current caused by the potential built-up under load. The reverse current is the current flowing through a cell in the dark under bias. According to the single-diode model, the dark current density is given by,

$$J_{dark}(V) = J_0(e^{\frac{qV}{nkT}} - 1) \tag{2.5}$$

where J_0 is the reverse saturation current density which is a measure of recombination of a diode, V is the voltage between the cell terminals, n is the ideality factor, k is the Boltzmann constant and T is temperature. The value of ideality factor is dependent upon the recombination type. $n = 1$ if recombination occurs in the neutral region, and $n = 2$ if it occurs in the depletion region[10].

The net current density of a solar cell under illumination is given by

$$J(V) = J_{sc} - J_{dark}(V) = J_{sc} - J_0(e^{\frac{qV}{nkT}} - 1) \tag{2.6}$$

At open circuit, the net current is zero, $J(V) = 0$. The open circuit voltage,

$$V_{oc} = \frac{nkT}{q} \ln\left(\frac{J_{sc}}{J_0} + 1\right) \tag{2.7}$$

Figure 2.8 shows the $J - V$ characteristic curve of a solar cell. The power density delivered by the solar cell is

$$P = JV \tag{2.8}$$

The maximum power point P_{max} is the operating point of a solar cell, corresponding to a voltage V_m and a current density J_m. A term fill factor (FF) is used to describe the squareness of the $J - V$ curve, and is given by the ratio,

$$FF = \frac{J_m V_m}{J_{sc} V_{oc}}. \tag{2.9}$$

The power conversion efficiency is the fraction of the power density at the operating point to the power density of the incident light, P_s,

$$\eta = \frac{J_m V_m}{P_s} = \frac{J_{sc} V_{oc} FF}{P_s}. \tag{2.10}$$

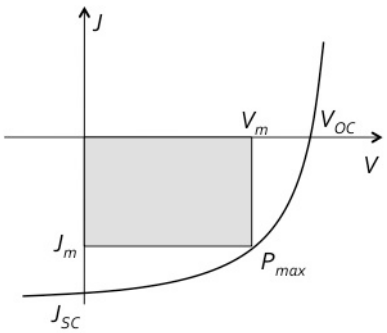

Figure 2.8: Current density-voltage (J-V) characteristic curve of a solar cell. P_{max} is the operating point of the solar cell when the power density is maximum.

In practice, series and shunt resistances are present in solar cells. The series resistance is a result of the semiconductor materials and the electrode contact. There is also some leakage current through the cell, which is high at low shunt resistance. Both resistances can change the fill factor, and an efficient solar cell requires a low series resistance and high shunt resistance[2].

2.2 Solution-processed photovoltaics

Solution-processed photovoltaics have received an enormous amount of research attention within the past decade. The four main solution-processed photovoltaic technologies are organic, dye-sensitised, inorganic thin film and quantum dots. The efficiencies of some of these technologies have exceeded 10% in laboratory. The concept of 'solution-processed' is of particular interest as the photovoltaic materials are processed in form of colloids, which can be coated onto both rigid or flexible substrates using techniques such as doctor blading, spray coating, inkjet printing or slot-die coating, lowering the cost of manufacture and installation[11].

2.2.1 Organic photovoltaics

The first organic solar cell was reported in 1986 using a bilayer structure of copper phthalocyanine (CuPc) and perylene tetracarboxylic derivative, producing a 1% power conversion efficiency[12]. Later in the early 1990s, photo-induced exciton transfer was discovered from conjugated polymers to buckminsterfullerene (C60), marking a major breakthrough in polymer photovoltaics[13,14]. Conjugated polymers and C60 were usually constructed in a bilayer geometry. Such a structure suffered low conversion efficiency due to the short exciton diffusion lengths of conjugated polymers (around 10 nm)[15,16], while optical absorption is insufficient if the absorber layer is only 10 nm thick. Bulk heterojunction was introduced by mixing donor and acceptor molecules to form an interpenetrated network[17,18]. This allows a short distance for an exciton to travel to an interface and a thick absorber layer to be formed. Controlling the bulk morphology is the key to an efficient bulk heterojunction solar cell. Phase separation between donor and acceptor should be at the same scale as the exicton diffusion length while they can vertically segregate to form bi-continuous network to transport separated free electrons and holes to their corresponding electrodes. With the effort of improving device architecture[19–22] and synthesising low band gap polymers[23–25], the efficiency of solution-processed organic photovoltaics have achieved 9%[26] for single junction and 11%[27] for tandem structures.

2.2.2 Dye-sensitised solar cells

Dye-sensitised solar cells (DSSCs) are constructed by having dye molecules absorbed onto a nanostructured metal oxide (TiO_2 or ZnO), followed by a hole conductor which can be a liquid electrolyte or solid-state semiconducting molecules. The first DSSC was reported in 1991[28] and the efficiency rapidly increased to over 10%[29,30]. The narrow band absorption of most dye sensitisers results in low short circuit current in DSSCs. Engineering new sensitisers has been the focus of research to further boost the efficiency[31–33]. More recently, a new class of sensitisers called perovskite has emerged[34–36], recording up to 15% power conversion efficiency[37]. The perovskite materials, $CH_3NH_3PbX_3$ (X = Cl, Br, I), are synthesised through a mixture of PbX_2 and CH_3NH_3X and can be deposited into mesoscopic metal oxides by both solution or vacuum[38] deposition. The electron and hole diffusion lengths for the perovskite were measured at over 1 μm, longer than its 200 nm absorption depth, meaning that it is not required to form a mesoscopic structure. Therefore, depositing perovskite onto mesoscopic Al_2O_3, which is a good insulator, can prevent charges from injecting into the oxides, while the Al_2O_3 acts as a scaffold for the perovskite. This also prompts the question that peroskite solar cells might operate as conventional thin film solar cells rather than excitonic DSSCs.

2.2.3 Inorganic solution-processed photovoltaics

Inorganic solution-processed thin film photovoltaics are mostly quaternary chalcogenides such as copper indium gallium selenide (CIGS) or copper zinc tin

sulphide (CZTS). The development of both materials is pioneered by IBM with 15% efficiency reported for CIGS[39] and 9.6% for CZTS[40]. The CZTS is seen as a promising solar cell material as it only uses earth abundant elements. One of the approach involves in colloidally synthesising CIGS or CZTS nanocrystals, followed by coating on a substrate. A post-deposition selenisation treatment is required to allow grain growth and to passivate defect states. This is usually carried out in an inert atmosphere or under vacuum at 500°C or above. Another approach involves in preparing the precursor ink by dissolving each metal chalcogenide in hydrazine. After film deposition, the metal-hydrazine complexes are then reduced to CIGS or CZTS by annealing. The safety concern over the use of hydrazine is the main hurdle of this technique.

2.2.4 Quantum dot photovoltaics

Colloidal quantum dots have been emerging materials for low cost photovoltaics in the past decade. They are synthesised and processed in solution. They can be applied on both rigid and flexible substrates using spin coating[41–44] and dip coating[45–47]. Manufacture of these devices can be scaled up to roll-to-roll processing[11] for example using inkjet printing[48,49] and to achieve low cost and high throughput production[50]. The quantum confinement effect allows the band gap of the quantum dots to be tuned to allow their optical absorption bandwidths to match with the solar spectrum. Under the quantum confinement regime, quantum dots with sizes less than the exciton Bohr radius results in

confinement of electron and hole wavefunction, leading to a greater band gap energy than the materials' bulk band gap energy[51,52].

The way to distinguish the inorganic quantum dot photovoltaics from the conventional inorganic solution-processed thin film photovoltaic is that rather than growing to bulk crystals, the dimensions of nanoparticles remain in quantum confinement from materials synthesis to final device assembly. This also determines the charge transport mechanism of a QD thin film. As the confinement increases the binding energy of an electron with a hole, charge transport is dominated by the diffusion of an electron-hole pair or an exciton by hopping from dot to dot into a charge separation interface. As the high exciton binding energy results in short diffusion distance, forming bulk heterojunction is seen as an efficient approach to utilise these materials in photovoltaics.

The first polymer/quantum dot bulk heterojunction device was reported by Greenham *et al.*[53] using poly[2-methoxy-5-(2-ethylhexyloxy)-1,4-phenylenevinylene] (MEH-PPV) and CdS or CdSe nanocrystals. The device efficiency was low (0.1%), but an important contribution of this report is that by displacing the surface ligand trioctylphosphine oxide (TOPO) with pyridine, photoluminescence quenching of MEH-PPV increased suggesting that a more efficient charge separation at the organic/inorganic interface. The paper also shows the importance of having phase segregation of nanocrystals to form continuous transport pathways. Realising this issue, interests have been growing

in controlling the polymer/nanocrystal blend morphology[54], especially by using nanorods or nanowires. This was first demonstrated by Huynh *et al.*[55] using CdSe nanorods with poly-3(hexylthiophene) (P3HT), recording a 1.7% efficiency. This concept has also been expanded to ZnO[56–58] and TiO2[59,60] nanorods, reaching over 2% efficiency. More recently, an in-situ method to grow nanocrystals in polymer matrix was reported by Leventis *et al.*[61] to control the morphology. This process involves in depositing a hybrid film from a polymer solution containing a soluble Cd xanthate precursor, which decomposes into CdS nanocrystals upon heating at 150°C. Microscopic studies confirms the interpenetrating nanocrystal network within the polymer matrix using this method and over 2% efficiency has been reported[62].

2.3 PbS quantum dot photovoltaics

2.3.1 Introduction

PbS quantum dots are recognised as one of the "magic" materials for photovoltaic applications, because PbS has a large exciton Bohr radius (18 nm)[63] and low bulk band gap 0.41 eV[64]. These enable the band gap of PbS QDs to be tuned from infrared to visible spectrum (*Figure 2.1*(a)). To make a single junction PbS solar cell, the band gap of the QDs can be tuned to 1.4 eV. Such a band gap can absorb most of the solar spectrum while maintaining a high open circuit voltage[2]. A multi-junction solar cell can also be constructed using a single

material system with dots of various size, which simplifies the fabrication process of a multi-junction device (*Figure 2.9*(b))

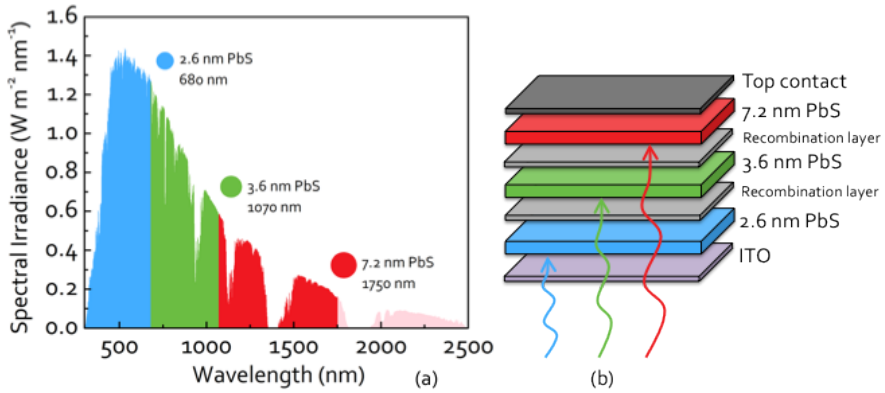

Figure 2.9: (a) PbS quantum dot band gap - size dependance and their absorption bandwidths compared with the solar spectrum (reconstructed from Tang et al.[41]); (b) the concept of a triple-junction solar cell using only PbS quantum dots with difference sizes to achieve optimal light absorption.

2.2.2 Progress of PbS QD photovoltaic

Early investigations of PbS QDs for photovoltaics used them as electron acceptors in organic bulk heterojunction[65–69] devices. PbS QDs was considered an alternative to PCBM for its broadband absorption and larger electron affinity for better charge separation[67]. However, these devices show poor performance with AM1.5 power conversion efficiency only reaching 0.6%[69]. One of the reasons for the low efficiency is attributed to the surface ligands that inhibit charge transfer[70]. A surfactant-free route to synthesise PbS QDs in-situ within the polymer matrix was developed[67,71]. Though this direct synthesis method shows poor control over bulk morphology and size distribution, 0.7% efficiency at low illumination intensity (5 mW/cm^2) has been reported[67]. Besides the polymer/QDs hybrid bulk

heterojunction, another early application of PbS QDs in photovoltaics was to replace organic dyes to sensitise metal oxide[72,73]. QDs were usually deposited into porous TiO_2 by a successive ionic layer absorption and reaction (SILAR) technique[74,75], followed by capping with a hole transporting layer (usually spiro-OMeTAD). Both early approaches have failed to demonstrate an overall benefit of using semiconductor QDs. It was later reported that charge dissociation in these nanostructures is limited by the interfacial Coulombic force between a localised charge in a QD and a counter charge in polymer or metal oxide[76].

A major breakthrough in PbS QD photovoltaics came when bidentate thiol ligands were used to replace oleic acid molecules, creating a cross-linked QD solid film[46,77]. Ethanedithiol(EDT)-treated PbS and PbSe QD Schottky junction devices produced AM1.5 efficiencies up to 3.6%[78] with air stability over 40 hours[79]. Besides a better electrical conductivity of the QD thin film with shorter ligands, the defect states on the QD surface are passivated by the thiol groups[77].

The power conversion efficiencies of PbS QD solar cells have since improved to over 7%[80] to date. Research in QD solar cells is progressing through two aspects of research areas in parallel. First, the electronic transport properties of the QD solids can be improved by modifying the physical and chemical properties of the QDs, particularly the QD surface. In the meantime, device architectures have been tailored to accommodate the need for better optical absorption by increasing the device thickness while maintaining efficient carrier transport. A

combination of both efforts is seen as a "path forward" to achieve highly efficient QD solar cells[81].

2.2.2.1 Recent advances in improving QDs' electronic properties

Surface passivation. The transport properties of QDs, which have abundant surface area, are limited by the defect states residing on the surface. These surface states, also known as mid-gap states, serve as recombination centres, providing a pathway for non-radiative carrier recombination before the charges can be extracted[82,83]. It is essential to passivate these defect states, as they lower the carrier mobility (μ) and recombination lifetime (τ), which determine the carrier diffusion length, l,

$$l = \sqrt{D\tau} \tag{2.11}$$

where D is the diffusion coefficient and $D = \frac{\mu kT}{q}$ according to Einstein relation.

The chemical origins of these surface defects have been identified by X-ray photoelectron spectroscopy (XPS). Oxidised compounds of PbO[84] and $PbSO_3$ induced shallows traps which extend the carrier lifetime, while $PbSO_4$[78,85] is responsible for deep traps or mid-gap states, leading to recombination. Short molecular ligands, including 1,2-ethanedithiol (EDT)[45,46,78], 1,4-benzenedithiol (BDT)[86–88], 3-mercaptopropinoic acid (MPA) and hydrazine, have been used to passivate the QD surface defects. These bidentate molecules can not only displace the insulating oleic acid ligands but also coordinate with exposed QD

surface cations. XPS analysis revealed that only $PbSO_3$ is present on the EDT-treated QD surface[85]. The hole mobility of EDT-treated PbS film is 1×10^{-4} $cm^2V^{-1}s^{-1}$ measured from a QD field-effect transistor (FET). BDT-treated PbS shows a higher FET mobility ($\mu = 2.4 \times 10^{-3}$ $cm^2V^{-1}s^{-1}$)[88], due to electron delocalisation by the conjugated benzene ring[41]. There has been increasing interest in MPA that has both thiol and carboxylate groups, offering the capability to passivate a wider range of defect states. An MPA-capped PbS QD film has one order of magnitude higher mobility than an EDT-treated one[89]. MPA is used most commonly in QD-sensitised TiO_2 devices, as the carboxylate group can anchor the molecule to TiO_2 providing a good electrical linkage between both materials[90–92]. Hydrazine treatment on PbSe has achieved exceptionally high mobility of 0.95 cm^2 $V^{-1}s^{-1}$ measured from an FET[93], but no photovoltaic devices treated only with hydrazine have been successfully made. Semonin *et al.*[94] reported an EDT+hydrazine co-treatment regime on PbSe QDs that can harvest extra photocurrent from multiple exciton generation (MEG). The device showed a striking result of over 100% external quantum efficiency at incident photon energies higher than $2E_g$.

Organic ligand passivation has achieved good device efficiencies of over 5%[95–97]. However, the C-C chain posits steric forces that prevent organic molecules from penetrating trenches on the surface of the QDs[80]. In the meantime, thiol groups have shown good bonding to surface Pb but poor coordination to S, leaving these sites unpassivated so they can readily oxidise[43]. These problems motivated the

development of inorganic ligands that have demonstrated some superior surface passivation properties. The first type of inorganic ligand is based on molecular metal chalcogenide complexes (MCCs)[98]. The MCCs are prepared by dissolving transition metal chalcogenides in hydrazine, for example SnS_2 in N_2H_4 forms $Sn_2S_6^-$ that can attach to the nanocrystal surface[99]. An impressivly high mobility of 16 $cm^2V^{-1}s^{-1}$ has been achieved by CdSe QDs capped with $In_2Se_4^-$ MCC[100]. The first QD photovoltaics with inorganic ligands to be unveiled used halide anions (Cl^-, I^- and Br^-)[43] to passivate PbS QD surface. The passivation was performed in two steps. First, a solution phase treatment of QDs was applied with cadmium chloride–tetradecylphosphonic acid ($CdCl_2$–TDPA) complexes. Cd^{2+} has strong affinity to S atoms while Cl^- can infiltrate those sites that are difficult to access by larger, organic, molecules. This is followed by a solid-state ligand exchange with either cetyltrimethylammonium bromide (CTAB) supplying Br^- ions[43] or MPA[80], both of which should completely remove oleic acid, cross-link the QDs and passivate surface Pb atoms. Both methods have achieved photovoltaic devices with NREL-certified record-breaking efficiencies: 6% for all inorganic passivation ($CdCl_2$–TDPA + CTAB) and 7% for hybrid passivating strategy ($CdCl_2$–TDPA + MPA).

Alloyed QDs. Besides surface passivation, core-shell nanocrystals and alloyed nanocrystals are both promising techniques to benefit from the properties of each composition. In one report, PbS_xSe_{1-x} QDs were synthesised with the composition

of S and Se tuned[101]. A Schottky device using the ternary QDs showed an improved performance with higher J_{sc} and V_{oc} compared with a Schottky PbS or PbSe device.

QD doping. QDs can be doped by introducing dopant into the bulk lattice during synthesis, as well as by modifying the surface properties. Both doping techniques can be performed at a relatively low temperature, compared with temperature needed to dope a bulk semiconductor. Ag-doped PbS QDs has achieved 10^{19} cm^{-3} p-type doping density[102]. For doping by surface ligands, EDT-capped PbS QDs is p-type, while hydrazine-treated QDs show n-type behaviour[93]. Surface oxidation can increase the p-type doping density without loss of mobility as long as ligands remain on the surface[84]. The surface oxide layer can be induced by air annealing at moderate temperature (100°C or below), which has been reported to improve the device fill factor and V_{oc}[44].

One motivation for QD doping is to create a QD p-n junction, such that both sides of the junction can contribute to light absorption[103,104]. To dope PbS QDs to n-type, a strategy of using halogen ions to substitute S has been reported, achieving a 10^{18} cm^{-1} doping density[105]. Comparison among I^-, Br^- and Cl^- shows that I^- is the desirable dopant for photovoltaic application as it produces a high mobility and a low carrier concentration, thus a greater depletion within the active layer. Heterojunction devices containing p-type and n-type PbS QDs have been reported, delivering an NREL-certified efficiency of 6.1%. However, the n-

type doped QDs must be stored and processed strictly in inert atmosphere as any oxidation can switch them to p-type[105].

2.2.2.2 Recent advances in device architecture

Bulk heterojunction. After the report of QD Schottky junction devices, QD/metal oxide (TiO_2 or ZnO) heterojunctions[42,47,106] have been reported showing improved efficiency to over 5%[95,107]. A layer of TiO_2 or ZnO is fabricated to form an Ohmic contact with the TCO, followed by a layer of QDs. The top electrode needs a high work function metal to ohmically contact with QDs[108]. This architecture places the junction in the front of the device where illumination is intense such that most minority carriers can be generated within the depletion region[95]. A thicker film could absorb more photons, but a trade-off has to be made with the charge collection length. The charge collection length is the transport distance of minority carriers within QD film, which is equivalent to the sum of depletion width and minority carrier diffusion length, usually around 150 – 200 nm in total in the case of PbS QD/TiO_2[11]. Therefore, a QD film that is thicker than this length will have limited carrier extraction ability in the region further away from the interface, while complete absorption of solar spectrum requires a micron-thick QD film[81,96].

A QD bulk heterojunction (BHJ) has been created to solve the absorption versus collection length conflict by reducing the transport distance for minority carriers. Some examples of QD bulk heterojunction device architectures are shown in

Figure 2.10. Junctions are extended into the absorber layer such that charge generation can occur close to the interface for efficient charge separation. The first reported QD BHJ is similar to a dye-sensitised solar cell in which a commercial TiO_2 paste was used to create a mesoporous TiO_2 layer which can be infiltrated by QDs[96]. To ensure complete depletion of QDs within the pores, a large TiO_2 particle size (150 – 200 nm) was used to create pore size with a similar dimension, but this yielded a broad pore size distribution. Enhancement of photocurrent can be clearly observed, particularly at visible and infrared wavelengths. Later, vertically-aligned nanopillars or nanowire arrays were used to create BHJs to give more directional transport[97,109–111]. The oriented nanostructures are usually fabricated by nano-imprint lithography[97] or solution deposition processes[109–111]. This offers the opportunity to control the inter-pillar/wire distance to match with the charge collection length. Compared with the mesoporous structure, the oriented arrays could avoid the formation of voids and islands after infiltration[97]. The above approach to prepare BHJ morphology requires pre-patterning of acceptor electrodes, which could undermine the benefit of solution processing. Preparing donor/acceptor BHJ in solution prior to thin film deposition is seen as a more economically viable approach. This was first reported using PbS/Bi_2S_3 blend under the ratio of 1:2, achieving 4.9% efficiency[112], a significant improvement over a planar junction device (1.5%) made from the same QDs[113]. The enhancement is attributed to a prolonged carrier lifetime due to efficient exciton dissociation by the BHJ.

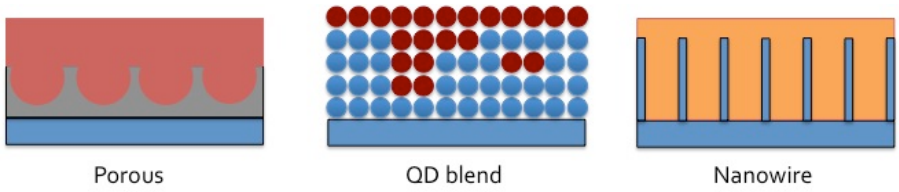

Figure 2.10: Common types of interpenetrated structure for QD bulk heterojunction.

Tandem. A multi-junction solar cell with different band gaps of absorber layers could reduce the thermalisation loss to overcome the Schockley-Queisser limit. The band gap tunability of semiconductor QDs allows the construction of tandem solar cells using a single material system. A sub-cell with large band gap QDs is placed in the front to absorb visible light and the one with small band gap QDs in the back to absorb in the infrared spectrum. The design of interlayers (or recombination layers) that separate each sub-cell must fulfil both electrical and optical constraints[114]. The energy levels of interlayers must be able to accept electrons and holes from each side and allow them to efficiently recombine. They must be optically transparent to allow light pass through to the back-cells, and be chemically and structurally robust to allow QDs to be deposited on the top. The diagrams (*Figure 2.11*) show the recombination layers for QD tandem cells reported by Choi *et al.*[115] and Wang *et al.*[116]. An optimised tandem cell should have matched currents from each of the sub-cells[114]. Therefore, the layer thickness of the small band gap QDs at the back of the cell must be tuned in conjunction with the illumination filtered by the front cell. Overall, the open circuit voltage should be the sum of V_{oc} produced by both sub-cells. The recombination layer reported by Choi *et al.*[115] (*Figure 2.11*(a)) has a shallow work function electron

acceptor (ZnO) in the front cell and a high work function contact (Au) connected to the back cell. A large barrier is created between the ZnO and Au impeding the electron flow from the front to recombine with holes from the back cell. Therefore, a graded recombination layer as in *Figure 2.11*(b) is proposed to form a gradual progression of energy levels to achieve barrier-free conveyance of electrons[116]. The device recorded a V_{oc} of 1.06 V, similar to the V_{oc} sum of the two constituent cells: 0.7 V for the 1.6 eV PbS and 0.39 for the 1 eV PbS.

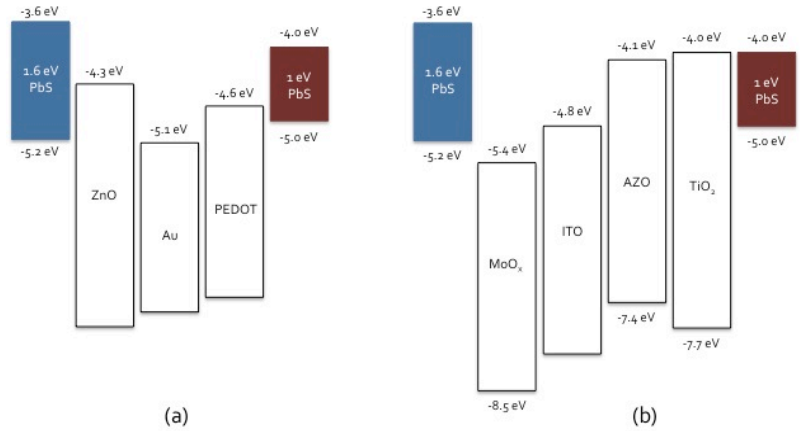

Figure 2.11: Energy level diagrams of different band gap PbS QDs and recombination layers reported by (a) Choi et al.[115] and (b) Wang et al.[116].

2.3 Conclusions and prospects

Semiconducting quantum dots are promising materials for next generation photovoltaics to compete with thin film, organic and dye-sensitised technologies. The rapid growth of QD photovoltaic research has been propelled by the efforts of materials' improvement and innovation of device architecture. The improvement of carrier mobility and carrier lifetime by adapting novel ligands

has significant impact on charge collection ability. With a better understanding of the origins of the QD surface defects, device stability has been improved from being air sensitive to stable in air over weeks. In light of better material properties, the QD device performance can be further improved by optimisation of device architectures that will not only enhance light absorption but also allow efficient charge transfer. The development follows the same route as organic photovoltaics from monolayer to bilayer and to more complex bulk heterojunction structures, where donor-acceptor morphology is the centre of study. The foundation of these morphological studies should be built upon an understanding of the principle of charge generation and separation mechanisms in QDs.

2.4 References

1. Yüncü, H.; Paykoç, E. *Solar Energy Utilization*; Springer: New York, 1987.
2. Nelson, J. *The Physics of Solar Cells*; Imperial College Press: London, 2003.
3. Fonash, S. *Solar Cell Device Physics*; 2nd ed.; Academic Press: San Diego, 2010.
4. Gregg, B. A. Coulomb forces in excitonic solar cells. In *Organic Photovoltaics: Mechanism, Materials, And Devices*; Sun, S.-S. S.; Serdar Sariciftci, N., Eds.; CRC Press: Boca Raton, 2005; pp. 139–160.
5. Mayer, A. C.; Scully, S. R.; Hardin, B. E.; Rowell, M. W.; Mcgehee, M. D. Polymer-Based Solar Cells. *Materials Today* **2007**, *10*, 28–33.
6. Law, M.; Beard, M. C.; Choi, S.; Luther, J. M.; Hanna, M. C.; Nozik, A. J. Determining the Internal Quantum Efficiency of PbSe Nanocrystal Solar Cells with the Aid of an Optical Model. *Nano Letters* **2008**, *8*, 3904–3910.

7. Willis, S. M.; Cheng, C.; Assender, H. E.; Watt, A. A. R. The Transitional Heterojunction Behavior of PbS/ZnO Colloidal Quantum Dot Solar Cells. *Nano Letters* **2012**, *12*, 1522–1526.

8. Zhu, X.; Yang, Q.; Muntwiler, M. Charge-Transfer Excitons at Organic Semiconductor Surfaces and Interfaces. *Accounts of Chemical Research* **2009**, *42*, 1779–1787.

9. Stallinga, P. *Electrical Characterization of Organic Electronic Materials and Devices*; John Wiley & Sons Ltd: Chichester, 2009.

10. Soga, T. *Nanostructured Materials for Solar Energy Conversion*; Elsevier Science: New York, 2006; p. 614.

11. Graetzel, M.; Janssen, R. a. J.; Mitzi, D. B.; Sargent, E. H. Materials Interface Engineering for Solution-Processed Photovoltaics. *Nature* **2012**, *488*, 304–312.

12. Tang, C. W. Two-Layer Organic Photovoltaic Cell. *Applied Physics Letters* **1986**, *48*, 183.

13. Sariciftci, N. S.; Smilowitz, L.; Heeger, a J.; Wudl, F. Photoinduced Electron Transfer from a Conducting Polymer to Buckminsterfullerene. *Science* **1992**, *258*, 1474–1476.

14. Sariciftci, N. S.; Smilowitz, L.; Heeger, a. J.; Wudl, F. Semiconducting Polymers (as Donors) and Buckminsterfullerene (as Acceptor): Photoinduced Electron Transfer and Heterojunction Devices. *Synthetic Metals* **1993**, *59*, 333–352.

15. Mikhnenko, O. V.; Azimi, H.; Scharber, M.; Morana, M.; Blom, P. W. M.; Loi, M. A. Exciton Diffusion Length in Narrow Bandgap Polymers. *Energy & Environmental Science* **2012**, *5*, 6960.

16. Stübinger, T.; Brütting, W. Exciton Diffusion and Optical Interference in Organic Donor–acceptor Photovoltaic Cells. *Journal of Applied Physics* **2001**, *90*, 3632.

17. Yu, G.; Gao, J.; Hummelen, J. C.; Wudl, F.; Heeger, A. J. Polymer Photovoltaic Cells: Enhanced Efficiencies via a Network of Internal Donor-Acceptor Heterojunctions. *Science* **1995**, *270*, 1789–1791.

18. Shaheen, S. E.; Brabec, C. J.; Sariciftci, N. S.; Padinger, F.; Fromherz, T.; Hummelen, J. C. 2.5% Efficient Organic Plastic Solar Cells. *Applied Physics Letters* **2001**, *78*, 841.

19. White, M. S.; Olson, D. C.; Shaheen, S. E.; Kopidakis, N.; Ginley, D. S. Inverted Bulk-Heterojunction Organic Photovoltaic Device Using a Solution-Derived ZnO Underlayer. *Applied Physics Letters* **2006**, *89*, 143517.

20. Waldauf, C.; Morana, M.; Denk, P.; Schilinsky, P.; Coakley, K.; Choulis, S. a.; Brabec, C. J. Highly Efficient Inverted Organic Photovoltaics Using Solution Based Titanium Oxide as Electron Selective Contact. *Applied Physics Letters* **2006**, *89*, 233517.

21. Gilot, J.; Wienk, M. M.; Janssen, R. a. J. Double and Triple Junction Polymer Solar Cells Processed from Solution. *Applied Physics Letters* **2007**, *90*, 143512.

22. Kim, J. Y.; Lee, K.; Coates, N. E.; Moses, D.; Nguyen, T.-Q.; Dante, M.; Heeger, A. J. Efficient Tandem Polymer Solar Cells Fabricated by All-Solution Processing. *Science* **2007**, *317*, 222–225.

23. Liang, Y.; Wu, Y.; Feng, D.; Tsai, S.-T.; Son, H.-J.; Li, G.; Yu, L. Development of New Semiconducting Polymers for High Performance Solar Cells. *Journal of the American Chemical Society* **2009**, *131*, 56–7.

24. Liang, Y.; Feng, D.; Wu, Y.; Tsai, S.-T.; Li, G.; Ray, C.; Yu, L. Highly Efficient Solar Cell Polymers Developed via Fine-Tuning of Structural and Electronic Properties. *Journal of the American Chemical Society* **2009**, *131*, 7792–9.

25. Chen, H.; Hou, J.; Zhang, S.; Liang, Y.; Yang, G.; Yang, Y. Polymer Solar Cells with Enhanced Open-Circuit Voltage and Efficiency. **2009**, *3*, 649–653.

26. He, Z.; Zhong, C.; Su, S.; Xu, M.; Wu, H.; Cao, Y. Enhanced Power-Conversion Efficiency in Polymer Solar Cells Using an Inverted Device Structure. *Nature Photonics* **2012**, *6*, 591–595.

27. Dou, L.; You, J.; Yang, J.; Chen, C.; He, Y.; Murase, S.; Moriarty, T.; Emery, K.; Li, G.; Yang, Y. Tandem Polymer Solar Cells Featuring a Spectrally Matched Low-Bandgap Polymer. *Nature Photonics* **2012**, *6*, 180–185.

28. O'Regan, B. C.; Graetzel, M. A Low-Cost, High-Efficiency Solar Cell Based on Dye-Sensitized Colloidal TiO2 Film. *Nature* **1991**, *353*, 737–739.

29. Chiba, Y.; Islam, A.; Watanabe, Y.; Komiya, R.; Koide, N.; Han, L. Dye-Sensitized Solar Cells with Conversion Efficiency of 11.1%. *Japanese Journal of Applied Physics* **2006**, *45*, L638–L640.

30. Chen, C.; Wang, M.; Li, J.; Pootrakulchote, N.; Alibabaei, L.; Decoppet, J.; Tsai, J.; Grätzel, C.; Wu, C.; Zakeeruddin, S. M.; *et al.* Highly Efficient Light-Harvesting Ruthenium Sensitizer for Thin-Film Dye-Sensitized Solar Cells. *ACS Nano* **2009**, *3*, 3103–3109.

31. Chen, C.-Y.; Wu, S.-J.; Li, J.-Y.; Wu, C.-G.; Chen, J.-G.; Ho, K.-C. A New Route to Enhance the Light-Harvesting Capability of Ruthenium Complexes for Dye-Sensitized Solar Cells. *Advanced Materials* **2007**, *19*, 3888–3891.

32. Jiang, K.-J.; Masaki, N.; Xia, J.-B.; Noda, S.; Yanagida, S. A Novel Ruthenium Sensitizer with a Hydrophobic 2-Thiophen-2-Yl-Vinyl-Conjugated Bipyridyl Ligand for Effective Dye Sensitized TiO2 Solar Cells. *Chemical communications* **2006**, 2460–2462.

33. Jang, S.; Lee, C.; Choi, H.; Ko, J. J.; Lee, J.; Vittal, R.; Kim, K. Oligophenylenevinylene-Functionalized Ru (II)-Bipyridine Sensitizers for Efficient Dye-Sensitized Nanocrystalline TiO2 Solar Cells. *Chemistry of Materials* **2006**, *18*, 5604–5608.

34. Lee, M. M.; Teuscher, J.; Miyasaka, T.; Murakami, T. N.; Snaith, H. J. Efficient Hybrid Solar Cells Based on Meso-Superstructured Organometal Halide Perovskites. *Science* **2012**, *338*, 643–647.

35. Kim, H.-S.; Lee, J.-W.; Yantara, N.; Boix, P. P.; Kulkarni, S. a; Mhaisalkar, S.; Grätzel, M.; Park, N.-G. High Efficiency Solid-State Sensitized Solar Cell-Based on Submicrometer Rutile TiO2 Nanorod and CH3NH3PbI3 Perovskite Sensitizer. *Nano letters* **2013**, *13*, 2412–2417.

36. Heo, J. H.; Im, S. H.; Noh, J. H.; Mandal, T. N.; Lim, C.; Chang, J. A.; Lee, Y. H.; Kim, H.; Sarkar, A.; Nazeeruddin, M. K.; *et al.* Efficient Inorganic-Organic Hybrid Heterojunction Solar Cells Containing Perovskite Compound and Polymeric Hole Conductors. *Nature Photonics* **2013**, *7*, 486–491.

37. Burschka, J.; Pellet, N.; Moon, S.-J.; Humphry-Baker, R.; Gao, P.; Nazeeruddin, M. K.; Grätzel, M. Sequential Deposition as a Route to High-Performance Perovskite-Sensitized Solar Cells. *Nature* **2013**, *499*, 316–319.

38. Liu, M.; Johnston, M. B.; Snaith, H. J. Efficient Planar Heterojunction Perovskite Solar Cells by Vapour Deposition. *Nature* **2013**, *501*, 395–398.

39. Todorov, T. K.; Gunawan, O.; Gokmen, T.; Mitzi, D. B. Solution-Processed Cu(In,Ga)(S,Se)2 Absorber Yielding a 15.2% Efficient Solar Cell. *Progress in Photovoltaics: Research and Applications* **2013**, *21*, 82–87.

40. Todorov, T. K.; Reuter, K. B.; Mitzi, D. B. High-Efficiency Solar Cell with Earth-Abundant Liquid-Processed Absorber. *Advanced Materials* **2010**, *22*, E156–E159.

41. Tang, J.; Sargent, E. H. Infrared Colloidal Quantum Dots for Photovoltaics: Fundamentals and Recent Progress. *Advanced Materials* **2010**, *23*, 12–29.

42. Choi, J. J.; Lim, Y.-F.; Santiago-Berrios, M. B.; Oh, M.; Hyun, B.-R.; Sun, L.; Bartnik, A. C.; Goedhart, A.; Malliaras, G. G.; Abruña, H. D.; *et al.* PbSe Nanocrystal Excitonic Solar Cells. *Nano Letters* **2009**, *9*, 3749–3755.

43. Tang, J.; Kemp, K. W.; Hoogland, S.; Jeong, K. S.; Liu, H.; Levina, L.; Furukawa, M.; Wang, X.; Debnath, R.; Cha, D.; *et al.* Colloidal-Quantum-Dot Photovoltaics Using Atomic-Ligand Passivation. *Nature Materials* **2011**, *10*, 765–771.

44. Zhao, N.; Osedach, T. P.; Chang, L.-Y.; Geyer, S. M.; Wanger, D.; Binda, M. T.; Arango, A. C.; Bawendi, M. G.; Bulovic, V. Colloidal PbS Quantum Dot Solar Cells with High Fill Factor. *ACS Nano* **2010**, *4*, 3743–3752.

45. Luther, J. M.; Law, M.; Beard, M. C.; Song, Q.; Reese, M. O.; Ellingson, R. J.; Nozik, A. J. Schottky Solar Cells Based on Colloidal Nanocrystal Films. *Nano Letters* **2008**, *8*, 3488–3492.

46. Luther, J. M.; Law, M.; Song, Q.; Perkins, C. L.; Beard, M. C.; Nozik, A. J. Structural, Optical, and Electrical Properties of Self-Assembled Films of PbSe Nanocrystals Treated with 1,2-Ethanedithiol. *ACS Nano* **2008**, *2*, 271–280.

47. Luther, J. M.; Gao, J.; Lloyd, M. T.; Semonin, O. E.; Beard, M. C.; Nozik, A. J. Stability Assessment on a 3% Bilayer PbS/ZnO Quantum Dot Heterojunction Solar Cell. *Advanced Materials* **2010**, *22*, 3704–3707.

48. Haverinen, H. M.; Myllylä, R. A.; Jabbour, G. E. Inkjet Printing of Light Emitting Quantum Dots. *Applied Physics Letters* **2009**, *94*, 073108.

49. Singh, B. M.; Haverinen, H. M.; Dhagat, P.; Jabbour, G. E. Inkjet Printing - Process and Its Applications. *Advanced Materials* **2010**, *22*, 673–685.

50. Maenosono, S.; Okubo, T.; Yamaguchi, Y. Overview of Nanoparticle Array Formation by Wet Coating. *Journal of Nanoparticle Research* **2003**, *5*, 5–15.

51. Brus, L. E. A Simple Model for the Ionization Potential, Electron Affinity, and Aqueous Redox Potentials of Small Semiconductor Crystallites. *The Journal of Chemical Physics* **1983**, *79*, 5566.

52. Brus, L. E. Electron–electron and Electron-Hole Interactions in Small Semiconductor Crystallites: The Size Dependence of the Lowest Excited Electronic State. *The Journal of Chemical Physics* **1984**, *80*, 4403.

53. Greenham, N.; Peng, X.; Alivisatos, A. Charge Separation and Transport in Conjugated-Polymer/semiconductor-Nanocrystal Composites Studied by Photoluminescence Quenching and Photoconductivity. *Physical review. B, Condensed matter* **1996**, *54*, 17628–17637.

54. Huynh, W. U.; Dittmer, J. J.; Libby, W. C.; Whiting, G. L.; Alivisatos, A. P. Controlling the Morphology of Nanocrystal–Polymer Composites for Solar Cells. *Advanced Functional Materials* **2003**, *13*, 73–79.

55. Huynh, W. U.; Dittmer, J. J.; Alivisatos, a P. Hybrid Nanorod-Polymer Solar Cells. *Science* **2002**, *295*, 2425–2427.

56. Beek, W. J. E.; Wienk, M. M.; Kemerink, M.; Yang, X.; Janssen, R. a J. Hybrid Zinc Oxide Conjugated Polymer Bulk Heterojunction Solar Cells. *Journal of Physical Chemistry B* **2005**, *109*, 9505–9516.

57. Olson, D. C.; Lee, Y.-J.; White, M. S.; Kopidakis, N.; Shaheen, S. E.; Ginley, D. S.; Voigt, J. a.; Hsu, J. W. P. Effect of Polymer Processing on the Performance of Poly(3-hexylthiophene)/ZnO Nanorod Photovoltaic Devices. *Journal of Physical Chemistry C* **2007**, *111*, 16640–16645.

58. Bouclé, J.; Snaith, H. J.; Greenham, N. C. Simple Approach to Hybrid Polymer/Porous Metal Oxide Solar Cells from Solution-Processed ZnO Nanocrystals. *The Journal of Physical Chemistry C* **2010**, *114*, 3664–3674.

59. Wu, M.-C.; Chang, C.-H.; Lo, H.-H.; Lin, Y.-S.; Lin, Y.-Y.; Yen, W.-C.; Su, W.-F.; Chen, Y.-F.; Chen, C.-W. Nanoscale Morphology and Performance of Molecular-Weight-Dependent Poly(3-hexylthiophene)/TiO2 Nanorod Hybrid Solar Cells. *Journal of Materials Chemistry* **2008**, *18*, 4097.

60. Lin, Y.-Y.; Chu, T.-H.; Li, S.-S.; Chuang, C.-H.; Chang, C.-H.; Su, W.-F.; Chang, C.-P.; Chu, M.-W.; Chen, C.-W. Interfacial Nanostructuring on the Performance of polymer/TiO2 Nanorod Bulk Heterojunction Solar Cells. *Journal of the American Chemical Society* **2009**, *131*, 3644–9.

61. Leventis, H. C.; King, S. P.; Sudlow, A.; Hill, M. S.; Molloy, K. C.; Haque, S. a Nanostructured Hybrid Polymer-Inorganic Solar Cell Active Layers Formed by Controllable in Situ Growth of Semiconducting Sulfide Networks. *Nano letters* **2010**, *10*, 1253–8.

62. Dowland, S.; Lutz, T.; Ward, A.; King, S. P.; Sudlow, A.; Hill, M. S.; Molloy, K. C.; Haque, S. A. Direct Growth of Metal Sulfide Nanoparticle Networks in Solid-State Polymer Films for Hybrid Inorganic-Organic Solar Cells. *Advanced Materials* **2011**, *23*, 2739–2744.

63. Kang, I.; Wise, F. W. Electronic Structure and Optical Properties of PbS and PbSe Quantum Dots. *Journal of the Optical Society of America B* **1997**, *14*, 1632–1646.

64. Hines, M. A.; Scholes, G. D. Colloidal PbS Nanocrystals with Size-Tunable Near-Infrared Emission: Observation of Post-Synthesis Self-Narrowing of the Particle Size Distribution. *Advanced Materials* **2003**, *15*, 1844–1849.

65. McDonald, S. A.; Cyr, P. W.; Levina, L.; Sargent, E. H. Photoconductivity from PbS-Nanocrystal/semiconducting Polymer Composites for Solution-Processible, Quantum-Size Tunable Infrared Photodetectors. *Applied Physics Letters* **2004**, *85*, 2089–2090.

66. McDonald, S. A.; Konstantatos, G.; Zhang, S.; Cyr, P. W.; Klem, E. J. D.; Levina, L.; Sargent, E. H. Solution-Processed PbS Quantum Dot Infrared Photodetectors and Photovoltaics. *Nature Materials* **2005**, *4*, 138–142.

67. Watt, A. A. R.; Blake, D.; Warner, J. H.; Thomsen, E. A.; Tavenner, E. L.; Rubinsztein-Dunlop, H.; Meredith, P. Lead Sulfide Nanocrystal: Conducting Polymer Solar Cells. *Journal of Physics D: Applied Physics* **2005**, *38*, 2006–2012.

68. Rauch, T.; Böberl, M.; Tedde, S. F.; Fürst, J.; Kovalenko, M. V.; Hesser, G.; Lemmer, U.; Heiss, W.; Hayden, O. Near-Infrared Imaging with Quantum-Dot-Sensitized Organic Photodiodes. *Nature Photonics* **2009**, *3*, 332–336.

69. Noone, K. M.; Strein, E.; Anderson, N. C.; Wu, P.-T.; Jenekhe, S. a.; Ginger, D. S. Broadband Absorbing Bulk Heterojunction Photovoltaics Using Low-

Bandgap Solution-Processed Quantum Dots. *Nano Letters* **2010**, *10*, 2635–2639.

70. Saunders, B. R.; Turner, M. L. Nanoparticle-Polymer Photovoltaic Cells. *Advances in Colloid and Interface Science* **2008**, *138*, 1–23.

71. Watt, A. A. R.; Thomsen, E.; Meredith, P.; Rubinsztein-Dunlop, H. A New Approach to the Synthesis of Conjugated Polymer-Nanocrystal Composites for Heterojunction Optoelectronics. *Chemical communications* **2004**, *20*, 2334–2335.

72. Plass, R.; Pelet, S.; Krueger, J.; Grätzel, M. Quantum Dot Sensitization of Organic-Inorganic Hybrid Solar Cells. *Journal of Physical Chemistry B* **2002**, *106*, 7578–7580.

73. Vogel, R.; Hoyer, P.; Weller, H. Quantum-Sized PbS, CdS, Ag2S, Sb2S3, and Bi2S3 Particles as Sensitizers for Various Nanoporous Wide-Bandgap Semiconductors. *Journal of Physicsal Chemistry* **1994**, *98*, 3183–3188.

74. Lee, H.; Leventis, H. C.; Moon, S.-J.; Chen, P.; Ito, S.; Haque, S. a.; Torres, T.; Nüesch, F.; Geiger, T.; Zakeeruddin, S. M.; *et al.* PbS and CdS Quantum Dot-Sensitized Solid-State Solar Cells: "Old Concepts, New Results." *Advanced Functional Materials* **2009**, *19*, 2735–2742.

75. Lee, H. J.; Chen, P.; Moon, S.-J.; Sauvage, F.; Sivula, K.; Bessho, T.; Gamelin, D. R.; Comte, P.; Zakeeruddin, S. M.; Seok, S. Il; *et al.* Regenerative PbS and CdS Quantum Dot Sensitized Solar Cells with a Cobalt Complex as Hole Mediator. *Langmuir* **2009**, *25*, 7602–7608.

76. Cate, S. ten; Schins, J. M.; Siebbeles, L. D. A. Origin of Low Sensitizing Efficiency of Quantum Dots in Organic Solar Cells. *ACS Nano* **2012**, *6*, 8983–8988.

77. Barkhouse, D. A. R.; Pattantyus-Abraham, A. G.; Levina, L.; Sargent, E. H. Thiols Passivate Recombination Centers in Colloidal Quantum Dots Leading to Enhanced Photovoltaic Device Efficiency. *ACS Nano* **2008**, *2*, 2356–2362.

78. Tang, J.; Brzozowski, L.; Barkhouse, D. A. R.; Wang, X.; Debnath, R.; Wolowiec, R.; Palmiano, E.; Levina, L.; Pattantyus-Abraham, A. G.; Jamakosmanovic, D.; *et al.* Quantum Dot Photovoltaics in the Extreme Quantum Confinement Regime: The Surface-Chemical Origins of Exceptional Air- and Light-Stability. *ACS Nano* **2010**, *4*, 869–878.

79. Tang, J.; Wang, X.; Brzozowski, L.; Barkhouse, D. A. R.; Debnath, R.; Levina, L.; Sargent, E. H. Schottky Quantum Dot Solar Cells Stable in Air Under Solar Illumination. *Advanced Materials* **2010**, *22*, 1398–1402.

80. Ip, A. H.; Thon, S. M.; Hoogland, S.; Voznyy, O.; Zhitomirsky, D.; Debnath, R.; Levina, L.; Rollny, L. R.; Carey, G. H.; Fischer, A.; *et al.* Hybrid Passivated Colloidal Quantum Dot Solids. *Nature Nanotechnology* **2012**, *7*, 577–582.

81. Kramer, I. J.; Sargent, E. H. Colloidal Quantum Dot Photovoltaics: a Path Forward. *ACS Nano* **2011**, *5*, 8506–8514.

82. Nagpal, P.; Klimov, V. I. Role of Mid-Gap States in Charge Transport and Photoconductivity in Semiconductor Nanocrystal Films. *Nature Communications* **2011**, *2*.

83. Gao, J.; Johnson, J. C. Charge Trapping in Bright and Dark States of Coupled PbS Quantum Dot Films. *ACS Nano* **2012**, *6*, 3292–3303.

84. Klem, E. J. D.; Shukla, H.; Hinds, S.; MacNeil, D. D.; Levina, L.; Sargent, E. H. Impact of Dithiol Treatment and Air Annealing on the Conductivity, Mobility, and Hole Density in PbS Colloidal Quantum Dot Solids. *Applied Physics Letters* **2008**, *92*, 212105.

85. Konstantatos, G.; Levina, L.; Fischer, A.; Sargent, E. H. Engineering the Temporal Response of Photoconductive Photodetectors via Selective Introduction of Surface Trap States. *Nano Letters* **2008**, *8*, 1446–1450.

86. Fu, H.; Tsang, S.-W.; Zhang, Y.; Ouyang, J.; Lu, J.; Yu, K.; Tao, Y. Impact of the Growth Conditions of Colloidal PbS Nanocrystals on Photovoltaic Device Performance. *Chemistry of Materials* **2011**, *23*, 1805–1810.

87. Tsang, S. W.; Fu, H.; Wang, R.; Lu, J.; Yu, K.; Tao, Y. Highly Efficient Cross-Linked PbS nanocrystal/C60 Hybrid Heterojunction Photovoltaic Cells. *Applied Physics Letters* **2009**, *95*, 183505.

88. Koleilat, G. I.; Levina, L.; Shukla, H.; Myrskog, S. H.; Hinds, S.; Pattantyus-abraham, A. G.; Sargent, E. H. Efficient , Stable Infrared Photovoltaics Based on Solution-Cast Colloidal Quantum Dots. *ACS Nano* **2008**, *2*, 833–840.

89. Jeong, K. S.; Tang, J.; Liu, H.; Kim, J.; Schaefer, A. W.; Kemp, K.; Levina, L.; Wang, X.; Hoogland, S.; Debnath, R.; *et al.* Enhanced Mobility-Lifetime

Products in PbS Colloidal Quantum Dot Photovoltaics. *ACS Nano* **2012**, *6*, 89–99.

90. Hyun, B.; Zhong, Y.; Bartnik, A. C.; Sun, L.; Abrun, H. D.; Wise, F. W.; Goodreau, J. D.; Matthews, J. R.; Leslie, T. M.; Borrelli, N. F. Electron Injection from Colloidal PbS Quantum Dots into Titanium Dioxide Nanoparticles. *ACS Nano* **2008**, *2*, 2206–2212.

91. Robel, I.; Subramanian, V.; Kuno, M.; Kamat, P. V Quantum Dot Solar Cells. Harvesting Light Energy with CdSe Nanocrystals Molecularly Linked to Mesoscopic TiO2 Films. *Journal of the American Chemical Society* **2006**, *128*, 2385–2393.

92. Yu, P.; Zhu, K.; Norman, A. G.; Ferrere, S.; Frank, A. J.; Nozik, A. J. Nanocrystalline TiO2 Solar Cells Sensitized with InAs Quantum Dots. *Journal of Physical Chemistry B* **2006**, *110*, 25451–25454.

93. Talapin, D. V; Murray, C. B. PbSe Nanocrystal Solids for n- and p-Channel Thin Film Field-Effect Transistors. *Science* **2005**, *310*, 86–89.

94. Semonin, O. E.; Luther, J. M.; Choi, S.; Chen, H.-Y.; Gao, J.; Nozik, A. J.; Beard, M. C. Peak External Photocurrent Quantum Efficiency Exceeding 100% via MEG in a Quantum Dot Solar Cell. *Science* **2011**, *334*, 1530–1533.

95. Pattantyus-Abraham, A. G.; Kramer, I. J.; Barkhouse, A. R.; Wang, X.; Konstantatos, G.; Debnath, R.; Levina, L.; Raabe, I.; Nazeeruddin, M. K.; Grätzel, M.; *et al.* Depleted-Heterojunction Colloidal Quantum Dot Solar Cells. *ACS Nano* **2010**, *4*, 3374–3380.

96. Barkhouse, D. A. R.; Debnath, R.; Kramer, I. J.; Zhitomirsky, D.; Pattantyus-Abraham, A. G.; Levina, L.; Etgar, L.; Grätzel, M.; Sargent, E. H. Depleted Bulk Heterojunction Colloidal Quantum Dot Photovoltaics. *Advanced Materials* **2011**, *23*, 3134–3138.

97. Kramer, I. J.; Zhitomirsky, D.; Bass, J. D.; Rice, P. M.; Topuria, T.; Krupp, L.; Thon, S. M.; Ip, A. H.; Debnath, R.; Kim, H.-C.; *et al.* Ordered Nanopillar Structured Electrodes for Depleted Bulk Heterojunction Colloidal Quantum Dot Solar Cells. *Advanced Materials* **2012**, *24*, 2315–2319.

98. Kovalenko, M. V; Scheele, M.; Talapin, D. V Colloidal Nanocrystals with Molecular Metal Chalcogenide Surface Ligands. *Science* **2009**, *324*, 1417–1420.

99. Mitzi, D. B.; Kosbar, L. L.; Murray, C. E.; Copel, M.; Afzali, A. High-Mobility Ultrathin Semiconducting Films Prepared by Spin Coating. *Nature* **2004**, *428*, 299–303.

100. Lee, J.-S.; Kovalenko, M. V; Huang, J.; Chung, D. S.; Talapin, D. V Band-Like Transport, High Electron Mobility and High Photoconductivity in All-Inorganic Nanocrystal Arrays. *Nature Nanotechnology* **2011**, *6*, 348–352.

101. Ma, W.; Luther, J. M.; Zheng, H.; Wu, Y.; Alivisatos, a P. Photovoltaic Devices Employing Ternary PbSxSe1-x Nanocrystals. *Nano Letters* **2009**, *9*, 1699–1703.

102. Liu, H.; Zhitomirsky, D.; Hoogland, S.; Tang, J.; Kramer, I. J.; Ning, Z.; Sargent, E. H. Systematic Optimization of Quantum Junction Colloidal Quantum Dot Solar Cells. *Applied Physics Letters* **2012**, *101*, 151112.

103. Tang, J.; Liu, H.; Zhitomirsky, D.; Hoogland, S.; Wang, X.; Furukawa, M.; Levina, L.; Sargent, E. H. Quantum Junction Solar Cells. *Nano Letters* **2012**, *12*, 4889–4894.

104. Ning, Z.; Zhitomirsky, D.; Adinolfi, V.; Sutherland, B.; Xu, J.; Voznyy, O.; Maraghechi, P.; Lan, X.; Hoogland, S.; Ren, Y.; *et al.* Graded Doping for Enhanced Colloidal Quantum Dot Photovoltaics. *Advanced Materials* **2013**, *25*, 1719–1723.

105. Zhitomirsky, D.; Furukawa, M.; Tang, J.; Stadler, P.; Hoogland, S.; Voznyy, O.; Liu, H.; Sargent, E. H. N-Type Colloidal-Quantum-Dot Solids for Photovoltaics. *Advanced Materials* **2012**, *24*, 6181–6185.

106. Leschkies, K. S.; Beatty, T. J.; Kang, M. S.; Norris, D. J.; Aydil, E. S. Solar Cells Based on Junctions Between Colloidal PbSe Nanocrystals and Thin ZnO Films. *ACS Nano* **2009**, *3*, 3638–3648.

107. Brown, P. R.; Lunt, R. R.; Zhao, N.; Osedach, T. P.; Wanger, D. D.; Chang, L.-Y.; Bawendi, M. G.; Bulović, V. Improved Current Extraction from ZnO/PbS Quantum Dot Heterojunction Photovoltaics Using a MoO3 Interfacial Layer. *Nano Letters* **2011**, *11*, 2955–2961.

108. Debnath, R.; Greiner, M. T.; Kramer, I. J.; Fischer, A.; Tang, J.; Barkhouse, D. A. R.; Wang, X.; Levina, L.; Lu, Z.-H.; Sargent, E. H. Depleted-Heterojunction Colloidal Quantum Dot Photovoltaics Employing Low-Cost Electrical Contacts. *Applied Physics Letters* **2010**, *97*, 023109.

109. Fan, Z.; Razavi, H.; Do, J.; Moriwaki, A.; Ergen, O.; Chueh, Y.-L.; Leu, P. W.; Ho, J. C.; Takahashi, T.; Reichertz, L. a; *et al.* Three-Dimensional Nanopillar-Array Photovoltaics on Low-Cost and Flexible Substrates. *Nature Materials* **2009**, *8*, 648–653.

110. Leschkies, K. S.; Jacobs, A. G.; Norris, D. J.; Aydil, E. S. Nanowire-Quantum-Dot Solar Cells and the Influence of Nanowire Length on the Charge Collection Efficiency. *Applied Physics Letters* **2009**, *95*, 193103.

111. Lan, X.; Bai, J.; Masala, S.; Thon, S. M.; Ren, Y.; Kramer, I. J.; Hoogland, S.; Simchi, A.; Koleilat, G. I.; Paz-Soldan, D.; *et al.* Self-Assembled, Nanowire Network Electrodes for Depleted Bulk Heterojunction Solar Cells. *Advanced Materials* **2013**, *25*, 1769–1773.

112. Rath, A. K.; Bernechea, M.; Martinez, L.; Arquer, F. P. G. De; Osmond, J.; Konstantatos, G. Solution-Processed Inorganic Bulk Nano-Heterojunctions and Their Application to Solar Cells. *Nature Photonics* **2012**, *6*, 529–534.

113. Rath, A. K.; Bernechea, M.; Martinez, L.; Konstantatos, G. Solution-Processed Heterojunction Solar Cells Based on p-Type PbS Quantum Dots and n-Type Bi2S3 Nanocrystals. *Advanced Materials* **2011**, *23*, 3712–3717.

114. Gilot, J.; Wienk, M. M.; Janssen, R. a J. Optimizing Polymer Tandem Solar Cells. *Advanced Materials* **2010**, *22*, E67–E71.

115. Choi, J. J.; Wenger, W. N.; Hoffman, R. S.; Lim, Y.-F.; Luria, J.; Jasieniak, J.; Marohn, J. a; Hanrath, T. Solution-Processed Nanocrystal Quantum Dot Tandem Solar Cells. *Advanced Materials* **2011**, *23*, 3144–3148.

116. Wang, X.; Koleilat, G. I.; Tang, J.; Liu, H.; Kramer, I. J.; Debnath, R.; Brzozowski, L.; Barkhouse, D. A. R.; Levina, L.; Hoogland, S.; *et al.* Tandem Colloidal Quantum Dot Solar Cells Employing a Graded Recombination Layer. *Nature P* **2011**, *5*, 480–484.

Chapter 3 - PbS QDs and Schottky Junction

3.1 Introduction

The blossom of PbS QDs for solar cells was initiated by the discovery that using strong coupling ligands can improve both transport properties and surface passivation of quantum dot solids[1,2]. The progress was also aided by the development of a new synthetic regime to form mono-dispersed QDs[3].

The size of the quantum dots is tuned to yield an optimum band gap of 1.4 eV[4] for single junction devices. Size control of QDs can be achieved by varying reaction temperature, time and ligand-to-co-solvent ratio[5]. A narrow size distribution requires rapid nucleation and slow growth[6]. This can enhance the performance of the QD solar cell devices by allowing close packing and by reducing "quantum traps" due to small-band gap particles[7].

This chapter will present the methodologies for synthesising PbS QDs with different band gaps and for assembly of QDs into solid thin films for solar cell devices. Schottky junction devices were fabricated to study the optimum device thickness and how this relates to the depletion widths and diffusion lengths. The effect of using lower work function top electrodes on open circuit voltage was studied to identify the Schottky junction limitation. The methodologies for QD

synthesis and thin film fabrication presented in this chapter are employed throughout the whole thesis.

3.2 PbS QD synthesis and characterisation

3.2.1 Colloidal synthesis of PbS QDs

PbS QDs were synthesised using a hot injection technique developed by Hines and Scholes[3] with slight modification in precursor concentrations. All syntheses were performed on an air-free Schlenk line. A diagram of the reaction set-up is shown in Figure 3.1.

In a typical synthesis of 1.4 eV PbS QDs, 0.47 g (2 mmol) lead oxide yellow (PbO, Acros Organics), 2 g oleic acid (OA, Sigma-Aldrich) and 10 g octadecene (ODE, 90%, technical grade, Sigma-Aldrich) were added into a three-neck flask. The mixture was heated under vacuum at 90°C for at least 3 hours under vigorous stirring, producing a clear lead-oleate solution. In a dry-box, 210 μL bis(trimethylsilyl) sulphide (aka. hexamethyldisilathiane or $(TMS)_2S$, 1 mmol, Sigma-Aldrich) was mixed with 5 g ODE and loaded into a syringe. $(TMS)_2S$ reacts with moisture in air rapidly to produce H_2S and must be handled with extreme care. The system was switched to nitrogen flow from vacuum and the temperature of the Pb-oleate solution was raised to 120°C. $(TMS)_2S$ was rapidly injected into the flask and the solution turned dark within 3 s indicating nucleation of nanocrystals. The QDs were allowed to grow slowly by using a slow cooling regime in order to focus the size distribution[5,6,8]. Therefore, after

injection, the heating mantle was switched off but not removed. The solution was left to cool slowly to around 30°C in a course of 20 - 30 min.

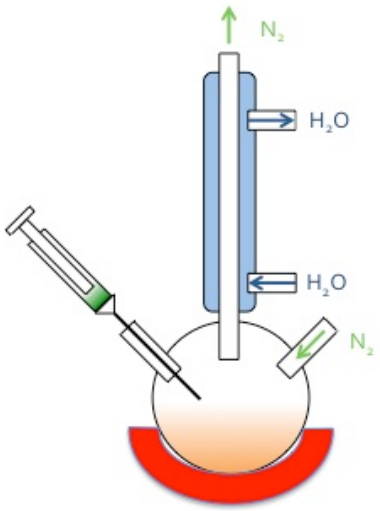

Figure 3.1: A schematic showing the experimental set-up for synthesising PbS QDs.

Sizes of the QDs can be controlled by changing the surfactant:co-solvent ratio and reaction temperature. For synthesising small-sized particles, rapid quenching of the reaction is needed to halt particle growth. This is achieved by soaking the reaction flask into iced water immediately after injection. PbS QDs with band gaps of 0.7, 1.4 and 1.7 eV were synthesised and detailed recipes[9] for synthesising these QDs are listed in Table 1.1.

Table 1.1. Recipes for synthesising PbS QDs with different band gaps.

E_g	PbO	$(TMS_2)S$	Oleic acid	Octadecene	Temperature	Cooling
0.7 eV	0.46 g	210 µL	18 g	10 g	130°C	Slow
1.4 eV	0.46 g	210 µL	2 g	10 g	120°C	Slow
1.7 eV	0.46 g	210 µL	2 g	10 g	60°C	Quenched

3.2.2 Solvent exchange

Solvent exchange is used to separate as-synthesised QDs from the coordinating solvent (e.g. octadecene (ODE)) and replace it with other low viscosity solvents for characterisation and thin film fabrication. It is also employed to remove some side products and unreacted precursors[10]. The liquid from the reaction flask was transferred into a 50 mL centrifuge tube. A polar solvent (acetone, ethanol, methanol or ethyl acetate) was added to precipitate PbS QDs from ODE. It was found that acetone was the best solvent to extract PbS QDs from ODE. The mixture was then centrifuged and the supernatant was decanted. The solid PbS was then dispersed in 5 mL hexane. The precipitation-centrifugation-dispersion process was performed twice more. This time methanol was used to precipitate the QDs from hexane. Repeat use of acetone can result in agglomeration of the QDs. Finally, the PbS QD solids were dried under nitrogen flow. The dry weight of the QDs was measured and then re-dispersed in toluene or hexane. The concentration can be calculated by measuring the dry weight of a 100 μL dispersion. The QDs were stored in a N_2-filled glovebox for further use.

3.2.3 Characterisation of PbS QDs

A microscopic study of PbS QDs was made using a JEOL 2000FX transmission electron microscope (TEM) operated at 200 kV. Optical absorption spectra of the QDs in hexane were measured on a Cary Varian 4000 UV-VIS-NIR spectrophotometer.

The electron micrographs of the as-synthesised PbS QDs of different sizes are shown in Figure 3.2. The nanoparticles are free from aggregation, forming closed-packed arrays of particles spaced from one another, due to the presence of 2.5 nm oleic acid ligands[11]. The mean particle size is an average of the diameters of 100 particles measured from the image.

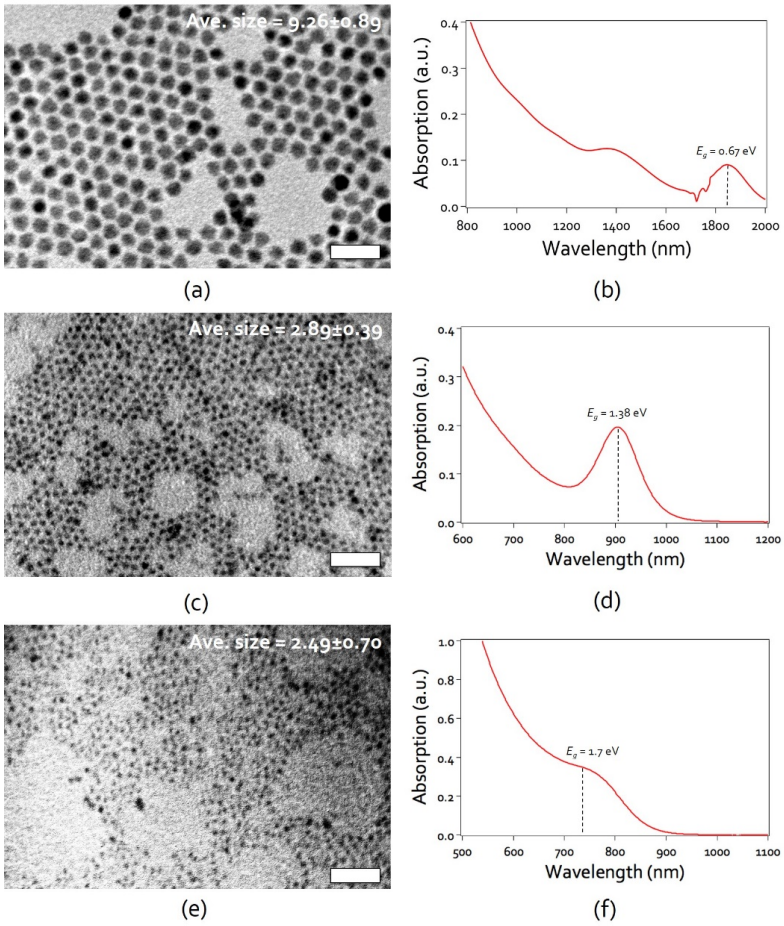

Figure 3.2: (a) (c) (e) TEM micrograph of PbS QDs at different sizes. Scale bar = 30 nm. Average particle size obtained by measuring 100 particles from the TEM micrographs; (b) (d) (f) optical absorption spectra of different sizes of PbS QDs in hexane solution.

Optical absorption spectra of the PbS QDs in hexane are presented in Figure 3.2(b) (d) and (f). An excitonic peak at low energy arising from the $1S_h$-$1S_e$ transition[12,13], defines the band gap. The mean particle sizes and their corresponding band gap energies are plotted in Figure 3.3 (black circles). The red line in Figure 3.3 shows the band gap – size relationship of PbS QDs proposed by Moreels *et al*.[14] as,

$$E_g = 0.41 + (0.0252d^2 + 0.283d)^{-1}, \tag{3.1}$$

where d is the diameter of the particles. The experimental data follows the general trend of the calculated curve with deviations up to 8%, although the exact form of an appropriate fitting is not possible to determine from the three data points.

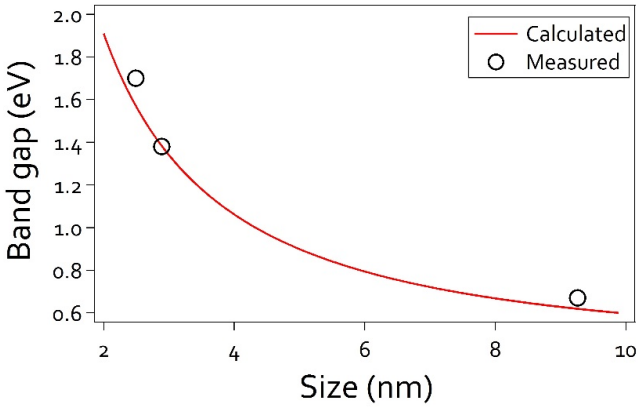

Figure 3.3: Band gap - size relationship of PbS QDs plotted from the equation proposed by Moreels et al.[14]. Black circles are sizes and band gaps measured from TEM and absorption.

3.3 PbS QD Schottky Junction Device

3.3.1 Fabrication of QD thin film device

ITO (indium-doped tin oxide) glass substrates were patterned by etching in an acid etchant (20% HCl/5% HNO_3) at 50°C. The substrates were cleaned by the following procedure: 10 min sonication in de-ionised water with detergent (Decon), 10 min sonication in pure de-ionised water, 5 min immersion in acetone at 60°C, and 5 min immersion in isopropanol at 60°C. The substrates were treated with oxygen plasma for 1 min (March Plasmod, 100 mbar). A layer of PEDOT:PSS was fabricated by spin coating 2 drops of filtered PEDOT:PSS solution at 5000 rpm for 30 s. The film was dried on a hot plate at 150°C for 5 min.

The Schottky junction device was assembled based on 1.4 eV QDs, an optimum band gap for single junction solar cells. Deposition of PbS QDs was performed in a fume hood. Cracks were generated by internal strain when short molecules displaced the long chain oleic acid (Figure 3.4). A layer-by-layer spin coating method was used to solve this problem. During each cycle a new layer of PbS is deposited to fill the cracks underneath. The substrates were set to spin at 2000 rpm. While spinning, one drop of 37.5 mg/mL PbS in toluene was dispensed onto the substrate through a 0.2 μm PTFE filter. For ligand exchange, 2 drops of 2 vol% 1,2-ethanedithiol (EDT) in acetonitrile solution was dispensed onto the spinning substrates. 5 drops of methanol was applied to remove the residual EDT

and 5 drops of toluene or hexane to remove oleic acid. The above process was repeated until the required thickness was obtained. Spin coating of 37.5 mg/mL concentration QD solution at 2000 rpm will yield an approximately 30 nm thick film. Film thicknesses were measured from the device cross-sections imaged on a JEOL 840F scanning electron microscope. After QD thin film deposition, the substrates were transferred into a vacuum chamber for top electrode deposition. Aluminium electrodes were deposited by thermal evaporation at 10^{-6} Torr. The electrodes had a thickness of 100 nm and were deposited at a rate of 0.1 nm/s. A shadow mask was used to define an active area of 0.02035 cm^2.

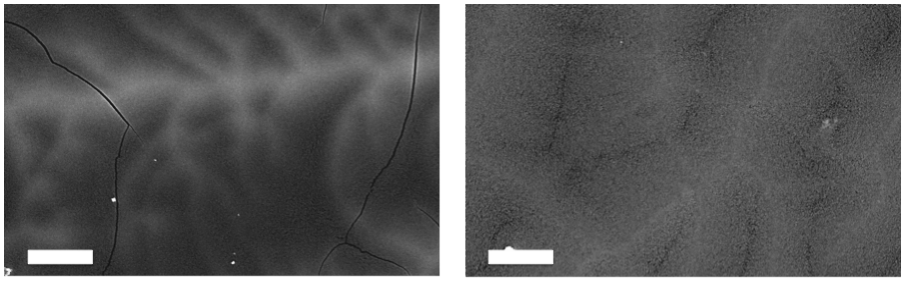

(a) (b)

Figure 3.4: (a) cracks are formed on EDT treated nanocrystal film; (b) by using layer-by-layer spin coating, the cracks are filled. Scale bar = 250 nm.

3.3.2 Characterisation of Schottky junction solar cell devices

3.3.2.1 Methods

All devices were loaded into an airtight chamber for characterisation in inert atmosphere flushed with N_2 constantly. Current-voltage (*I-V*) measurement was performed on a Keithley 2400 SourceMeter. The voltage was swept from -0.5 to 1.0 V at a step size of 0.025 V. An AM1.5 solar spectrum was produced by a

Newport 96000 150 W solar simulator fitted with an AM1.5 filter. The power density of the light source was calibrated with a Thorlabs D3MM thermal sensor. Capacitance-voltage (*C-V*) measurement was performed on an Agilent E4980A option 001 Precision LCR Meter. The modulation frequency was 5000 Hz and the modulation amplitude was 25 mV.

3.3.2.2 Results and discussions

Prior to EDT ligand exchange, devices made from OA-capped PbS QDs show no photovoltaic response (Figure 3.5(a) red lines) due to the electrical insulation by the oleic acid ligands. A good rectification is seen in the *J-V* characteristic curve of the EDT-coupled QD device (Figure 3.5(a) blue line). A Schottky barrier is established at the PbS/Al interface[15,16] (Figure 3.5(c)), providing the driving force for charge separation.

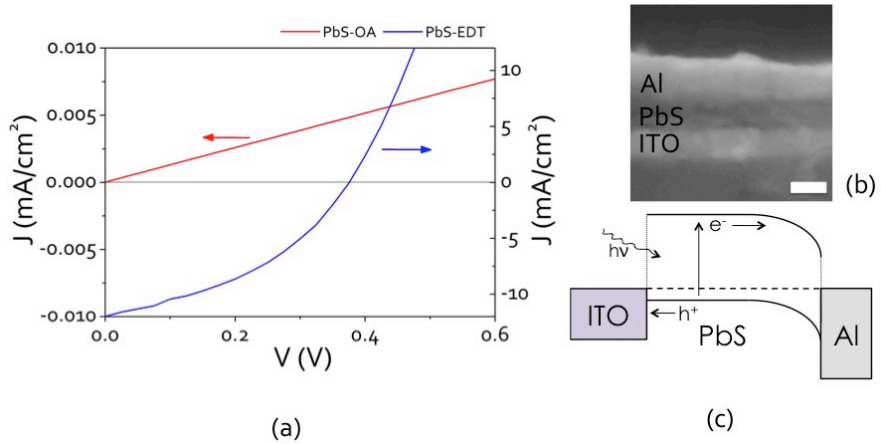

Figure 3.5: (a) current density – voltage (J-V) curve of OA (red) and EDT (blue) -capped PbS QD devices; (b) SEM cross-section image of a PbS Schottky device (scale bar = 100 nm); (c) equilibrium band diagram of PbS/Al Schottky junction.

The performance of these devices was subject to optimisation by varying the PbS layer thickness. Schottky junction devices were fabricated with active layer thickness ranging from 90 to 300 nm (Figure 3.6). The best-performing device consisted of a 90 nm PbS layer, yielding a short circuit current (J_{sc}) of 12 mA/cm^2, an open circuit voltage (V_{oc}) of 0.38 V, a fill factor (*FF*) of 40% and an AM1.5 power conversion efficiency (*PCE*) of 1.8%. The same efficiency has been reported by Johnson *et al.*[17]. Tang *et al.*[18] later report that by allowing some extent of surface oxidation can significantly improve the V_{oc} and *FF* without sacrificing the photocurrent. This highest efficiency Schottky junction device has an efficiency of 3.6%. The enhancement is mainly due to a prolonged carrier lifetime by inducing shallow traps.

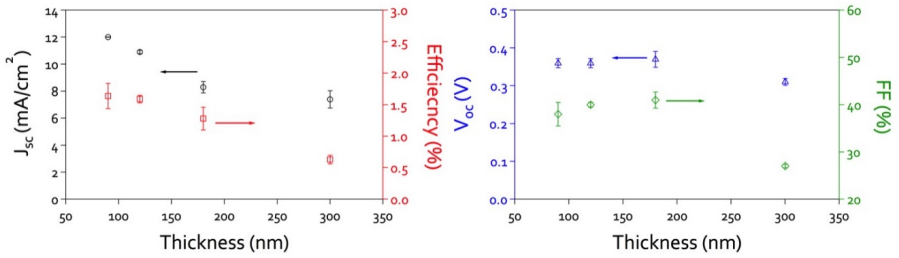

Figure 3.6: Solar cell parameters at different thicknesses (90, 120, 180, 300 nm) of absorber layer. (a) Jsc and Voc; (b) FF and PCE.

Mott-Schottky analysis was employed to gain more knowledge of the doping density, the built-in potential and the width of the Schottky barrier. Capacitance–voltage (*C-V*) measurement was performed to obtain a Mott-Schottky plot (Figure 3.7).

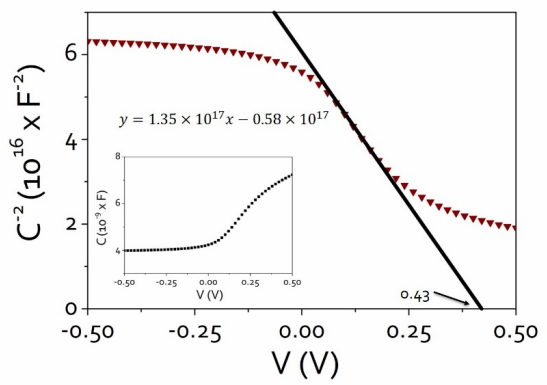

Figure 3.7: Mott-Schottky plot (C^{-2}-V) of PbS-Al Schottky junction and the linear fit of the linear region. Inset: C-V plot of PbS-Al Schottky junction.

When a small forward bias is applied to a Schottky junction device, the relationship between capacitance and applied bias can be written as[19],

$$C^{-2} = \frac{2(V_{bi} - V)}{A^2 q \varepsilon N_a} \tag{3.2}$$

where C is the capacitance, V_{bi} is the built-in potential, V is the applied bias, A is the pixel area, q is the elemental charge, ε is the dielectric constant of the semiconductor, and N_a is the doping density of the semiconductor. The doping density of the PbS QDs was determined at 1.4×10^{17} cm^{-3} from the gradient, using ε = 18 as reported in the literature[18]. The built-in potential is found to be 0.43 V. This can be treated as the upper limit of the V_{oc}. The width of depletion region at equilibrium is[19],

$$W = \sqrt{\frac{2\varepsilon\varepsilon_0 V_{bi}}{qN_a}} \tag{3.3}$$

where ε_0 is the vacuum permittivity and W is the depletion width. Using the calculated values above, the depletion width is estimated to be approximately 80 nm.

Considering a fully depleted device (thickness < 80 nm), charge extraction is efficient as the built-in electric field drifts the electrons and holes to their corresponding electrodes[20] over the full thickness of the device. A thicker device would consist of a quasi-neutral region where diffusion is the major transport mechanism for any charges that are extracted. The electron diffusion length for PbS QD film was reported on the order of 10 nm[21,22]. Carrier extraction would be limited if a device thickness greater than depletion width plus carrier diffusion length. However, a thick absorber layer is capable of absorbing more light, so the thickness is optimal when the device is at the maximum thickness over which charge can be extracted. In summary, carrier extraction is most efficient when the thickness of the active layer is the sum of the width of depletion region and length of carrier diffusion. This explains the 90 nm device is the most efficient of all thicknesses.

3.3.3 Limitation on PbS Schottky Junction Devices

The study of QD Schottky junction is useful to gain understanding of material properties and set a benchmark for the devices in the following chapters. However, device performance based on a Schottky junction has several limitations: the V_{oc} is limited to the offset between the Fermi level and the

electrode work function. Secondly, the short molecular ligands capped on the PbS QDs surface are prone to react with electrode metals[23]. Thirdly, the PbS QD Schottky junction suffers from a low fill factor (40%): as there is only a minimal barrier for holes to the metal, a shunt path for holes is present between the semiconductor and the metal. Considering the first of these problems, a study was made on whether forming a Schottky barrier with low work function metals could increase the barrier height to produce a higher V_{oc}. Using Al (work function ϕ = ~4.1 eV) as the top electrode produced a higher V_{oc} then using Ag (ϕ = ~4.3 eV)(Figure 3.8). However, using scandium (ϕ = ~3.5 eV) a metal with an even lower work function caused a decrease in V_{oc}. It has been reported that an inversion layer is formed with a high Schottky barrier[4,24]. In addition, Fermi-level pinning states are more likely to exist in a low work function metal interface, further degrading the photovoltage[4].

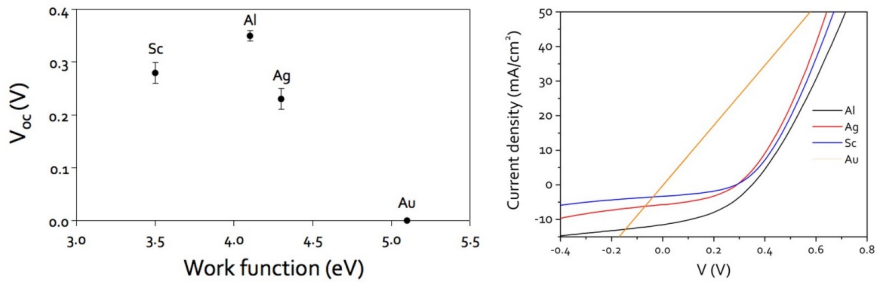

Figure 3.8: V_{oc} of PbS Schottky junction devices with different top electrodes and corresponding J-V curves.

Introducing an n-type semiconductor to form a heterojunction with PbS QDs could avoid the limits of the Schottky junction. This will be discussed in the next chapter.

3.4 Conclusion

Controlling the particle size of PbS QDs can be achieved by adjusting the surfactant-to-co-solvent ratio and injection temperature. By displacing oleic acid with EDT, the *J-V* curve of PbS-Al Schottky junction devices changed from an insulator to a diode behavior with 1.8% efficiency achieved. Mott-Schottky analysis was then performed to study the electronic properties of the materials. By understanding of the nature of band depletion and carrier diffusion, it is possible to determine the optimum device thickness in relation to the length of light absorption and carrier extraction. Further improvement of the Schottky junction is limited. A QD heterojunction structure will be studied in the next chapter.

3.5 References

1. Luther, J. M.; Law, M.; Song, Q.; Perkins, C. L.; Beard, M. C.; Nozik, A. J. Structural, Optical, and Electrical Properties of Self-Assembled Films of PbSe Nanocrystals Treated with 1,2-Ethanedithiol. *ACS Nano* **2008**, *2*, 271–280.

2. Barkhouse, D. A. R.; Pattantyus-Abraham, A. G.; Levina, L.; Sargent, E. H. Thiols Passivate Recombination Centers in Colloidal Quantum Dots Leading to Enhanced Photovoltaic Device Efficiency. *ACS Nano* **2008**, *2*, 2356–2362.

3. Hines, M. A.; Scholes, G. D. Colloidal PbS Nanocrystals with Size-Tunable Near-Infrared Emission: Observation of Post-Synthesis Self-Narrowing of the Particle Size Distribution. *Advanced Materials* **2003**, *15*, 1844–1849.

4. Nelson, J. *The Physics of Solar Cells*; Imperial College Press: London, 2003.

5. Yin, Y.; Alivisatos, a P. Colloidal Nanocrystal Synthesis and the Organic-Inorganic Interface. *Nature* **2005**, *437*, 664–70.

6. Murray, C. B.; Norris, D. J.; Bawendi, M. G. Synthesis and Characterization of Nearly Monodisperse CdE (E = S, Se, Te) Semiconductor Nanocrystallites. *Journal of American Chemical Society* **1993**, *115*, 8706–8715.

7. Zhitomirsky, D.; Kramer, I. J.; Labelle, A. J.; Fischer, A.; Debnath, R.; Pan, J.; Bakr, O. M.; Sargent, E. H. Colloidal Quantum Dot Photovoltaics: The Effect of Polydispersity. *Nano Letters* **2012**, *12*, 1007–12.

8. Fu, H.; Tsang, S.-W.; Zhang, Y.; Ouyang, J.; Lu, J.; Yu, K.; Tao, Y. Impact of the Growth Conditions of Colloidal PbS Nanocrystals on Photovoltaic Device Performance. *Chemistry of Materials* **2011**, *23*, 1805–1810.

9. Rath, A. K.; Bernechea, M.; Martinez, L.; Konstantatos, G. Solution-Processed Heterojunction Solar Cells Based on p-Type PbS Quantum Dots and n-Type Bi2S3 Nanocrystals. *Advanced Materials* **2011**, *23*, 3712–3717.

10. Cattley, C. a; Stavrinadis, A.; Beal, R.; Moghal, J.; Cook, A. G.; Grant, P. S.; Smith, J. M.; Assender, H.; Watt, A. a R. Colloidal Synthesis of Lead Oxide Nanocrystals for Photovoltaics. *Chemical Communications* **2010**, *46*, 2802–2804.

11. Wang, D.; Baral, J. K.; Zhao, H.; Gonfa, B. A.; Truong, V.-V.; Khakani, M. A. El; Izquierdo, R.; Ma, D. Controlled Fabrication of PbS Quantum-Dot/carbon-Nanotube Nanoarchitecture and Its Significant Contribution to Near-Infrared Photon-to-Current Conversion. *Advanced Functional Materials* **2011**, *21*, 4010–4018.

12. Nootz, G.; Padilha, L. a; Olszak, P. D.; Webster, S.; Hagan, D. J.; Stryland, E. W. Van; Levina, L.; Sukhovatkin, V.; Brzozowski, L.; Sargent, E. H. Role of Symmetry Breaking on the Optical Transitions in Lead-Salt Quantum Dots. *Nano Letters* **2010**, *10*, 3577–82.

13. Gesuele, F.; Sfeir, M. Y.; Murray, C. B.; Heinz, T. F.; Wong, C. W. Biexcitonic Effects in Excited States of PbS Quantum Dots. *Nano Letters* **2012**, *12*, 2658–2664.

14. Moreels, I.; Lambert, K.; Smeets, D.; Muynck, D. De; Nollet, T.; Martins, J. C.; Vanhaecke, F.; Vantomme, A.; Delerue, C.; Allan, G.; *et al.* Size-Dependent Optical Properties of Colloidal PbS Quantum Dots. *ACS Nano* **2009**, *3*, 3023–30.

15. Luther, J. M.; Law, M.; Beard, M. C.; Song, Q.; Reese, M. O.; Ellingson, R. J.; Nozik, A. J. Schottky Solar Cells Based on Colloidal Nanocrystal Films. *Nano Letters* **2008**, *8*, 3488–3492.

16. Clifford, J. P.; Johnston, K. W.; Levina, L.; Sargent, E. H. Schottky Barriers to Colloidal Quantum Dot Films. *Applied Physics Letters* **2007**, *91*, 253117.

17. Johnston, K. W.; Pattantyus-Abraham, A. G.; Clifford, J. P.; Myrskog, S. H.; MacNeil, D. D.; Levina, L.; Sargent, E. H. Schottky-Quantum Dot Photovoltaics for Efficient Infrared Power Conversion. *Applied Physics Letters* **2008**, *92*, 151115.

18. Tang, J.; Brzozowski, L.; Barkhouse, D. A. R.; Wang, X.; Debnath, R.; Wolowiec, R.; Palmiano, E.; Levina, L.; Pattantyus-Abraham, A. G.; Jamakosmanovic, D.; *et al.* Quantum Dot Photovoltaics in the Extreme Quantum Confinement Regime: The Surface-Chemical Origins of Exceptional Air- and Light-Stability. *ACS Nano* **2010**, *4*, 869–878.

19. Stallinga, P. *Electrical Characterization of Organic Electronic Materials and Devices*; John Wiley & Sons Ltd: Chichester, 2009.

20. Johnston, K. W.; Pattantyus-Abraham, A. G.; Clifford, J. P.; Myrskog, S. H.; Hoogland, S.; Shukla, H.; Klem, E. J. D.; Levina, L.; Sargent, E. H. Efficient Schottky-Quantum-Dot Photovoltaics: The Roles of Depletion, Drift, and Diffusion. *Applied Physics Letters* **2008**, *92*, 122111.

21. Kramer, I. J.; Zhitomirsky, D.; Bass, J. D.; Rice, P. M.; Topuria, T.; Krupp, L.; Thon, S. M.; Ip, A. H.; Debnath, R.; Kim, H.-C.; *et al.* Ordered Nanopillar Structured Electrodes for Depleted Bulk Heterojunction Colloidal Quantum Dot Solar Cells. *Advanced Materials* **2012**, *24*, 2315–2319.

22. Graetzel, M.; Janssen, R. a. J.; Mitzi, D. B.; Sargent, E. H. Materials Interface Engineering for Solution-Processed Photovoltaics. *Nature* **2012**, *488*, 304–312.

23. Tang, J.; Wang, X.; Brzozowski, L.; Barkhouse, D. A. R.; Debnath, R.; Levina, L.; Sargent, E. H. Schottky Quantum Dot Solar Cells Stable in Air Under Solar Illumination. *Advanced Materials* **2010**, *22*, 1398–1402.

24. Demoulin, E.; Vandewiele, F. Inversion Layer at the Interface of Schottky Diodes. *Solid-State Electronics* **1974**, *17*, 825–833.

Chapter 4 - PbS/ZnO Quantum Dot Heteorjunction

4.1 Introduction

The previous chapter shows the QD-metal Schottky junction configuration places some limits on the QD device performance. In this chapter, a QD donor-acceptor heterojunction is designed to overcome this problem. ZnO nanoparticles are used as the electron acceptor. ZnO is an n-type semiconductor with good electron mobility[1] and has been used for various optoelectronic applications (transparent conductors[2], field-effect transistors[3,4], and light-emitting diodes[5], etc.). ZnO nanoparticles can be synthesised at low temperature using a facile method without the need to use any surfactant. Depending on reaction conditions the particle can grow isotropically or as nanorods or nanowires, allowing more complex nanostructures to be built for solar cell applications[6–8].

A new design of solar cell device architecture of ITO/PEDOT:PSS/PbS/ZnO/Al is presented in this chapter[9]. The best-performing device showed 3% AM1.5 power conversion efficiency. The key questions to address in this chapter are:

1) whether using a heterojunction structure can improve the device performance;

2) whether the junction operating mechanism of quantum dot heterojunction is excitonic, depleted p-n, or a combination of both.

The work in this chapter was conducted in collaboration with Dr Shawn Willis in our group. All materials synthesis and device fabrication were solely performed by me. Device characterisation and data analysis were performed jointly with equal contribution.

4.2 Methodology

4.2.1 Synthesis of ZnO nanoparticles

The ZnO nanoparticles were synthesised using the sol-gel method based on that reported by Pacholski *et al.*[10] with a slight modification to the precursor concentration. A zinc precursor was prepared by dissolving 0.002 mol zinc acetate dihydrate (technical grade, Riedel-de Haën) in 100 mL methanol and stirred at 60°C. To this 0.002 mol potassium hydroxide (Fisher, laboratory reagent grade) dissolved in 50 mL methanol was added drop-wise through filter paper. The solution first turned turbid and then became clear after approximately 10 - 20 minutes. The reaction was kept at 60°C for 2 hr 30 min after which ZnO nanoparticles started to precipitate from the solution. The solid was collected by centrifugation and re-dispersed in methanol. The centrifugation/re-dispersion cycle was performed three times. Finally, the nanoparticles were re-dispersed in chloroform to a concentration of 40 mg/mL. The nanoparticles were stored in air and stable for about two weeks.

4.2.2 Fabrication of PbS-ZnO heterojunction devices

1.4 eV PbS QD at 37.5 mg/mL concentration was used for solar cell device fabrication. PbS QD layers were fabricated using layer-by-layer spin coating as described in Chapter 3. A 100 nm layer of ZnO was spin coated on top of the PbS at 1000 rpm for 1 min. Al electrodes were deposited by thermal evaporation at 10^{-6} Torr to a thickness of 100 nm at a deposition rate of 0.1 nm/s. Electrodes were patterned using a shadow mask to define an active area of 0.03 cm^2.

4.2.3 Solar cell device characterisation

Devices were mounted into a sealed chamber and continuously flushed with N_2 during testing. Capacitance-voltage measurements were performed with the sample in the dark using an Agilent E4980A opt001 LCR meter at a bias between -2 V and 2 V at 0.02 V intervals. The AC signal was set to 25 mV and 500 Hz.

For external quantum efficiency measurement, devices were illuminated by a halogen lamp connected to an Oriel Conerstone 130 monochromator. The intensity of the light source was calibrated using a Newport 818 UV enhanced silicon photodetector for wavelength from 400 - 1075 nm and a Newport 918 IR germanium photodetector for wavelength from 1080 – 1200 nm. The current signal was measured with a Keithley 6845 picoammeter.

4.3 Characterisation of PbS-ZnO heterojunction devices

4.3.1 UV photodoping of ZnO

A schematic of the device architecture and a cross-section SEM image of the device stack are shown in Figure 4.1. It is known that oxygen absorbed onto the ZnO surface forms electron traps, decreasing the conductivity of the ZnO[11]. UV photodoping has been reported as an effective method to cause oxygen desorption from the ZnO surface, increasing the conductivity[12–14]. The schematic in Figure 4.2 illustrates the O_2 desorption process from the ZnO surface on exposure to UV and re-absorption of O_2 when exposed to ambient conditions[12]. UV-excited electrons generate free holes that could migrate to the ZnO surface and free trapped O_2 molecules, leaving mobile electrons in the ZnO.

Administrator 29/7/2013 14:43
Comment [1]: Think? Maybe a semiconductor conductiviety/mobility/carrier conc in the range XXXXX

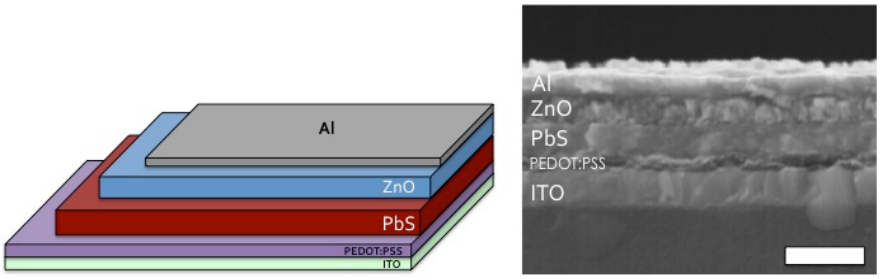

Figure 4.1: Device architecture of PbS/ZnO heterojunction device and cross-section SEM image of the device stack. (Scale bar = 300 nm)

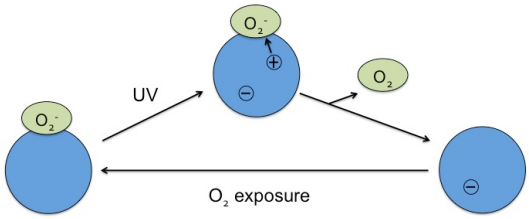

Figure 4.2: The physical process of ZnO UV photodoping and re-absorption of O_2. Adapted from Lakhwani et al.[12].

The photodoping of ZnO was performed in an N_2 atmosphere by removing the 420 nm filter from the solar simulator. It is believed that only a fraction of UV light was able to reach the ZnO, with the majority was being absorbed by the glass, ITO, PEDOT:PSS and PbS QDs. Figure 4.3(a) shows the evolution of J_{sc} and *PCE* with exposure time. Figure 4.3(b) shows the *J - V* characteristic curves of the best-performing device before and after UV doping. An undoped device produced a low short circuit current density (2.5 mA/cm^2) and a poor fill factor (36%). The UV illumination onto the device increases the photocurrent. The current density saturates after 10 min exposure to UV. An increase in fill factor is also observed, which can be attributed to a decrease in series resistance R_s from 94 to 32 Ω cm^2 as the ZnO became more conductive. A champion device was obtained after careful selection of absorber layer thickness. The device has a power conversion efficiency of 3%, producing a J_{sc} of 11.1 mA/cm^2, a V_{oc} of 0.55 V and a *FF* of 51%.

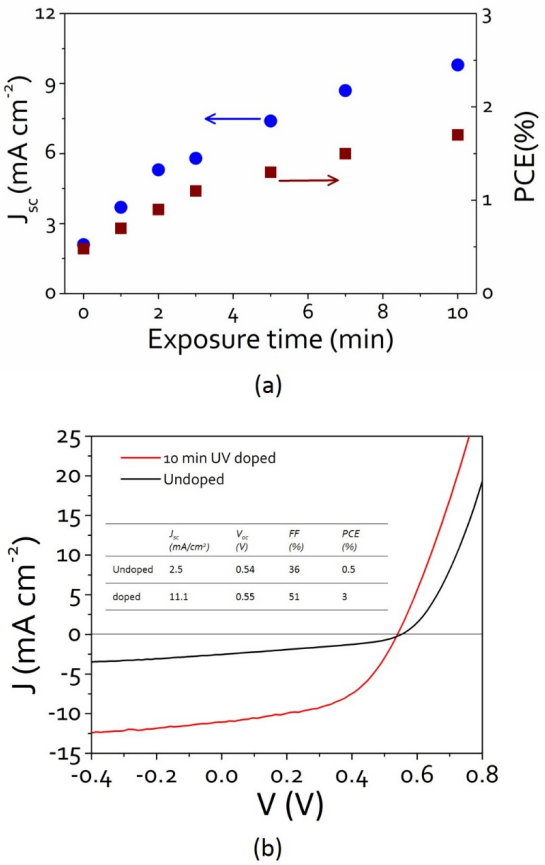

Figure 4.3: (a) J_{sc} and AM1.5 efficiency as a function of UV exposure time; (b) light J-V characteristic curve of the best PbS/ZnO heterojunction device before and after UV photodoping.

Exposure of the devices to air allows oxygen to be re-absorbed on the ZnO surfaces, leading to a rapid degradation of J_{sc}. However, the J_{sc} could recover again once the device was brought into an N_2 atmosphere and treated with UV.

4.3.2 Thickness optimisation

PbS thicknesses of 75, 125, 175, 250 nm were fabricated to identify the optimum absorber layer thickness. This optimum thickness is expected to be the same or

similar to the charge extraction length such that the device has the maximum thickness over which all charges can be collected while allowing it to absorb more photons than a thinner device. All devices were measured after exposure to UV for 10 min. The solar cell parameters versus PbS thickness are shown in Figure 4.4. The device with 125 nm active layer thickness yielded the highest efficiency.

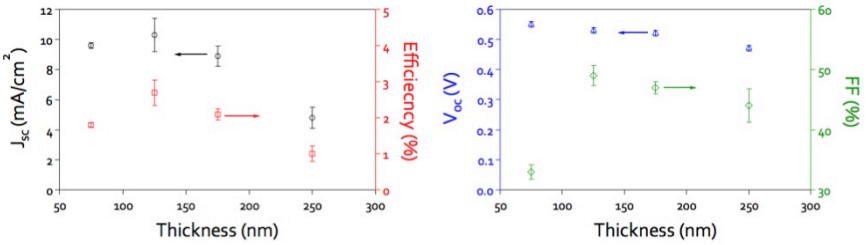

Figure 4.4: Device parameters as a function of absorber layer thickness.

Capacitance-voltage (*C-V*) measurements were performed to determine the depletion width of the junction. In contrast to a Schottky junction device, the depletion region can lie in both the PbS and ZnO semiconductor layers, dependent upon the carrier concentration of each material[15]. The *C-V* curves of the devices with different thicknesses were obtained at 500 Hz shown in Figure 4.5.

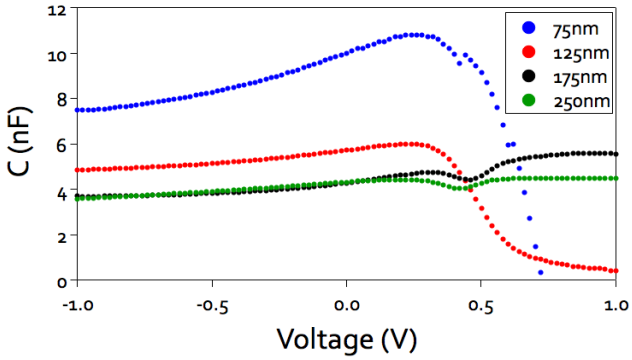

Figure 4.5: C-V curves of PbS/ZnO heterojunction devices with different thickness.

Figure 4.5 shows that at reverse bias the two thicker devices (175 and 250 nm) have nearly the same capacitance while capacitance of the two thinner devices (75 and 125 nm) decreases with increasing device thickness. The heterojunction can be modelled as a parallel-plate capacitor, the capacitance of which is determined by the width of the depletion region[16]. The result indicates that the two thinner devices are possibly fully depleted such that the capacitance is determined by the distance between the two electrodes. The two thicker devices consist of a depleted region and a neutral (non-depleted) region. The width of the depletion region can be calculated based on the capacitance of a parallel-plate capacitor,

$$W = \frac{\varepsilon\varepsilon_0 A}{C}. \tag{4.1}$$

Carrier extraction via linear increasing voltage (CELIV) was employed to determine the dielectric constant ε of the QD film. In this experiment, a triangular voltage pulse is applied to the device with a rate of increase, R, and the

corresponding transient current density is monitored. The dielectric constant can be obtained using[17]

$$\varepsilon = j_0 d / R \varepsilon_0 \tag{4.2}$$

where d is the thickness of the QD film and j_0 is the current density, as indicated in Figure 6. Calculating the ε for each of the different thicknesses, a ε value of 22±2 is obtained. This dielectric constant value is in agreement with the literature value, 20, estimated by using Maxwell-Garnett effective medium theory by Tang *et al.*[18]. The estimated value is a combination of the dielectric constants of bulk PbS and the ligands, assuming volume fraction of PbS is 50% in the matrix. Using the measured capacitance value 4.31 at zero bias (Figure 4.5) for the two fully depleted devices, the depletion width is calculated, using equation (4.1), to be 136 nm, agreeing with observation from the *C-V* data (Figure 4.5), which suggests a depletion width between 125nm and 175nm

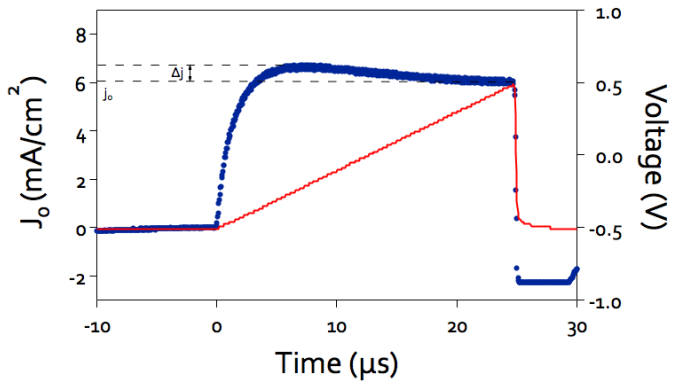

Figure 4.6: CELIV data of the 125 nm device. A transient current was produced (blue) by applying a triangular voltage pulse (red).

External quantum efficiency was measured for the devices with different PbS layer thicknesses to study the relationship between light absorption and charge extraction (Figure 4.7).

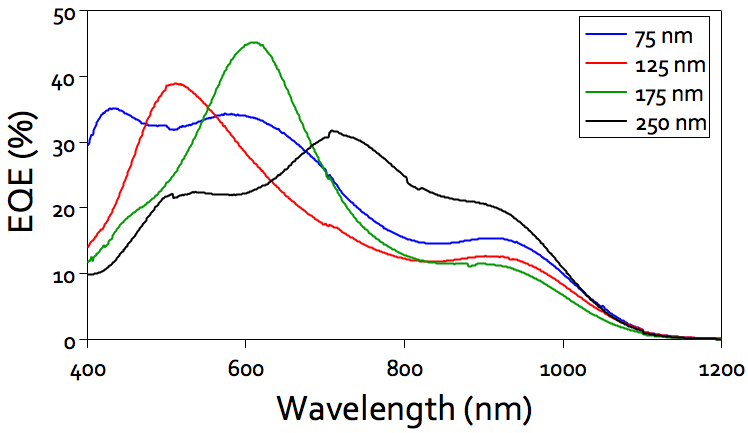

Figure 4.7: External quantum efficiency spectra of PbS/ZnO devices with different thicknesses.

For the thinnest 75 nm device, the most intense peak lies at around 430 nm. With increasing device thickness, a red shift of this EQE peak is observed (moving from 430 nm in the 75 nm device, through 500 nm and 600 nm in the 125 nm and 175 nm devices, to 720 nm in the 250 nm thick device), corresponding to a decrease in EQE at the short wavelength region.

A model is proposed here that across a QD absorber layer three regions could exist in a heterojunction device depending upon the device thickness: a depletion region, a quasi-neutral region and a dead zone. A diagram of this model is shown in Figure 4.8. In a fully depleted thin device (e.g. the 75 nm device in our case),

charge carriers can drift across the whole layer by the built-in electric field at the junction interface. When a device is made thicker, it could contain the complete depletion region, beyond which there exists a quasi-neutral region, where charges are able to diffuse into the depletion region and then drift to the electrodes. The length of the quasi-neutral region is defined by the minority carrier diffusion length which is reported at 10 - 20 nm for PbS QDs[19]. A device that is thicker than the width of depletion region plus the quasi-neutral region will form a region where charges generated cannot be extracted. This region is called "dead zone"[20] because all charges will recombine.

The above model must be considered in conjunction with photon absorption profile of a semiconductor. High energy photons have a shorter absorption depth than low energy photons[21]. In the current device geometry, short wavelength photons are absorbed at the front of the device near the ITO. Long wavelength photons can penetrate further into the device, being absorbed closer to the junction interface. It is possible that for a thin device long wavelength photons penetrate through the whole device with only a fraction being absorbed.

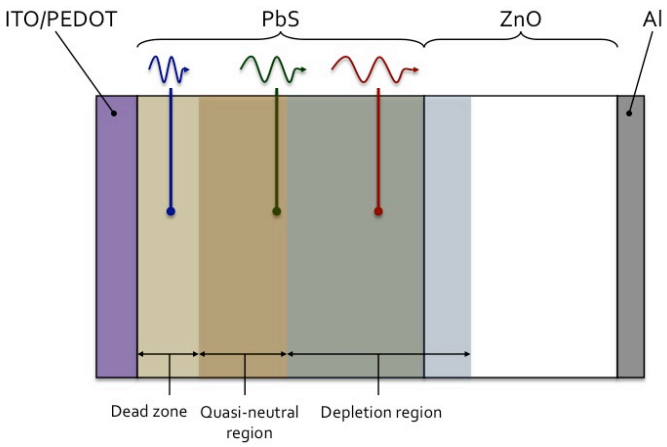

Figure 4.8: The proposed model that a QD layer can consist of a depletion region, a quasi-neutral region and a dead zone. (Schematic created by Dr Shawn Willis)

The observed absorption spectra, shown in Figure 4.9(a) are consistent with this idea. It is evident that a thicker device is in general absorbing more photons of wavelength up to 800 nm. The Beer-Lambert law can be used here to estimate the absorption coefficient (α) by

$$abs = \alpha L, \tag{4.3}$$

where *abs* is absorbance and *L* is the optical length, which is the PbS thickness in this case. $1/\alpha$ can be regarded as the optical penetration depth[21]. The α value for each wavelength is extracted by plotting the absorbance against the device thickness (Figure 4.9(b)). The estimated optical penetration depth from 400 to 700 nm is shown in Figure 4.9(c). The short wavelength light can penetrate a few hundred nanometres into the PbS QD film, while long wavelength photons have a penetration depth much greater than the QD film thicknesses reaching a few

thousand nanometres. As the device is made thicker, short wavelength photons are absorbed in the dead zone and long wavelength photons excite charge carriers in the extraction zone. This estimation also shows that a few micron thick PbS QD film is required to absorb all the visible light. There are some limitations of this technique: 1) the single pass absorption does not correct any reflection and scattering by the samples (this can be corrected if an integrating sphere is used). 2) The absorber layers is too thin to have significant absorption of long wavelength light. Therefore, the α value may be distorted at these wavelengths. Besides the red shifts of the EQE peaks (Figure 4.7) of the thicker devices and the excitonic absorption peaks at 950 nm for all devices, there are two noticeable peaks at 470 nm and 500 nm wavelengths for the 175 nm and 250 nm devices, respectively. An explanation to this is that high energy photons can generated longer-lived excitons that can migrate further than an exciton generated by low energy photons[22]. The peak may exist in the two thin devices but are overshadowed by the main peaks.

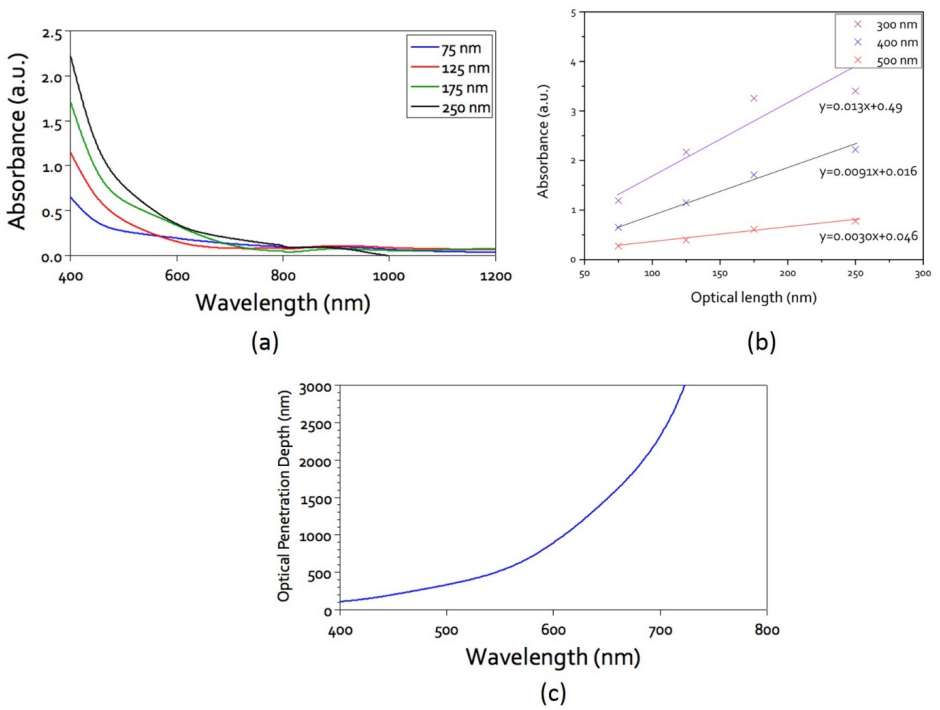

Figure 4.9: (a) optical absorption spectra of PbS QD film with different thickness; (b) absorbance versus optical length or PbS layer thickness at different wavelengths 300 nm, 400 nm and 500 nm; (b) optical penetration depth in PbS at different wavelength measured by Beer-Lambert law.

To conclude the above discussion, for a thin device that is fully depleted, short wavelength photons are absorbed and the photogenerated carriers have a high possibility of extraction by the built-in electric field, giving rise to a peak in the EQE spectrum at short wavelengths. However, long wavelength photons are not absorbed by a thin absorber layer. A thicker PbS layer can absorb more longer wavelength photons but now short wavelength photons are absorbed in the dead zone. Therefore, a thick device has lower quantum efficiency in the short wavelength region causing a red shift of the EQE, as observed in Figure 4.7.

4.3.3 Implication of dead zone

The formation of a dead zone in the device limits the benefit of making the absorber layer thicker to harvest more photons, particularly in the short wavelength region for this bilayer device geometry[23]. The optimum heterojunction device was found to have a PbS thickness of 125 nm, but in this case a significant proportion of long wavelength photons pass right through the device and are not absorbed. Based on the extinction coefficient of PbS QDs, it will require a PbS film at least 2 μm thick to absorb 90% of AM1.5 spectrum[24].

One of the solutions is to introduce an inverted cell structure[25,26], in which the metal oxide layer is fabricated in front of the absorber. This allows the junction interface to be located in the front of the device where light is more intense. However, a dead zone will still be present near the top electrode in such a device, and extraction of charges generated by long wavelength photons will be limited.

An interpenetrated structure is an approach to overcome the dead zone. If the junction interface can be distributed throughout the absorber layer such that charges generated at every point of the absorber layer are close enough to the junction interface, no light will be absorbed in a 'dead zone' from which the charges cannot be extracted. The strategies to create interpenetrated structures will be considered in the next two chapters. However, an optimised morphological design of the interpenetrated structure requires a good understanding of the junctions in the of QD solar cells (and hence what the

thickness of the charge extraction zone is, for example whether its operating mechanism is excitonic or depleted p-n). This is because phase separation of donor-acceptor must be in the same scale of charge collection length[27], which is different for an excitonic and a p-n junction solar cell.

4.4 Operating mechanism of QD heterojunction

4.4.1 Introduction

The operating mechanism of quantum dot heterojunction is an area of debate: whether it is excitonic[11,28,29] or depleted p-n[25,30]. In an excitonic junction, charge separation is achieved by diffusion of bound excitons to a materials' interface to dissociate[31]. An electron is injected into the LUMO of an acceptor leaving a hole in the HOMO of a donor. Choi *et al.*[11] observed a correlation of V_{oc} with LUMO offsets between PbSe QDs and ZnO rather than Fermi-level difference, indicating an excitonic junction behaviour. In support of depleted p-n mechanism, Pattantyus-Abraham *et al.*[25] argue that Förster energy transfer of excitons can only occur over the distance of a few dots based on the transfer time and exciton lifetime of PbS QDs, in contrast to the thickness of the most efficient device, which is around 250 nm, near 100 dot-to-dot transfers.

It is important to understand the device operating mechanism before further structural optimisation. In an excitonic device, device structure must be optimised with donor-acceptor phase separation at the same scale as the exciton diffusion length. In a depleted p-n junction, a built-in electric field extends the

charge collection length further into the material; carriers only need to diffuse into the depletion region to drift to the electrodes[25]. For this reason it is of interest to probe the nature of the operating mechanism of the PbS/ZnO heterojunction. In this study, a transitional behaviour of the junction operating mechanism from excitonic to depleted p-n is observed, following UV doping of ZnO.

4.4.2 Excitonic to p-n junction transition through doping of ZnO

ZnO is inherently an n-type semiconductor but oxygen absorption on the surface can trap electrons. Before UV illumination, ZnO is considered as an instrinsic semiconductor[12]. UV photodoping can raise the doping density of ZnO up to ~10^{19} cm^{-3}. In the study of the junction operating mechanism, the effect of ZnO doping density on the interfacial charge separation mechanism is investigated by employing capacitance - voltage and external quantum efficiency measurements.

First, capacitance - voltage (*C*-*V*) measurements were performed on the devices before and after UV exposure. It is shown in Figure 4.10 that a near-constant capacitance is observed for the device before UV doping. After UV doping the capacitance initially increases and then begins to drop again at some forward bias.

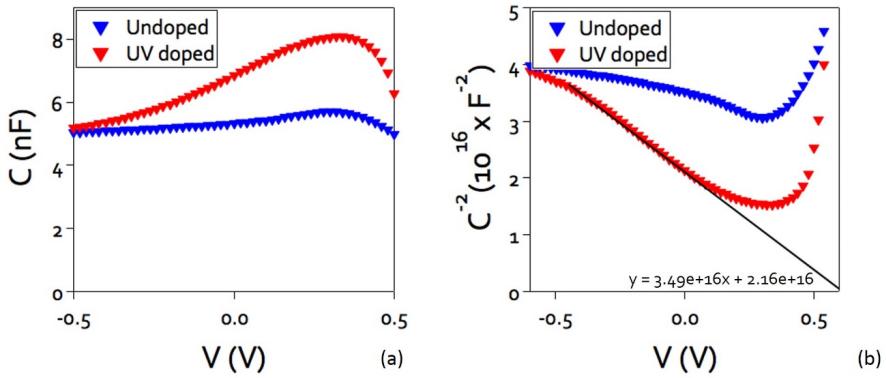

Figure 4.10: Capacitance-voltage measurement of PbS/ZnO heterojunction device before and after UV doping. (a) C-V; (b) C^{-2}-V, the black line shows the linear fitting of equation (4.4).

In a heterojunction, when the acceptor has a doping density much higher than the donor, Mott-Schottky analysis can be applied to determine the doping density of the donor and the built-in potential of a p-n junction[15]. The capacitance is determined by the width of the depletion region and can be expressed as[15,32],

$$\frac{1}{C^2} = \frac{2(V_{bi} - V)}{A^2 q \varepsilon \varepsilon_0 N_a} \tag{4.4}$$

where V_{bi} is the built-in potential, A is the active area (0.02035 cm^2), q is the elementary charge and N_a is the doping density. The bias-dependent capacitance at small forward bias of the UV-treated device is in agreement with equation (4.4) demonstrating a p-n junction behaviour. By fitting the linear region of *C-V* curve, one can calculate the V_{bi} = 0.61 V and N_a = 2.5 × 10^{17} cm^{-3}. The N_a is close to the result obtained from the Schottky junction device (1.4 × 10^{17} cm^{-3}) in Chapter 3. The Mott-Schottky analysis could not be applied to the device before UV doping.

The extracted V_{bi} value, 2.1 V, is not considered valid, as it is much greater than the difference between the VB of PbS (-5.1 eV) and the CB of ZnO (-4.3 eV).

Evidence of the change in charge separation mechanism after UV exposure is also observed in the external quantum efficiency measurement. EQE spectra were recorded as a function of UV exposure time (Figure 4.11). An overall low EQE is observed in the undoped device or with short exposure time with only a peak at 600 nm evident. As UV doping progresses, the spectral response at short wavelength increases with a peak at 450 nm evolving after 3 min. This effect can be explained by the growth of a depletion region within the PbS QDs. As short wavelength photons have short absorption length, the growth of the depletion region improves the collection of charge carriers generated further away from the junction. The overall EQE increase is attributed to the increased electrical conductivity of ZnO.

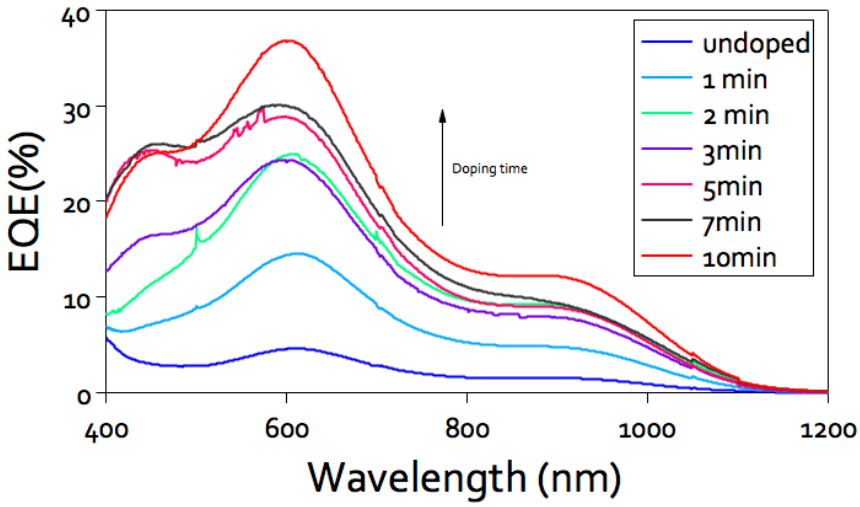

Figure 4.11: Evolution of EQE spectra with UV exposure time.

The growth of a depletion region originates from the change of ZnO doping density. The ZnO nanoparticles are initially intrinsic. Therefore, the depletion region is located mainly within the ZnO layer as the doping density of PbS is much higher. The ZnO does not absorb light at these wavelengths, so there are no excitons generated in this depletion region to be separated. UV-doped ZnO can reach a doping density up to ~10^{19} cm^{-3} [12], two orders of magnitude higher than that of EDT-coupled PbS QDs (~10^{17} cm^{-3}) as calculated in Chapter 3. Most of the depletion region will now be located in the PbS layer where the light absorption occurs. The width of depletion within the PbS layer can be estimated using the discrete boundary approximation[15],

$$w_{PbS} = \frac{1}{N_a}\sqrt{\frac{2\varepsilon\varepsilon_0 V_{bi}}{q(\frac{1}{N_a}+\frac{1}{N_d})}} \quad (4.5)$$

where N_d is the doping density of ZnO. Only the depletion region within the PbS is considered, as ZnO with a large optical band gap of 3.3 eV[33] has little contribution to charge generation. Using equation (4.5), the width of depletion region lying within the PbS layer as a function of ZnO doping density level from 10^{13} to 10^{19} cm^{-3} can be plotted (Figure 4.12).

When initially ZnO is intrinsic the junction shows an excitonic behaviour, as there is no depletion region in the PbS layer: only charge generated within the exciton diffusion length of the junction can be extracted. When ZnO is doped to a level greater than that of PbS, the depletion width in PbS increased. Charge extraction undergoes a p-n junction mechanism such that the built-in electric field can extract charge carriers generated within the depletion region, and in addition some may be extracted from the quasi-neutral region by diffusion.

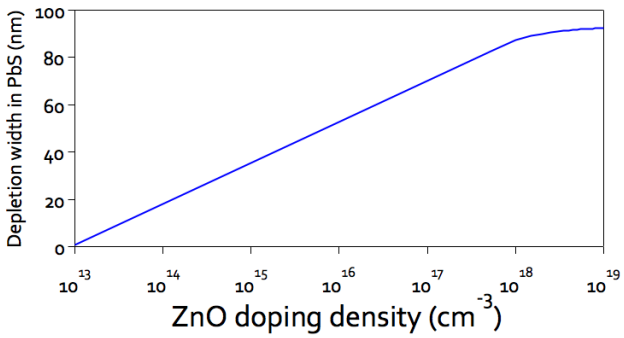

Figure 4.12: Width of depletion region in PbS as a function of ZnO doping density.

To summarise the above findings, the *C-V* measurement of the undoped device shows a near-constant capacitance at reverse bias, indicating that there is no bias-dependent depletion region (excitonic behaviour). The depletion behaviour is observable when ZnO is doped. Furthermore, the EQE shows that increasing the doping density of ZnO results in a greater spectral response from short wavelength region indicating the formation of a depletion region in the PbS, displaying a p-n junction behaviour. The doping density of PbS QDs is influenced by the surface ligands and defect states, which could affect the nature of the heterojunction. QD size could also be an influential factor, as the excitons cannot separate at the interface if the LUMO of PbS lies below that of ZnO.

4.5 Conclusion

The PbS/ZnO heterojunction has significantly improved the photovoltaic performance of PbS QD devices. All working devices had an average efficiency of 2.7±0.36% with a 3% champion device recorded after UV doping of ZnO. However, device performance of the planar junction device geometry is limited due to the formation of a charge extraction dead zone preventing the absorber layer from being made thicker to enhance optical absorption. An interpenetrated structure could enhance both photon absorption and charge extraction, which will be studied in the following chapters. To inform the design of this penetrated structure, a study was made of the operating mechanism of the PbS/ZnO heterojunction, which was not previously well established. A transitional

behaviour from excitonic to depleted p-n junction was observed, which warrants further device optimisation based on both mechanisms.

4.6 References

1. Saito, M.; Fujihara, S. Large Photocurrent Generation in Dye-Sensitized ZnO Solar Cells. *Energy & Environmental Science* **2008**, *1*, 280–283.

2. Grilli, M. L.; Sytchkova, A.; Boycheva, S.; Piegari, A. Transparent and Conductive Al-Doped ZnO Films for Solar Cells Applications. *Physica Status Solidi A* **2013**, *210*, 748–754.

3. Nomura, K.; Ohta, H.; Ueda, K.; Kamiya, T.; Hirano, M.; Hosono, H. Thin-Film Transistor Fabricated in Single-Crystalline Transparent Oxide Semiconductor. *Science* **2003**, *300*, 1269–1272.

4. Sun, B.; Sirringhaus, H. Solution-Processed Zinc Oxide Field-Effect Transistors Based on Self-Assembly of Colloidal Nanorods. *Nano letters* **2005**, *5*, 2408–2413.

5. Bakin, a.; El-Shaer, A.; Mofor, a. C.; Al-Suleiman, M.; Schlenker, E.; Waag, A. ZnMgO-ZnO Quantum Wells Embedded in ZnO Nanopillars: Towards Realisation of Nano-LEDs. *Physica Status Solidi C* **2007**, *4*, 158–161.

6. Leschkies, K. S.; Jacobs, A. G.; Norris, D. J.; Aydil, E. S. Nanowire-Quantum-Dot Solar Cells and the Influence of Nanowire Length on the Charge Collection Efficiency. *Applied Physics Letters* **2009**, *95*, 193103.

7. Law, M.; Greene, L. E.; Johnson, J. C.; Saykally, R.; Yang, P. Nanowire Dye-Sensitized Solar Cells. *Nature Materials* **2005**, *4*, 455–459.

8. Beek, W. J. E.; Wienk, M. M.; Kemerink, M.; Yang, X.; Janssen, R. a J. Hybrid Zinc Oxide Conjugated Polymer Bulk Heterojunction Solar Cells. *Journal of Physical Chemistry B* **2005**, *109*, 9505–9516.

9. Willis, S. M.; Cheng, C.; Assender, H. E.; Watt, A. A. R. The Transitional Heterojunction Behavior of PbS/ZnO Colloidal Quantum Dot Solar Cells. *Nano Letters* **2012**, *12*, 1522–1526.

10. Pacholski, C.; Kornowski, A.; Weller, H. Self-Assembly of ZnO: From Nanodots to Nanorods. *Angewandte Chemie International Edition* **2002**, *41*, 1188–1191.

11. Choi, J. J.; Lim, Y.-F.; Santiago-Berrios, M. B.; Oh, M.; Hyun, B.-R.; Sun, L.; Bartnik, A. C.; Goedhart, A.; Malliaras, G. G.; Abruña, H. D.; *et al.* PbSe Nanocrystal Excitonic Solar Cells. *Nano Letters* **2009**, *9*, 3749–3755.

12. Lakhwani, G.; Roijmans, R. F. H.; Kronemeijer, A. J.; Gilot, J. Probing Charge Carrier Density in a Layer of Photodoped ZnO Nanoparticles by Spectroscopic Ellipsometry. *Journal of Physical Chemistry C* **2010**, *114*, 14804–14810.

13. Verbakel, F.; Meskers, S. C. J.; Janssen, R. A. J. Electronic Memory Effects in Diodes from a Zinc Oxide Nanoparticle-Polystyrene Hybrid Material. *Applied Physics Letters* **2006**, *89*, 102103.

14. Gilot, J.; Wienk, M. M.; Janssen, R. a. J. Double and Triple Junction Polymer Solar Cells Processed from Solution. *Applied Physics Letters* **2007**, *90*, 143512.

15. Nelson, J. *The Physics of Solar Cells*; Imperial College Press: London, 2003.

16. Stallinga, P. *Electrical Characterization of Organic Electronic Materials and Devices*; John Wiley & Sons Ltd: Chichester, 2009.

17. Juška, G.; Viliūnas, M.; Arlauskas, K.; Nekrašas, N.; Wyrsch, N.; Feitknecht, L. Hole Drift Mobility in μc-Si:H. *Journal of Applied Physics* **2001**, *89*, 4971–4973.

18. Tang, J.; Brzozowski, L.; Barkhouse, D. A. R.; Wang, X.; Debnath, R.; Wolowiec, R.; Palmiano, E.; Levina, L.; Pattantyus-Abraham, A. G.; Jamakosmanovic, D.; *et al.* Quantum Dot Photovoltaics in the Extreme Quantum Confinement Regime: The Surface-Chemical Origins of Exceptional Air- and Light-Stability. *ACS Nano* **2010**, *4*, 869–878.

19. Tang, J.; Sargent, E. H. Infrared Colloidal Quantum Dots for Photovoltaics: Fundamentals and Recent Progress. *Advanced Materials* **2010**, *23*, 12–29.

20. Barkhouse, D. A. R.; Kramer, I. J.; Wang, X.; Sargent, E. H. Dead Zones in Colloidal Quantum Dot Photovoltaics: Evidence and Implications. *Optics Express* **2010**, *18*, A451–A457.

21. Law, M.; Beard, M. C.; Choi, S.; Luther, J. M.; Hanna, M. C.; Nozik, A. J. Determining the Internal Quantum Efficiency of PbSe Nanocrystal Solar Cells with the Aid of an Optical Model. *Nano Letters* **2008**, *8*, 3904–3910.

22. Willis, S. M. Advanced Optoelectronic Characterisation of Solar Cells, University of Oxford, 2011.

23. Kramer, I. J.; Sargent, E. H. Colloidal Quantum Dot Photovoltaics: a Path Forward. *ACS Nano* **2011**, *5*, 8506–8514.

24. Wu, H.; Yang, Y.; Oh, E.; Lai, F.; Yu, D. Direct Synthesis of High-Density Lead Sulfide Nanowires on Metal Thin Films Towards Efficient Infrared Light Conversion. *Nanotechnology* **2012**, *23*, 265602.

25. Pattantyus-Abraham, A. G.; Kramer, I. J.; Barkhouse, A. R.; Wang, X.; Konstantatos, G.; Debnath, R.; Levina, L.; Raabe, I.; Nazeeruddin, M. K.; Grätzel, M.; *et al.* Depleted-Heterojunction Colloidal Quantum Dot Solar Cells. *ACS Nano* **2010**, *4*, 3374–3380.

26. Luther, J. M.; Gao, J.; Lloyd, M. T.; Semonin, O. E.; Beard, M. C.; Nozik, A. J. Stability Assessment on a 3% Bilayer PbS/ZnO Quantum Dot Heterojunction Solar Cell. *Advanced Materials* **2010**, *22*, 3704–3707.

27. McNeill, C. R.; Westenhoff, S.; Groves, C.; Friend, R. H.; Greenham, N. C. Influence of Nanoscale Phase Separation on the Charge Generation Dynamics and Photovoltaic Performance of Conjugated Polymer Blends: Balancing Charge Generation and Separation. *Journal of Physical Chemistry C* **2007**, *111*, 19153–19160.

28. Leschkies, K. S.; Beatty, T. J.; Kang, M. S.; Norris, D. J.; Aydil, E. S. Solar Cells Based on Junctions Between Colloidal PbSe Nanocrystals and Thin ZnO Films. *ACS Nano* **2009**, *3*, 3638–3648.

29. Choi, J. J.; Luria, J.; Hyun, B.-R.; Bartnik, A. C.; Sun, L.; Lim, Y.-F.; Marohn, J. a; Wise, F. W.; Hanrath, T. Photogenerated Exciton Dissociation in Highly Coupled Lead Salt Nanocrystal Assemblies. *Nano Letters* **2010**, *10*, 1805–1811.

30. Strasfeld, D. B.; Dorn, A.; Wanger, D. D.; Bawendi, M. G. Imaging Schottky Barriers and Ohmic Contacts in PbS Quantum Dot Devices. *Nano Letters* **2012**, *12*, 569.

31. Gregg, B. A. Excitonic Solar Cells. *Journal of Physical Chemistry B* **2003**, *107*, 4688–4698.

32. Clifford, J. P.; Johnston, K. W.; Levina, L.; Sargent, E. H. Schottky Barriers to Colloidal Quantum Dot Films. *Applied Physics Letters* **2007**, *91*, 253117.

33. Srikant, V.; Clarke, D. R. On the Optical Band Gap of Zinc Oxide. *Journal of Applied Physics* **1998**, *83*, 5447–5451.

Chapter 5 - PbS/ZnO Bulk Heterojunction

5.1 Introduction

Chapter 4 shows that a charge extraction dead zone exists in a planar junction device, limiting the effective thickness of devices. In this chapter, an interpenetrated donor-acceptor network using a PbS/ZnO QD blend was created to extend the heterojunction interface throughout the active layer. The blend morphology incorporates a large interface area and short exciton diffusion distance such that excitons can easily diffuse into the junction interface for dissociation[1,2]. A bulk heterojunction would therefore allow more light to be absorbed and more photocurrent to be extracted, as the device thickness is no longer limited by the depletion width of the bi-layer junction. During the same period this research was carried, a QD BHJ using PbS/Bi_2S_3 nanocrystal blend was reported by Arup *et al.*[3], showing an enhanced efficiency from 2% to 5% as result of extended carrier lifetime due to fast exciton dissociation. This is the only nanocrystal blend method to create QD BHJ reported to date. Most reports on QD BHJ requires fabricating a nanostructured template[4–6] which is subsequently in-filled with QDs.

The key aspects discussed in this study are: 1) whether using a BHJ can enhance performance; 2) the morphology of PbS/ZnO blend; 3) the charge transfer process within the BHJ.

5.2 Experimental methods

1.4 eV PbS QDs and ZnO nanoparticles are synthesised as described previously. To fabricate BHJ devices, both solutions were mixed according to ZnO weight percentages and stirred overnight in a glovebox. Devices were fabricated using sequential spin coating of the BHJ solution as described in Chapter 3. Atomic force microscope images were taken using an AutoProbe CP (Park Scientific Instruments) in tapping mode. Photoluminescence spectra were recorded on a Princeton Instruments Acton SP2300 detector cooled by liquid N_2. The sample was excited by a 633 nm HeNe laser at a 45° incident angle.

5.3 Results and discussions

5.3.1 Device performance

A schematic of the BHJ device structure is shown in Figure 5.1(a). The relative concentration of donor and acceptor materials considerably affects the bulk morphology and therefore the device performance[7]. It is postulated that if the device is excitonic, an ideal morphology of a binary QD blend should have a scale of phase separation within the exciton diffusion length while ensuring that both phases can percolate to form transport pathways[8,9]. A low ZnO concentration would result in small islands of ZnO in a large PbS matrix, and

poor percolation. On the other hand, when ZnO concentration is too high, PbS "islands" will form, where free holes can be trapped. It is at intermediate ZnO wt% concentrations that it is hoped that a bi-continuous phase structure will be formed, and if the two components are not agglomerated, this phase structure will be on a fine scale[10]. Figure 5.1(b) shows the *J-V* characteristic curves of the BHJ devices with different ZnO concentrations. To ensure the charge extraction in the bulk is excitonic, no UV photodoping was performed prior to *J-V* measurement. It was found that UV doping of the BHJ caused short circuit in the device due to increased conductivity of ZnO, leading to current leakage. The extracted solar cell parameters of the BHJ devices and a reference planar junction device (0 wt%) are shown in Figure 5.1(c)(d). The mean device parameters (J_{sc}, *FF*, V_{oc}) of the 20 wt% ZnO device are higher than the other weight percentages and hence leading to a higher average device efficiency. This composition dependence suggests the performance of the BHJ could be morphology-related in the manner described above. Interestingly, the V_{oc} of the 20 wt% BHJ is higher than the PbS-only (bilayer) device, reaching 0.4 V, though the J_{sc} and *FF* are lower. A high concentration of ZnO shows a drastic decrease in performance with the 50 wt% device having poor rectification with the *J-V* curve showing almost a straight line. A crossover effect of the *J-V* curves is observed at 0.5 V, indicating that a secondary junction exists in the device. This is likely due to a Schottky barrier present between the ZnO in the BHJ and the PEDOT:PSS[11,12] which is more likely to occur at this high ZnO concentration.

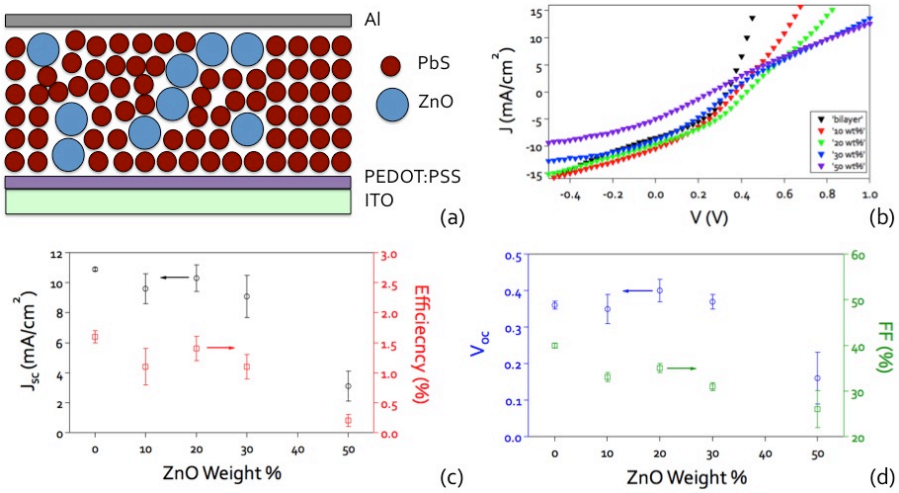

Figure 5.1: (a) Device schematic of a PbS/ZnO BHJ; (b) J-V characteristic curves of the BHJ devices with different ZnO concentration; (v) comparison of J_{sc} and PCE at different ZnO concentrations; (d) comparison of V_{oc} and FF at different ZnO concentrations.

To eliminate the barrier at the ZnO/PEDOT:PSS interface and reduce recombination at the electrodes[13], a thin pristine layer of PbS acting as hole transporting/electron blocking layer and a layer of neat ZnO as electron transporting/hole blocking layer were employed to sandwich the BHJ such that the contact of ZnO with PEDOT and PbS with Al (Figure 5.2(a)) can be isolated. Figure 5.2(b) shows the *J-V* characteristic curve of a 20 wt% BHJ device with the capping layers. The *J-V* curve of a PbS/ZnO bilayer device with the same absorber layer thickness is shown for comparison. An increase in V_{oc} from 0.40 V to 0.59 V was observed by using capping layers with the *FF* increased from 35% to 46%, leading to an increase in overall efficiency reaching 1.8%. The V_{oc} of the BHJ devices exceeds that of the simple bilayer heterojunction by more than 0.1 V.

This increase is possibly driven by efficient exciton dissociation at the PbS/ZnO interface. Photovoltage created by an excitonic process is usually higher as it overcomes the limit of V_{bi} from the band bending of a p-n junction[14]. The overall device efficiency is, however, significantly lower than the reference bilayer device.

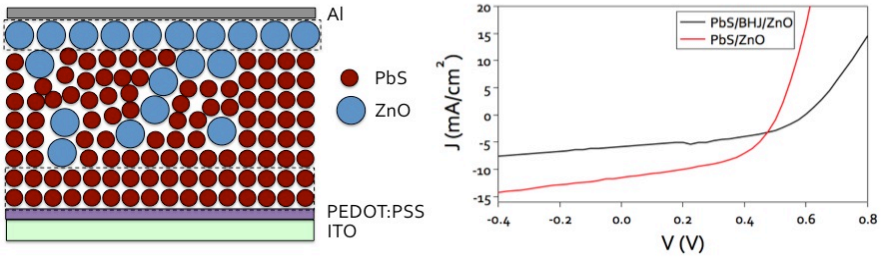

Figure 5.2: (a) Schematic of using capping layers between the BHJ and the electrodes; (b) comparison of J-V characteristic curves of devices with and without capping ayers.

5.3.2 Spectral response measurement

Photocurrent spectral response measurement was employed to probe whether the BHJ can extract charges generated in a dead zone. To rule out any perturbation from the depletion region at PbS/Al interface, devices that are thicker than the depletion width (80 nm as calculated in Chapter 3) were made such that a field-free region will form at the front, where short wavelength photons are mostly absorbed. In a planar junction device, the EQE intensity at short wavelength will generally decrease with increasing device thickness, as charge excitation by short wavelengths is moving away from the junction and eventually in the dead zone. This is seen in Figure 5.3(a) that a decreased EQE

intensity at 400 nm is observed for the Schottky junction device. The EQE spectra of the BHJ devices show different patterns of change when the device thickness increases (Figure 5.3(b)). The 120 nm device shows a higher EQE at 400 nm wavelength than that of the 90 nm device, suggesting charges are extracted from the electric field-free region in the BHJ. With the thickness increasing from 90 to 120 nm more photons are absorbed. However, the EQE of the 180 nm device drops to the same level as the 90 nm device. Therefore, further increasing the thickness of the BHJ does not contribute to more photocurrent generation from the dead zone. At the same time, the EQE decreases at wavelength above 500 nm for the two thicker devices, leading to overall decrease in efficiency. Therefore, the benefit of having two junctions in the BHJ devices is undermined possibly by poor morphology of the BHJ film, leading to poor charge extraction, or interface recombination that results in drastic decline in efficiency. Therefore, the study now turns to examine the morphology and electronic properties of the BHJ and understand their implication on further device optimisation.

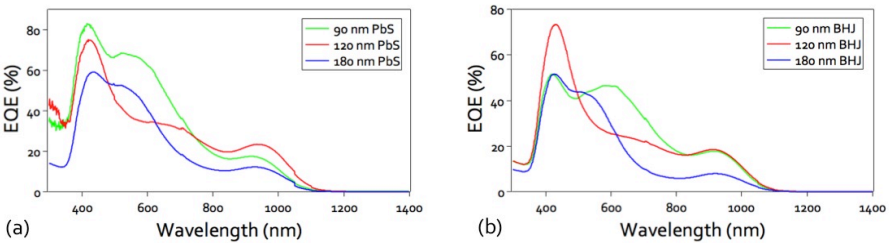

Figure 5.3: Thickness dependent EQE spectra: (a) PbS only devices; (b) BHJ devices.

5.3.3 Analysis of QD BHJ

5.3.3.1 Morphology study of PbS/ZnO BHJ

The surface morphology of the BHJ film was examined with an atomic force microscope (AFM) as shown in Figure 5.4. The AFM images were taken by Dr Peter Kovacik at the Department of Materials, University of Oxford. The neat PbS QD film shows a very smooth surface. Surface agglomerates (bright spots) start to appear on the surface of the 10 wt% ZnO film. The agglomeration becomes more pronounced at the surface of the BHJ layer, with the 20 wt% and 50 wt% film showing very coarse surfaces. Base on the change in weight concentration, these agglomerates should be predominately ZnO. The root mean square (RMS) roughness of the 20 wt% layer is 3.25 nm, similar to that of the 50 wt% surface (3.49 nm). This is significantly higher than the RMS roughness of the 10 wt% surface at 1.48 nm. Only the 20 wt% film shows clearly two separated phases with the PbS domain size in the range of 20 - 50 nm. This could explain why the 20 wt% devices produced the highest efficiency for the BHJ. The 50 wt% shows that ZnO agglomerates are dominating the morphology which creates shunt paths in the device.

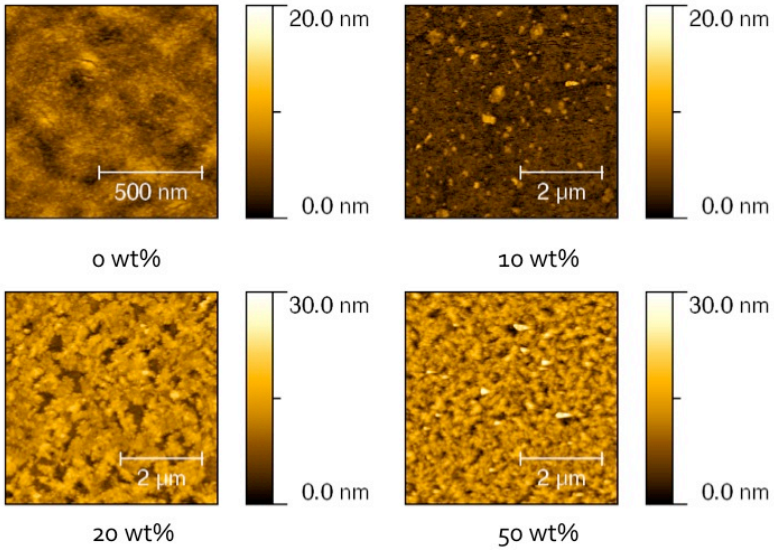

Figure 5.4: AFM surface morphology of BHJ film as a function of ZnO composition.

However, examining the PbS/ZnO blend dispersion cast directly onto a grid from solution under a TEM (Figure 5.5) does not show aggregation of ZnO nanocrystals. Individual ZnO nanocrystals with sizes around 5 - 10 nm are scattered in the PbS matrix. Therefore, the aggregation of ZnO nanocrystals is likely to have formed during the film deposition stage. A previous study has observed a similar coarse surface morphology on a conjugated polymer/ZnO composite film[15]. The study shows that surface coarsening is due to ZnO aggregation and that using amines can improve the colloidal stability of ZnO in the blend but does not reduce the extent of ZnO aggregation in the film due to incompatibility between the ZnO surface and the conjugated polymers. In the current system, the PbS QDs are coated with oleic acid molecules and expected to have a similar hydrophobicity as the conjugated polymer chains. This

uncontrolled agglomeration of ZnO leads to poor phase separation that is detrimental to charge transfer. In another study, Oosterhout *et al*.[16] studied the three-dimensional phase morphology of a P3HT/ZnO blend. They believe that the low efficiency of these devices using ZnO as electron acceptor comparing with using PCBM is mainly due to coarse phase separation.

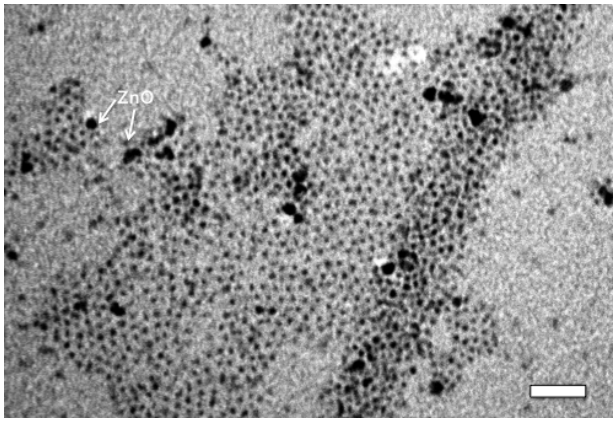

Figure 5.5: TEM micrograph of PbS-ZnO BHJ solution. Scale bar = 30 nm.

5.3.3.2 Charge transfer from PbS to ZnO

The BHJ would have two possible routes (a depleted junction and an excitonic junction) for charge separation. First, a depleted junction is established (illustrated in Figure 5.6(b) as the process (1)). In this process, free electrons and holes are generated under the influence of the depletion region's electric field. A recent study has suggested that this is by dissociation of excitons through tunnelling between highly-coupled dots[17]. Charge extraction is achieved by the built-in field drifting the holes to the ITO and electrons to the Al. In the excitonic process (process (2) in Figure 5.6(b)), the intermixing of PbS and ZnO facilitates

fast exciton dissociation at the interface. In principle, the BHJ has two junctions operating in parallel such that charges generated beyond the depletion region can be extracted through an excitonic process.

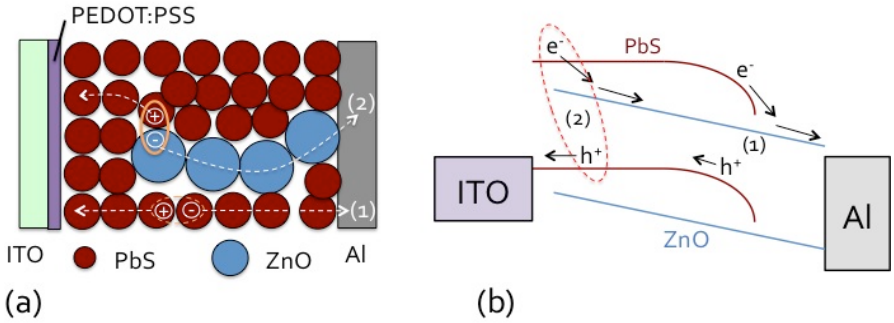

Figure 5.6: The proposed device operating mechanism that involves in two charge separation processes: exciton dissociation at PbS-ZnO interface and free electrons and holes drift by the built-in field.

To understand the exciton dissociation process, photoluminescence was measured to study the charge transfer at the type-II heterojunction. Figure 5.7(a) shows the photoluminescence spectra of the EDT-capped PbS and OA-capped PbS QD film. The emission peak at around 1100 nm can be attributed to the band-edge transition in PbS QDs. The PL of EDT-coupled QD film shows a lower intensity than the OA-capped QD film, suggesting the emission is quenched by the charge transfer between electronically coupled-QDs[18], which becomes more favourable with the shorter EDT ligands. With increasing ZnO concentration, there is a small increase in the emission from PbS band-edge transition, as shown in Figure 5.7(b), and the increase in the emission becomes more pronounced beyond 20 wt% with a small red-shift in the spectra. The red-shift in the emission

is an indication of radiative recombination of intermolecular charge-transfer (CT) states at the PbS/ZnO interface, suggesting geminate recombination of coulombically bound electron-hole pairs[19]. Therefore, on inclusion of ZnO, inter-dot exciton dissociation (process (1)) is overtaken by the energy transfer from PbS to ZnO (process (2)), resulting in CT states, which could recombine radiatively.

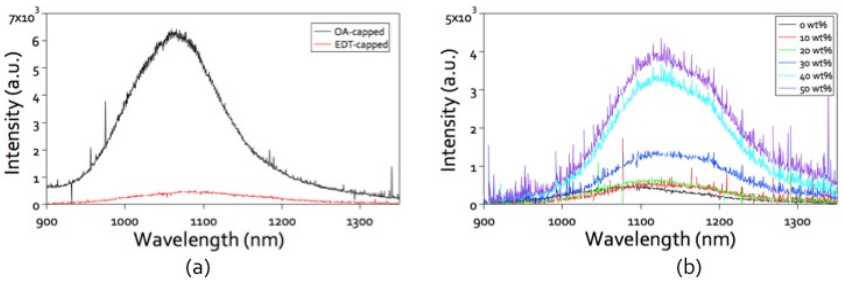

Figure 5.7: (a) Photoluminescent spectra of OA-capped and EDT-capped PbS thin film; (a) PL spectra of BHJ film at different ZnO concentrations.

A recent study suggests that CT states are responsible for the low performance of QD sensitised or hybrid photovoltaic devices[20]. A CT state consists of a localised charge in the HOMO of PbS and an electron in the LUMO of ZnO. This geminate electron-hole pair is tightly bound by coulombic interaction, requiring extra energy to separate. Geminate recombination could also occur in exciton transfer in coupled-QDs, however, is less likely as the recombination energy is competing with the built-in electric field[18,21].

This above discussion suggests that charge separation via exciton dissociation between PbS and ZnO is less efficient due to interfacial recombination. This can

be enhanced by using a p-n junction route such that the transport of charges is assisted by a built-in field, which is sufficient to produce a large photocurrent with minimum interface recombination. PbS QD devices using p-n or Schottky junction has achieved over 7% power conversion efficiency[22] while PbS QD-sensitised[23] and hybrid[24] devices have efficiency lower than 1%.

With an understanding of the operating principle, it is possible to rationalise the design principle of an interpenetrated network for quantum dot heterojunction. It is essential to engineer the bulk morphology to achieve a phase separation such that the QD phase is fully depleted to sustain an electric field. This could improve charge separation by increasing the interfacial area, and the depth into the sample at which interface is present, while minimising the interfacial geminate recombination. In the next chapter, an approach is proposed to engineer the donor-acceptor morphology to achieve efficient charge separation in QD BHJ devices.

5.4 Conclusion

This chapter explores a novel concept of an all inorganic quantum dot bulk heterojunction solar cell structure using PbS and ZnO nanocrystals. The devices show no improvement in device performance compared with ordinary planar junction devices. At this stage, controlling the morphology of the binary nanocrystal blend has not been studied. Simple blending of these two particles leads to a coarse surface, which is detrimental to the electronic properties. How

to achieve a bi-continuous morphology could be further examined by selecting capping ligands or fine-tuning the acceptor concentration. The poor performance is also a result of the generation of localised geminate pairs that promote interface recombination. The study leads us to consider more sophisticated means to control the morphology of quantum bulk heterojunction.

5.5 References

1. Yu, G.; Gao, J.; Hummelen, J. C.; Wudl, F.; Heeger, A. J. Polymer Photovoltaic Cells: Enhanced Efficiencies via a Network of Internal Donor-Acceptor Heterojunctions. *Science* **1995**, *270*, 1789–1791.

2. Park, S. H.; Anshuman, R.; Beaupré, S.; Cho, S.; Coates, N.; Moon, J. S.; Moses, D.; Leclerc, M.; Lee, K.; Heeger, A. J. Bulk Heterojunction Solar Cells with Internal Quantum Efficiency Approaching 100%. *Nature Photonics* **2009**, *3*, 297–303.

3. Rath, A. K.; Bernechea, M.; Martinez, L.; Arquer, F. P. G. De; Osmond, J.; Konstantatos, G. Solution-Processed Inorganic Bulk Nano-Heterojunctions and Their Application to Solar Cells. *Nature Photonics* **2012**, *6*, 529–534.

4. Barkhouse, D. A. R.; Debnath, R.; Kramer, I. J.; Zhitomirsky, D.; Pattantyus-Abraham, A. G.; Levina, L.; Etgar, L.; Grätzel, M.; Sargent, E. H. Depleted Bulk Heterojunction Colloidal Quantum Dot Photovoltaics. *Advanced Materials* **2011**, *23*, 3134–3138.

5. Kramer, I. J.; Zhitomirsky, D.; Bass, J. D.; Rice, P. M.; Topuria, T.; Krupp, L.; Thon, S. M.; Ip, A. H.; Debnath, R.; Kim, H.-C.; *et al.* Ordered Nanopillar Structured Electrodes for Depleted Bulk Heterojunction Colloidal Quantum Dot Solar Cells. *Advanced Materials* **2012**, *24*, 2315–2319.

6. Leschkies, K. S.; Jacobs, A. G.; Norris, D. J.; Aydil, E. S. Nanowire-Quantum-Dot Solar Cells and the Influence of Nanowire Length on the Charge Collection Efficiency. *Applied Physics Letters* **2009**, *95*, 193103.

7. Bavel, S. S. van; Bärenklau, M.; With, G. de; Hoppe, H.; Loos, J. P3HT/PCBM Bulk Heterojunction Solar Cells: Impact of Blend Composition and 3D Morphology on Device Performance. *Advanced Functional Materials* **2010**, *20*, 1458–1463.

8. Dennler, G.; Scharber, M. C.; Brabec, C. J. Polymer-Fullerene Bulk-Heterojunction Solar Cells. *Advanced Materials* **2009**, *21*, 1323–1338.

9. Bartelt, J. A.; Beiley, Z. M.; Hoke, E. T.; Mateker, W. R.; Douglas, J. D.; Collins, B. A.; Tumbleston, J. R.; Graham, K. R.; Amassian, A.; Ade, H.; *et al.* The Importance of Fullerene Percolation in the Mixed Regions of Polymer-Fullerene Bulk Heterojunction Solar Cells. *Advanced Energy Materials* **2013**, *3*, 364–374.

10. Dang, M. T.; Hirsch, L.; Wantz, G.; Wuest, J. D. Controlling the Morphology and Performance of Bulk Heterojunctions in Solar Cells. Lessons Learned from the Benchmark System. **2013**.

11. Nakano, M.; Tsukazaki, a.; Gunji, R. Y.; Ueno, K.; Ohtomo, a.; Fukumura, T.; Kawasaki, M. Schottky Contact on a ZnO (0001) Single Crystal with Conducting Polymer. *Applied Physics Letters* **2007**, *91*, 142113.

12. Lakhwani, G.; Roijmans, R. F. H.; Kronemeijer, A. J.; Gilot, J. Probing Charge Carrier Density in a Layer of Photodoped ZnO Nanoparticles by Spectroscopic Ellipsometry. *Journal of Physical Chemistry C* **2010**, *114*, 14804–14810.

13. Leschkies, K. S.; Beatty, T. J.; Kang, M. S.; Norris, D. J.; Aydil, E. S. Solar Cells Based on Junctions Between Colloidal PbSe Nanocrystals and Thin ZnO Films. *ACS Nano* **2009**, *3*, 3638–3648.

14. Gregg, B. A. Excitonic Solar Cells. *Journal of Physical Chemistry B* **2003**, *107*, 4688–4698.

15. Rhodes, R.; Horie, M.; Chen, H.; Wang, Z.; Turner, M. L.; Saunders, B. R. Aggregation of Zinc Oxide Nanoparticles: From Non-Aqueous Dispersions to Composites Used as Photoactive Layers in Hybrid Solar Cells. *Journal of Colloid and Interface Science* **2010**, *344*, 261–271.

16. Oosterhout, S. D.; Wienk, M. M.; Bavel, S. S. van; Thiedmann, R.; Koster, L. J. A.; Gilot, J.; Loos, J.; Schmidt, V.; Janssen, R. a J. The Effect of Three-Dimensional Morphology on the Efficiency of Hybrid Polymer Solar Cells. *Nature Materials* **2009**, *8*, 818–24.

17. Choi, J. J.; Luria, J.; Hyun, B.-R.; Bartnik, A. C.; Sun, L.; Lim, Y.-F.; Marohn, J. a; Wise, F. W.; Hanrath, T. Photogenerated Exciton Dissociation in Highly Coupled Lead Salt Nanocrystal Assemblies. *Nano Letters* **2010**, *10*, 1805–1811.

18. Gao, J.; Johnson, J. C. Charge Trapping in Bright and Dark States of Coupled PbS Quantum Dot Films. *ACS Nano* **2012**, *6*, 3292–3303.

19. Tvingstedt, K.; Vandewal, K.; Zhang, F.; Inganäs, O. On the Dissociation Efficiency of Charge Transfer Excitons and Frenkel Excitons in Organic Solar Cells: A Luminescence Quenching Study. *Journal of Physical Chemistry C* **2010**, *114*, 21824–21832.

20. Cate, S. ten; Schins, J. M.; Siebbeles, L. D. A. Origin of Low Sensitizing Efficiency of Quantum Dots in Organic Solar Cells. *ACS Nano* **2012**, *6*, 8983–8988.

21. Nagpal, P.; Klimov, V. I. Role of Mid-Gap States in Charge Transport and Photoconductivity in Semiconductor Nanocrystal Films. *Nature Communications* **2011**, *2*.

22. Ip, A. H.; Thon, S. M.; Hoogland, S.; Voznyy, O.; Zhitomirsky, D.; Debnath, R.; Levina, L.; Rollny, L. R.; Carey, G. H.; Fischer, A.; *et al.* Hybrid Passivated Colloidal Quantum Dot Solids. *Nature Nanotechnology* **2012**, *7*, 577–582.

23. Lee, H.; Leventis, H. C.; Moon, S.-J.; Chen, P.; Ito, S.; Haque, S. a.; Torres, T.; Nüesch, F.; Geiger, T.; Zakeeruddin, S. M.; *et al.* PbS and CdS Quantum Dot-Sensitized Solid-State Solar Cells: "Old Concepts, New Results."*Advanced Functional Materials* **2009**, *19*, 2735–2742.

24. Watt, A. A. R.; Blake, D.; Warner, J. H.; Thomsen, E. A.; Tavenner, E. L.; Rubinsztein-Dunlop, H.; Meredith, P. Lead Sulfide Nanocrystal: Conducting Polymer Solar Cells. *Journal of Physics D: Applied Physics* **2005**, *38*, 2006–2012.

Chapter 6 - Templated TiO_2/PbS Bulk Heterojunction

6.1 Introduction

In this chapter, a strategy to engineer the QD BHJ morphology is employed to achieve enhanced light absorption and efficient charge separation. This is realised by patterning the n-type semiconductor (TiO_2) into a porous structure, which can be in-filled by PbS QDs such that the domain size of PbS can be controlled. It is widely accepted that the charge separation mechanism at the PbS/TiO_2 interface is depleted p-n[1–3]. Therefore, the domain size of PbS should favour the formation of an electric field within the pores to achieve charge separation over a larger volume of material than a simple bilayer structure. There have been some reports on fabricating nanostructured metal oxide templates using nano-lithography[4] or other solution-grown techniques[5–7]. However, these methods require either expensive equipment or extra fabrication steps, which undermine the advantage of using solution-processed PbS QDs for low-cost photovoltaics. In this study, the porous TiO_2 with controlled pore dimension is created using a straightforward sacrificial lithography method using polystyrene (PS) spheres.

The main questions to address in this chapter are: 1) What is the ideal pore size that facilitates both light absorption and charge extraction? 2) Can QDs infiltrate

the pores without changing the deposition method? 3) Can such a structure improve the device performance?

6.2 Fabrication of templated TiO_2/PbS devices

6.2.1 Methods

A schematic of the fabrication process is shown in Figure 6.1. TiO_2 substrates were prepared by Dr Michael Lee from the Department of Physics, University of Oxford. Fluorine-doped tin oxide-coated glass (Pilkington TEC 15) was rinsed with milliQ water, acetone and ethanol and dried with clean dry air. The substrates were treated by oxygen plasma for 5 min. A compact layer of TiO_2 was fabricated to isolate the contact between the PbS and FTO. The compact layer of anatase TiO_2 was formed through spray pyrolysis of titanium diisopropoxide bis(acetylacetonate) (Sigma-Aldrich) diluted in anhydrous ethanol at a volumetric ratio of 1:10 using nitrogen as carrier gas. For a planar junction device, a flat TiO_2 layer was deposited by spin coating TiO_2 paste (Dyesol 18NR-T) diluted in anhydrous ethanol at 1:4 by weight at 2000 rpm. For a porous TiO_2 film, the same concentration of TiO_2 paste was mixed with polystyrene spheres (Thermo Scientific, 300 nm) at 1:4 PS:ethanol concentration and spin coated on at 2000 rpm. The TEM image of the polystyrene beads was shown in Figure 6.1. The layers were then sintered in air at 550°C for 30 min. The flat TiO_2 film is nearly visually transparent, while the macroporous TiO_2 film is translucent containing sub-micron voids acting as light scattering centres (Figure 6.2).

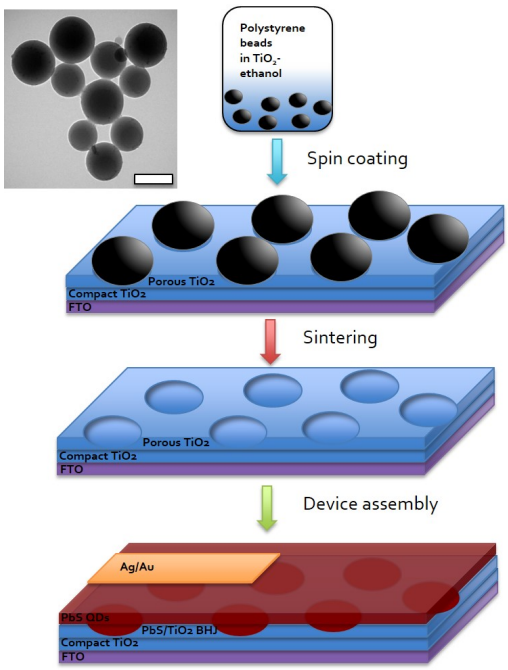

Figure 6.1 TEM micrograph of polystyrene spheres (300 nm) and a schematic describing the process of fabricating a templated porous TiO_2 film and device assembly.

1.4 eV PbS QDs were synthesised as in Chapter 3. Fabrication of solar cell devices was performed under ambient conditions. PbS QD layers were fabricated by a layer-by-layer spin coating technique. On a constantly spinning substrate, 1 drop of 37.5 mg/mL PbS was dispensed through a 0.2 μm PTFE membrane filter, followed by 2 drops of 10% 3-mercaptopropionic acid (MPA) in methanol through a 0.45 μm PTFE filter. The film was washed with 5 drops of methanol, 5 drops of toluene and washed again with 5 drops of methanol. The above cycle was repeated to attain required thicknesses. It is found that the most efficient device consists of 12 layers PbS. A high work function metal or semiconductor (Au, Pt, MoO_x) is required for top contact to form an Ohmic junction between the

PbS and the cathode[8]. Top electrodes containing 20 nm Au followed by 80 nm Ag were deposited in an Edwards Auto thermal evaporator at 10^{-6} Torr at the rate of 1 Å/s.

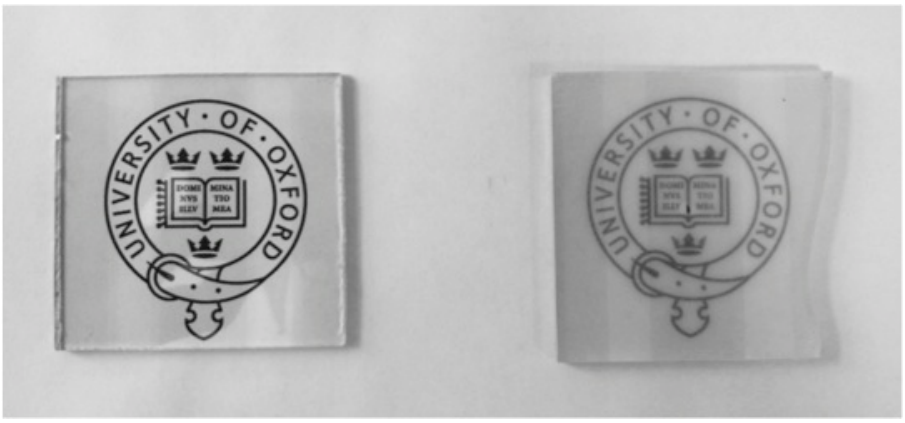

Figure 6.2: (Left) flat TiO_2 film on an FTO substrate; (Right) macroporous TiO_2 film.

6.2.2 Determination of pore sizes and morphological characterisation

The optimum pore size and layer thickness of the porous TiO_2 needs to be determined, with consideration of the device properties of light absorption (volume fraction of PbS QDs, layer thickness), charge extraction (size of PbS domain) and processing limitations (pore infiltration). First, the maximum radius of the pores should be considered in conjunction with the width of depletion within the PbS, where collection of photogenerated carriers is most efficient. To estimate the depletion length in PbS at a PbS/TiO_2 junction, capacitance-voltage measurement on a PbS/TiO_2 bilayer device was performed and the Mott-Schottky plot is shown in Figure 6.3. A bias-dependent capacitance at reverse bias is observed indicating the PbS layer is not fully depleted at equilibrium. This

confirms that the PbS/TiO_2 barrier operates as a p-n junction as expected[9]. The linear region at small forward bias can be fitted with depletion capacitance equation as,

$$\frac{1}{C^2} = \frac{2(V_{bi} - V)}{A^2 q \varepsilon \varepsilon_0 N_a} \quad (6.1)$$

It is assumed that almost all the depletion region occurs within the PbS as TiO_2 is usually more heavily doped[10,11] reaching a doping density up to 10^{20} cm^{-3}. V_{bi} = 0.65 V and N_a = 5.6×10^{16} cm^{-3} are extrapolated from the linear region. The width of the depletion region can be calculated by,

$$w = \sqrt{\frac{2\varepsilon\varepsilon_0 V_{bi}}{qN_a}}. \quad (6.2)$$

The depletion width at equilibrium is measured to be ~150 nm. Therefore, a pore size of 300 nm is desired as it maximises the PbS volume fraction within the TiO_2, while allowing for a fully depleted PbS region within the pores.

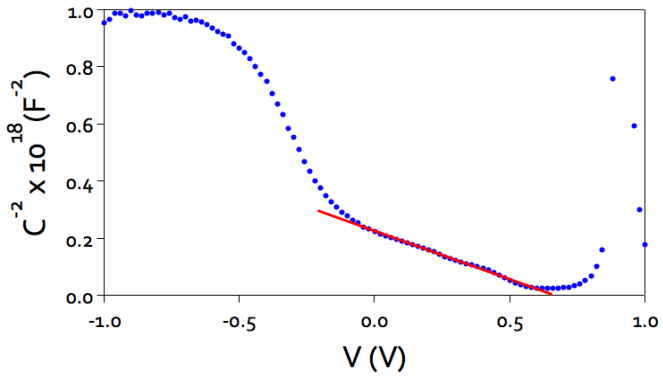

Figure 6.3: Mott-Schottky plot of a PbS/TiO_2 planar junction device.

To have successful pore infiltration by QDs, one must ensure that all pores are open, as closed pores embedded within the TiO_2 would not be filled during the spin-coating process (Figure 6.4). One way to ensure this is to make the TiO_2 layer around 300 nm thick to create a monolayer of pores such that no voids are formed after PbS deposition.

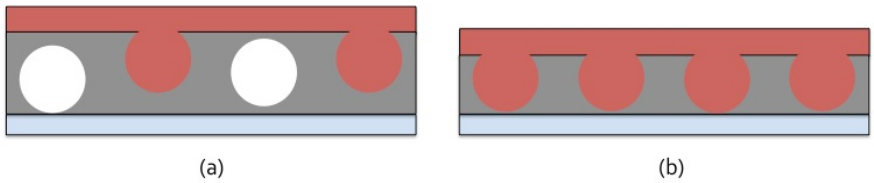

Figure 6.4: (a) Voids are formed when closed-pores are in the layer; (b) by making the TiO_2 layer sufficiently thin, a monolayer of pores with surface openings can be formed to allow QDs pass into the pores.

The porous morphology was studied on a Zeiss NVision 40 focused-ion beam (FIB) scanning electron microscope operated at 2 kV. The images were taken by Dr Gareth Hughes at the Department of Materials, University of Oxford. The FIB was used to prepare cross-sections of the films. Figure 6.5(a) shows a highly porous structured TiO_2 with pore size roughly mimicking the dimension of polystyrene spheres. Some large pores can be seen, possibly due to agglomeration of the polystyrene spheres. Spin coating of QDs onto the porous TiO_2 shows good infiltration into the porous structure with no voids formed (Figure 6.5(b)). Back-scattered electron imaging allowed contrast between the PbS and TiO_2 phases. The domain size of PbS is shown to be around 300 nm, as expected. Figure 6.5(c) shows the cross-section of a planar junction device.

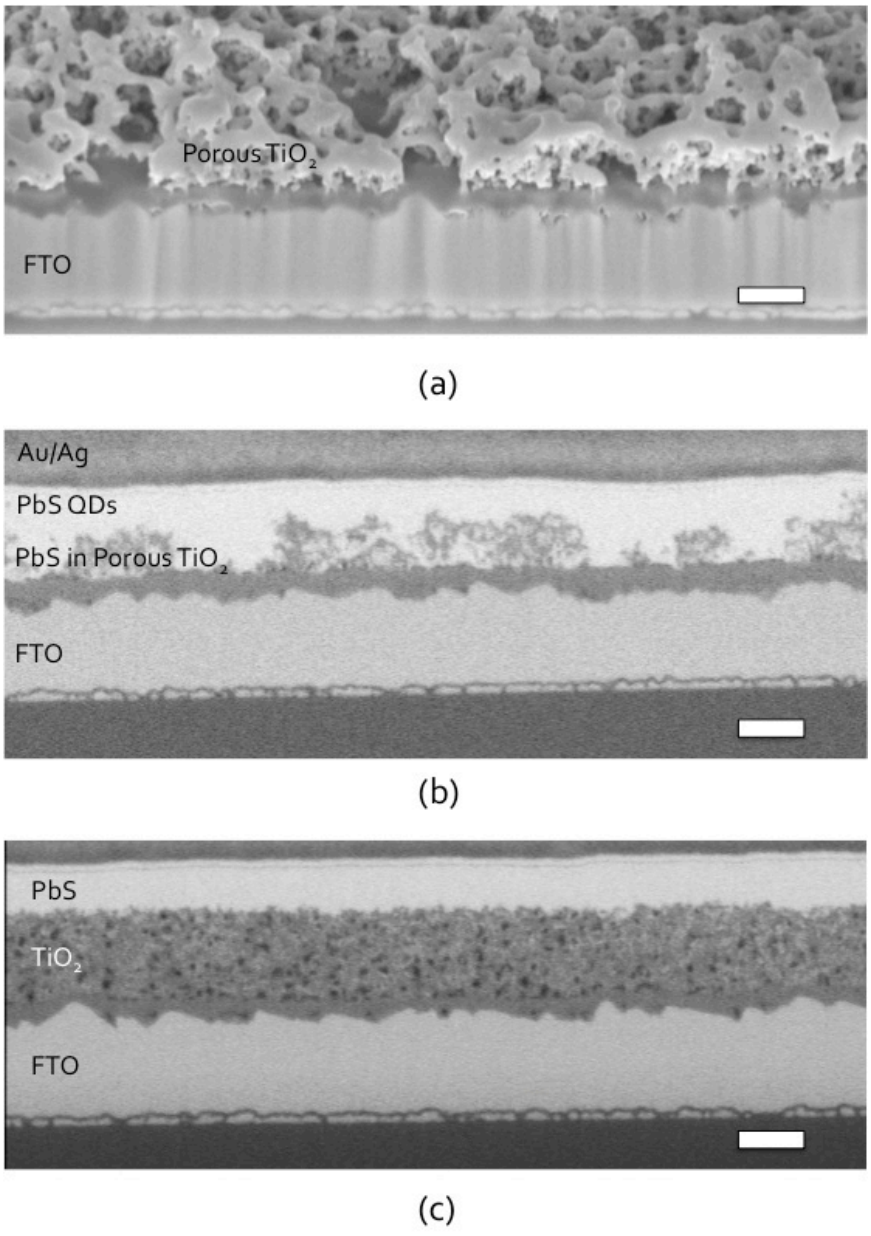

Figure 6.5: Scanning electron microscopy images of (a) porous TiO_2 cross-section and surface; (b) secondary electron detector image of device cross-section of QD-filled porous TiO_2 film; (c) secondary electron detector image of a cross-section through a planar device. Scale bar = 300 nm.

6.3 Device characterisation

6.3.1 Methods

Current – voltage characteristics were measured on a Keithley 2400 Sourcemeter under simulated AM 1.5G sunlight at 100 mW cm^{-2} generated using an AAB ABET Technologies Sun 2000 solar simulator and calibrated using an NREL calibrated silicon reference cell with a KG5 filter to minimise spectral mismatch (the mismatch factor was calculated to be less than 1%). To avoid over-estimation of the active area resulting in an erroneous short circuit current density[12,13], the solar cells were masked with a metal aperture to define an active area of 0.09 cm^2 and measured in a light-tight sample holder to minimise any edge effects.

To measure the transient photocurrent and photovoltage decay, a white light bias was generated using an array of diodes (Lumiled Model LXHL-NWE8 whitestar). The perturbation source was generated from an array of red-light pulsed diodes (LXHLND98 redstar, 200 μs square pulse width, 100 ns rise and fall time), controlled by a fast solid-state switch. The photovoltage decay was measured on a 1 GHz Agilent oscilloscope across the high impedance (1 MΩ) port, while the photocurrent decay was measured through a low impedance port (50 Ω) to enable short circuit condition.

6.3.2 Results and discussion

Figure 6.6 shows the *J-V* characteristics of the highest efficiency porous and planar junction devices. The table compares the device parameters and standard

deviations extracted from the current density-voltage (*J-V*) characteristic curves of all 10 working devices. The devices with the porous structure exhibit an enhancement in short circuit current density under AM1.5G illumination. The porous structure produced an average power conversion efficiency of 5% and a 5.7% champion device was recorded. The champion device has a J_{sc} of 19 mA/cm^2, a V_{oc} of 0.51 V and a *FF* of 59%. An enhancement in fill factor is also observed in the porous device, indicating reduced recombination.

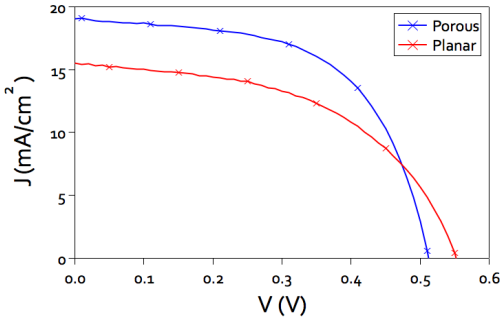

	Porous	Planar
PCE	5.0±0.4	3.2±0.7
J_{sc} (mA/cm^2)	16.7±1.5	12.4±1.9
V_{oc} (V)	0.51±0.00	0.53±0.03
FF (%)	58±3	47±5
R_s (Ω cm^2)	4.7±0.4	9.4±2.8

Figure 6.6: J - V characteristic curves of the best porous and planar junction devices. The table lists the averaged device parameters for comparison.

To understand the origin of the increased photocurrent in the porous TiO_2 structure, external quantum efficiency (EQE) at wavelengths between 400 and 1200 nm (Figure 6.7(a)) was measured. The device with a porous structure displays a higher EQE than the planar device across the whole range of wavelengths, particularly at short wavelengths. To elucidate the EQE enhancement, the optical properties of the devices were first examined.

Figure 6.7(b) shows the absorption spectra of the planar and porous films. The measurement is performed with and without an integrating sphere. Increased absorption by the porous film is only observed below 700 nm. From the SEM cross-section images it is clear that there is roughly the same thickness of PbS pristine layers in both porous and planar devices. The difference being that the porous structure allows this extra layer of fully depleted PbS in the device that enhances absorption of the visible light up to 700 nm, contributing to photocurrent generation. In a planar junction device, increasing the thickness will have charges are generated beyond the reach of the electric field leading to an increase in recombination. Furthermore, some enhancement of photocurrent can be attributed to increased absorption through light scattering within the porous structure. Yu *et al.*[14] suggest that a 300 nm pore size is most efficient in scattering light of visible wavelengths[15]. The porous TiO_2 film looks visually translucent as the pores behave as scattering centres, leading to a better light management within the device. This scattering could explain the particular enhancement of absorption at the shorter wavelengths. The enhancement in EQE cannot be fully explained by the optical effects alone, however, as the porous film does not show higher optical absorption above 700 nm. Meanwhile, a higher fill factor suggests repressed recombination in this device and therefore the electronic properties are now examined.

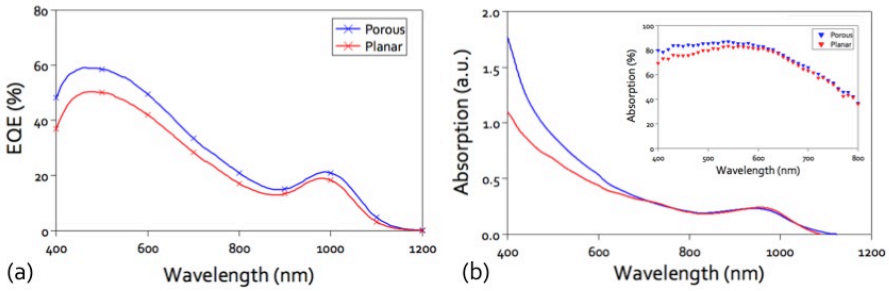

Figure 6.7: (a) External quantum efficiency of porous and planar devices from wavelength 400 - 1200 nm; (b) absorption spectra of planar and porous device films, inset showing the integrated sphere-corrected absorption spectra.

Using semiconductor process simulation, Kramer *et al.*[4] and Fan *et al.*[5] have shown an interpenetrated p-n junction device to be more efficient in charge extraction by suppressing Shockley-Read-Hall recombination. A significant increase in interface area means more carriers are generated in the vicinity of the junction interface, where the electric field strength is higher than the region further away from the junction. To measure whether the porous device can reduce trap-assisted recombination, small perturbation transient photocurrent and photovoltage decay measurements were performed on our devices[16–18]. These measurements allow us to monitor the fate of the exited carriers and to study the recombination and transport properties of the PbS/TiO_2 heterojunction[19]. The solar cells are illuminated under simulated sunlight at different illumination intensities and "flashed" by a red light pulse generated by LEDs. The resulting transient photocurrent and photovoltage decays are then measured. The mean

decay lifetime can be calculated by fitting the decay to an exponential function. The light pulse excites additional electrons will decay with a lifetime τ.

The transient photocurrent decay curves of both devices are shown in Figure 6.8(a), the inset shows a close-up of the initial decay region. Both devices have rapid initial decay for 10 μs as free electrons drift out of the PbS to TiO_2 to produce current[20] as well as rapid trapping of the electrons[21]. However, the porous device shows a long-lived tail, with continuous charge extraction up to 3 ms. The origin of this long-lived photocurrent tail has been associated with a slow de-trapping process[22]. This suggests that the BHJ has the ability to free charges from traps to produce higher photocurrent. This is probably assisted by the stronger electric field close to the interface of the BHJ such that trap-assisted recombination is reduced. To further verify that this slow decay dynamic is trap-meditated, the background intensity was varied as a means to change the charge occupation density of the trap states in the semiconductors. Figure 6.8(b) shows the transient photocurrent decay at different background light intensity. It is evident that a slower decay rate is observed with decreasing background intensity. At lower background intensity when more traps are unoccupied, there is a higher probability for electrons to be trapped in these states. The calculated decay lifetime of the planar device is 24 μs, while the porous structure is 280 μs, suggesting rapid trapping of charges in the planar device, which subsequently recombine. The extended lifetime in the case of porous structure suggests that the

trapped charges can be subsequently extracted. This is confirmed by transient photovoltage decay measurements, which are performed to directly measure the electron recombination lifetime under open-circuit conditions. Both planar and porous devices have the same recombination lifetime of around 20 μs when no charge extraction occurs.

The light intensity dependence of the normalised J_{sc} to J_{sc} at 1 sun intensity is shown in Figure 6.8(d). The data are fitted to the power law relationship $J_{sc} \propto I^{\alpha}$. The porous device produced a nearly linear relationship (α = 0.92) suggesting the device is operated with minimal recombination. High charge recombination in the planar junction device is indicated by a sub-linear relationship[16] with α = 0.78.

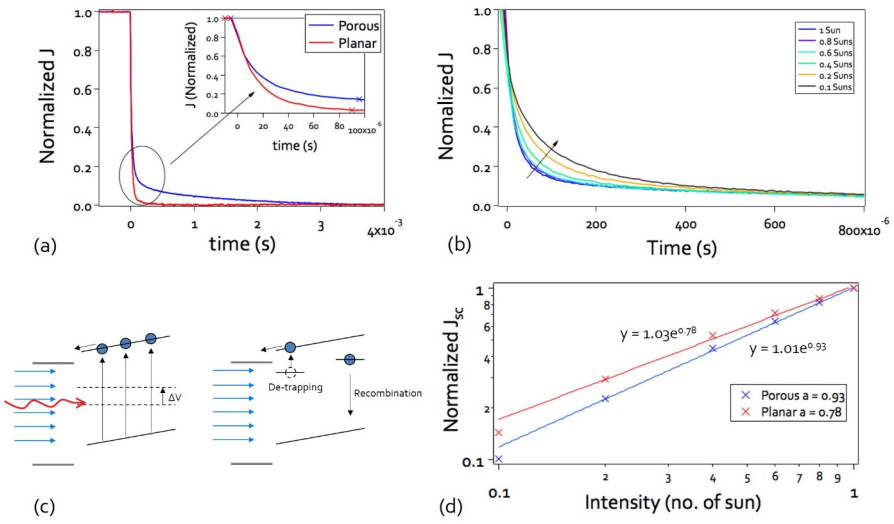

Figure 6.8: (a) Transient photocurrent decay curves of porous and planar junction devices; (b) transient photocurrent decay curves of a porous device at different background illumination intensity; (c) schematic illustrating the charge generation induced by the red-light pulse and the de-trapping and recombination process in the

depletion region. The de-trapping process is likely to occur closer to the interface where a stronger electric field is predicted to be present; (d) intensity-dependent measurement of normalized J_{sc}.

6.4 Conclusion

By careful design of the porous structure in conjunction with the electronic properties of the QD heterojunction, a significant improvement of the power conversion efficiency has been demonstrated in the porous bulk heterojunction. This is enhanced by a 30% increase in short circuit current and 10% increase in fill factor, leading to a 5.7% AM1.5 efficiency device. The porous device allows a thicker fully depleted PbS QDs layer to be incorporated in the device to absorb more photons while ensuring all photoexcited charges can still be extracted. Absorption has also been enhanced by the scattering effect of the pores. The BHJ structure also enhances the electronic properties by incorporating a large interface, showing a drastic increase in carrier lifetime resulting from de-trapping of charge carriers.

6.5 References

1. Pattantyus-Abraham, A. G.; Kramer, I. J.; Barkhouse, A. R.; Wang, X.; Konstantatos, G.; Debnath, R.; Levina, L.; Raabe, I.; Nazeeruddin, M. K.; Grätzel, M.; *et al.* Depleted-Heterojunction Colloidal Quantum Dot Solar Cells. *ACS Nano* **2010**, *4*, 3374–3380.

2. Barkhouse, D. A. R.; Debnath, R.; Kramer, I. J.; Zhitomirsky, D.; Pattantyus-Abraham, A. G.; Levina, L.; Etgar, L.; Grätzel, M.; Sargent, E. H. Depleted Bulk Heterojunction Colloidal Quantum Dot Photovoltaics. *Advanced Materials* **2011**, *23*, 3134–3138.

3. Etgar, L.; Moehl, T.; Gabriel, S.; Hickey, S. G.; Eychmüller, A.; Grätzel, M. Light Energy Conversion by Mesoscopic PbS Quantum dots/TiO_2 Heterojunction Heterojunction Solar Cells. *ACS Nano* **2012**, 3092–3099.

4. Kramer, I. J.; Zhitomirsky, D.; Bass, J. D.; Rice, P. M.; Topuria, T.; Krupp, L.; Thon, S. M.; Ip, A. H.; Debnath, R.; Kim, H.-C.; *et al.* Ordered Nanopillar Structured Electrodes for Depleted Bulk Heterojunction Colloidal Quantum Dot Solar Cells. *Advanced Materials* **2012**, *24*, 2315–2319.

5. Fan, Z.; Razavi, H.; Do, J.; Moriwaki, A.; Ergen, O.; Chueh, Y.-L.; Leu, P. W.; Ho, J. C.; Takahashi, T.; Reichertz, L. a; *et al.* Three-Dimensional Nanopillar-Array Photovoltaics on Low-Cost and Flexible Substrates. *Nature Materials* **2009**, *8*, 648–653.

6. Leschkies, K. S.; Jacobs, A. G.; Norris, D. J.; Aydil, E. S. Nanowire-Quantum-Dot Solar Cells and the Influence of Nanowire Length on the Charge Collection Efficiency. *Applied Physics Letters* **2009**, *95*, 193103.

7. Lan, X.; Bai, J.; Masala, S.; Thon, S. M.; Ren, Y.; Kramer, I. J.; Hoogland, S.; Simchi, A.; Koleilat, G. I.; Paz-Soldan, D.; *et al.* Self-Assembled, Nanowire Network Electrodes for Depleted Bulk Heterojunction Solar Cells. *Advanced Materials* **2013**, *25*, 1769–1773.

8. Gao, J.; Luther, J. M.; Semonin, O. E.; Ellingson, R. J.; Nozik, A. J.; Beard, M. C. Quantum Dot Size Dependent J-V Characteristics in Heterojunction ZnO/PbS Quantum Dot Solar Cells. *Nano letters* **2011**, *11*, 1002–8.

9. Willis, S. M.; Cheng, C.; Assender, H. E.; Watt, A. A. R. The Transitional Heterojunction Behavior of PbS/ZnO Colloidal Quantum Dot Solar Cells. *Nano Letters* **2012**, *12*, 1522–1526.

10. Lee, E.; Pyun, S. Analysis of Nonlinear Mott-Schottky Plots Obtained from Anodically Passivating Amorphous and Polycrystalline TiO2 Films. *Journal of Applied Electrochemistry* **1992**, *22*, 156–160.

11. Sellers, M. C. K.; Seebauer, E. G. Measurement Method for Carrier Concentration in TiO_2 via the Mott–Schottky Approach. *Thin Solid Films* **2011**, *519*, 2103–2110.

12. Snaith, H. J. How Should You Measure Your Excitonic Solar Cells? *Energy & Environmental Science* **2012**, *5*, 6513–6520.

13. Snaith, H. J. The Perils of Solar Cell Efficiency Measurements. *Nature Photonics* **2012**, *6*, 337–340.

14. Yu, I. G.; Kim, Y. J.; Kim, H. J.; Lee, C.; Lee, W. I. Size-Dependent Light-Scattering Effects of Nanoporous TiO2 Spheres in Dye-Sensitized Solar Cells. *Journal of Materials Chemistry* **2011**, *21*, 532–538.

15. Ferber, J.; Luther, J. Computer Simulations of Light Scattering and Absorption in Dye-Sensitized Solar Cells. *Solar Energy Materials and Solar Cells* **1998**, *54*, 265–275.

16. Zhao, N.; Osedach, T. P.; Chang, L.-Y.; Geyer, S. M.; Wanger, D.; Binda, M. T.; Arango, A. C.; Bawendi, M. G.; Bulovic, V. Colloidal PbS Quantum Dot Solar Cells with High Fill Factor. *ACS Nano* **2010**, *4*, 3743–3752.

17. Snaith, H. J.; Moule, A. J.; Klein, C.; Meerholz, K.; Friend, R. H.; Grätzel, M. Efficiency Enhancements in Solid-State Hybrid Solar Cells via Reduced Charge Recombination and Increased Light Capture. *Nano Letters* **2007**, *7*, 3372–3376.

18. O'Regan, B. C.; Lenzmann, F. Charge Transport and Recombination in a Nanoscale Interpenetrating Network of n-Type and p-Type Semiconductors: Transient Photocurrent and Photovoltage Studies of TiO2/Dye/CuSCN Photovoltaic Cells. *Journal of Physical Chemistry B* **2004**, *108*, 4342–4350.

19. Docampo, P.; Guldin, S.; Stefik, M.; Tiwana, P.; Orilall, M. C.; Hüttner, S.; Sai, H.; Wiesner, U.; Steiner, U.; Snaith, H. J. Control of Solid-State Dye-Sensitized Solar Cell Performance by Block-Copolymer-Directed TiO2 Synthesis. *Advanced Functional Materials* **2010**, *20*, 1787–1796.

20. Lee, M. M.; Teuscher, J.; Miyasaka, T.; Murakami, T. N.; Snaith, H. J. Efficient Hybrid Solar Cells Based on Meso-Superstructured Organometal Halide Perovskites. *Science* **2012**, *338*, 643–647.

21. Li, Z.; McNeill, C. R. Transient Photocurrent Measurements of PCDTBT:PC70BM and PCPDTBT:PC70BM Solar Cells: Evidence for Charge Trapping in Efficient Polymer/fullerene Blends. *Journal of Applied Physics* **2011**, *109*, 074513.

22. McNeill, C. R.; Hwang, I.; Greenham, N. C. Photocurrent Transients in All-Polymer Solar Cells: Trapping and Detrapping Effects. *Journal of Applied Physics* **2009**, *106*, 024507.

Chapter 7 - Conclusions and further work

7.1 Conclusions of the thesis findings

The study in this thesis shows the great potential for using solution-processed PbS quantum dots for next generation low-cost photovoltaics. The past three years' research has improved the power conversion efficiency of the PbS QD solar cells from 1.8% of the Schottky junction device, to 3% of the PbS/ZnO heterojunction device and to 5.7% of the structured bulk heterojunction TiO_2/PbS device. This enhancement in efficiency was achieved by 1) optimisation of processing condition and parameters: this includes both synthesis and post-synthesis procedure as well as assembly of QD thin film using spin coating and solid-state ligand exchange; 2) optimisation of device architecture: from Schottky junction to heterojunction to bulk heterojunction. The scientific findings of the thesis can be summarised as follows:

1) Light absorption of the QD devices can be improved by increasing the absorber layer thickness. However, the optimum thickness is limited by the width of the depletion region, beyond which charge extraction is poor. Creating a QD bulk heterojunction is an effective approach to overcome the charge extraction length by incorporating a large interface in the device. This allows a thicker device to be made while maintaining good charge collection ability.

2) Designing a QD bulk heterojunction should be rationalised by understanding the charge separation mechanism of QD heterojunction, which has been an area of discussion. The study shows that PbS/ZnO heterojunction shows both excitonic and depleted p-n junction mechanism depending on the doping density of ZnO.

3) It is shown that efficient charge separation in QDs should be driven by an electric field. Charge extraction via an excitonic route in the bulk heterojunction PbS/ZnO made from the nanocrystal blend suffers from strong interfacial recombination, resulting in low efficiency. Creating a porous TiO_2 template to allow the phase separation between the donor and acceptor to match with the depletion width can ensure the charge separation is electric field-driven even within thick devices, and hence provides a route to higher photocurrents.

7.2 Further work

1) Deeper understanding of the QD operating mechanism.

A number of literature[1,2] suggests that a p-n junction behaviour displays in a quantum confined system is because the excitons have relative low binding energy and can dissociate into free electrons and holes between highly coupled PbS QDs. This question still remains debatable and varies for different types of QD materials. Further experimental and theoretical study should be carried out to investigate this hypothesis and draw a generalised picture. This will help

researchers in materials selection and device architectural design for both QD photovoltaics and light-emitting diodes.

2) Improving the materials' electronic properties.

Improving the charge carrier mobility and lifetime of semiconductor QDs as well as their robustness to oxygen and moisture can be achieved by engineering the surface properties of the materials. Modifying the QD surface using novel organic or inorganic ligands can improve the surface passivation of QDs as well as the charge transport in solid film. Bulk doping by using substitutional atoms can also result in more intrinsic alteration to the QD properties.

3) Increasing light absorption.

The thesis reports studies of metal oxide semiconductors (ZnO and TiO_2) as an electron acceptor. n-type semiconductors with visible wavelength band gap can be used to complement the absorption of PbS QDs. This includes n-type QDs such as CdS, ZnS, SnS_2, Bi_2S_3 and etc., and some organic materials such as C_{60} and C_{70}. These n-type absorbers can also be made into QD bulk heterojunction devices to further improve absorption and extraction. Furthermore, QD tandem devices will be the key to finally overcome the Schockley-Queisser limit.

7.3 References

1. Choi, J. J.; Luria, J.; Hyun, B.-R.; Bartnik, A. C.; Sun, L.; Lim, Y.-F.; Marohn, J. A.; Wise, F. W.; Hanrath, T. Photogenerated Exciton Dissociation in

Highly Coupled Lead Salt Nanocrystal Assemblies. *Nano Letters* **2010**, *10*, 1805–1811.

2. Cate, S. ten; Schins, J. M.; Siebbeles, L. D. A. Origin of Low Sensitizing Efficiency of Quantum Dots in Organic Solar Cells. *ACS Nano* **2012**, *6*, 8983–8988.